Determining the dominant degradation mechanisms in Nitrocellulose [CORRECTIONS]

Amy J. Lai

A thesis submitted in partial fulfilment

of the requirements for the degree of

Doctor of Philosophy

of

University College London.

Department of Chemistry

University College London

December 18, 2019

Abbreviations

%N	percentage nitrogen by mass
2-NDPA	2-Nitrodiphenylamine
AIMD	*ab initio* molecular dynamics
AO	atomic orbital
a.u.	atomic units
B3LYP	Becke, 3-parameter, Lee-Yang-Parr hybrid functional
BCP	bonding critical point
BSSE	basis set superposition error
CH_3/CH_3	NC repeat unit with two $-OCH_3$ capping groups
CH_3/OH	NC repeat unit with $-OCH_3$ capping group on ring 1 and $-OH$ group on ring 2
OH/CH_3	NC repeat unit with $-OH$ capping group on ring 1 and $-OCH_3$ group on ring 2
CCP	cage critical point
CP	critical point
DFT	density functional theory
DFT-D	density functional theory with dispersion correction
DSC	differential scanning calorimetry
DOS	degree of substitution

DPA	diphenylamine
EN	ethyl nitrate
ESP	electrostatic potential
FF	force field
G09	Gaussian 09 revision E.01
GGA	generalised gradient approximation
GM	genetically modified
GTO	Gaussian type orbitals
GView	Gauss View 5.0.8
HF	Hartree-Fock
HMF	hydroxymethylfurfural
HOMO	highest occupied molecular orbital
IR	infra-red spectroscopy
KS-DFT	Kohn-Sham DFT
LDA	local density approximation
MD	molecular dynamics
MEP	minimum energy path
MM	molecular mechanics
MMFF94	Merck molecular force field 94
MO	molecular orbitals
MP2	Møller–Plesset perturbation theory with second order correction
MW	molecular weight
NBO	natural bond orbital

NC   nitrocellulose

NCP   nuclear critical point

NG   nitroglycerine

NMR   nuclear magnetic resonance spectroscopy

PCM   polarisable continuum model

PES   potential energy surface

PETN   pentaerythritol tetranitrate

PETRIN   pentaerythritol trinitrate

QM   quantum mechanics

QTAIM   quantum theory of atoms in molecules

RCP   ring critical point

RESP   restrained electrostatic potential atomic partial charges

RHF   restricted HF

RMS   root mean square

ROHF   restricted-open HF

UHF   unrestricted HF

SB59   1,4-bis(ethylamino)-9,10-anthraquinone dye

SCF   self-consistent field

SCRF   self-consistent reaction field

SEM   scanning electron microscopy

SMD   solvation model based on density

S_N2   bi-molecular nucleophilic substitution reaction

STO   Slater type orbitals

TG   thermogravitmetric analysis

TS   transition state

UFF   universal force field

UV   ultraviolet

UV-vis   ultraviolet–visible spectroscopy

vdW   van der Waals

ωB97X-D ωB97X-D long-range corrected hybrid functional

ZPE   zero-point energy

Chapter 1

Theory and Implementation

1.1 Electronic structure methods

Electronic structure methods apply the principles of quantum mechanics to the evaluation of electron position and movement, thereby allowing chemists to derive the properties and interactions of molecules. Despite the long history of research and use of nitrocellulose (NC) in industry, experimental analysis has failed to distinguish the fine mechanistic details of its decomposition. This is partly owed to the variation arising from biodiverse NC source materials, combined with the complexity due to the interplay of many different and simultaneous degradation interactions. Electronic structure methods provide a means to untangle the individual facets of decomposition.

At the most fundamental level, the wave function (Ψ) holds the description of a quantum system. In a non-relativistic system, the probability of a particle possessing a given momentum, or residing in a particular location, is given by the probability density. This can be obtained by multiplication of Ψ with its complex conjugate, $|\Psi^2|$. Integration of $|\Psi^2|$ over a region of space returns the probability that a system will be found within, called the Born interpretation. Values of Ψ are chosen to be orthonormal; integrating $|\Psi^2|$ over all space gives the probability of 1:

$$\langle \Psi_i | \Psi_j \rangle = \delta_{ij} \tag{1.1}$$

where all states are represented by i and j, and:

$$\delta_{ij} = 0 \text{ for } i \neq j$$

$$\delta_{ij} = 1 \text{ for } i = j \text{ the integral is one.}$$

Operators acting on Ψ yield the observable properties of the system. The operator returning the energy of the system is called the the Hamiltonian operator (**H**). Erwin Schrödinger

proposed his equation in 1926, describing a quantum system using its wave function [1]. Schrödinger's time-independent equation is:

$$\mathbf{H}\Psi = E\Psi \tag{1.2}$$

and the energy of the system is given by the expectation value of the Hamiltonian operator:

$$E = \langle \Psi | \mathbf{H} | \Psi \rangle \tag{1.3}$$

where the Hamiltonian operator $\mathbf{H}$ is an eigenvalue of the wave function Ψ, and E is a scalar denoting the energy of the system. A given system may have many acceptable values for Ψ, each with an associated value for E.

The general form of the Hamiltonian is given by:

$$\mathbf{H} = -\sum \frac{\hbar^2}{2m_e}\nabla_i^2 - \sum \frac{\hbar^2}{2m_k}\nabla_k^2 - \sum_i \sum_k \frac{e^2 Z_k}{r_{ik}} + \sum_{i<j} \frac{e^2}{r_{ij}} + \sum_{k<l} \frac{e^2 Z_k Z_l}{r_{kl}} \tag{1.4}$$

where all electrons are represented by i and j, and all nuclei by k and l [2]. $\hbar$ is the reduced Planck's constant ($\hbar = \frac{h}{2\pi} = 1.055 \times 10^{-34}$ Js), m_e is the mass of an electron, m_k is the mass of the nucleus k, e is the charge of an electron, Z_k is the atomic number of k and r_{ik} is the distance between particles i and k. When using atomic units (a.u.), the value of e, m_e and $\hbar$ are reduced to 1. ∇^2 refers to the Laplacian operator, which describes the divergence of the gradient of a field. In Cartesian space, this is defined as the sum of the second derivatives of the gradient with respect to each of the three dimensions (x,y,z):

$$\nabla_i^2 = \frac{\partial^2}{\partial x_i^2} + \frac{\partial^2}{\partial y_i^2} + \frac{\partial^2}{\partial z_i^2} \tag{1.5}$$

The first and second terms of equation (1.4) correspond to the kinetic energy of the electrons and the nuclei, respectively. Electron-nuclear attraction is described by the third term; the fourth term describes inter-electronic repulsion and the final term the inter-nuclear repulsion. The final three potential energy terms are identical to their expression in classical mechanics. The kinetic energy terms can be expressed as the eigenvalues of the kinetic energy operator ($\mathbf{T}$):

$$\mathbf{T} = -\frac{\hbar^2}{2m}\nabla^2 \tag{1.6}$$

The total, non-relativistic Hamiltonian can therefore be written in terms of the kinetic energy and potential energy operators:

$$\mathbf{H} = \mathbf{T}_e + \mathbf{T}_N + \mathbf{V}_{e-N} + \mathbf{V}_{e-e} + \mathbf{V}_{N-N} \qquad (1.7)$$

where the terms are as they were in equation 1.4. $\mathbf{T}_e$ corresponds to the kinetic energy of the electrons, $\mathbf{T}_N$ the kinetic energy of the nuclei, $\mathbf{V}_{e-N}$ the coulombic interaction between electron and nuclei, $\mathbf{V}_{e-e}$ the electron-electron repulsion and $\mathbf{V}_{N-N}$ the nuclear-nuclear interaction.

1.1.1 Born-Oppenheimer approximation

In a real system, the motion of elections and nuclei are coupled. Electron density flows dynamically in response to the change in nuclear position and repulsion from other electrons. The correlated motion of particles is described by the pairwise attractive and repulsive terms of the Schrödinger equation. However, this interdependency makes defining a wave function difficult. Relative to electronic motion, nuclei move far more slowly, owing to their much greater mass (the mass of a proton is around 1836 times larger than that of the electron). Nuclear positions therefore appear essentially stationary when compared to that of the electrons. Exploiting this property, the Born-Oppenheimer approximation fixes the nuclear positions. In this way, the motion of electrons and nuclei can be decoupled, and the electronic properties of the system may be calculated for the given nuclear coordinates. Dependency on the nuclear kinetic energy term ($\mathbf{T}_N$) is removed, as the nuclei are frozen. The nuclear-nuclear repulsive term ($\mathbf{V}_{N-N}$) becomes a constant for the specified geometry. Equation 1.4 is reduced to its electronic components and nuclear constants which in atomic units can be written as:

$$\mathbf{H} = \mathbf{T}_e + \mathbf{V}_{e-N} + \mathbf{V}_{e-e} + \mathbf{V}_{N-N} \qquad (1.8)$$

and the electronic terms can be collected into one term, to simplify notation:

$$\mathbf{H} = \mathbf{H}_{el} + \mathbf{V}_{N-N} \qquad (1.9)$$

The Schrödinger's equation can now be written in terms of only the electronic coordinates:

$$(\mathbf{H}_{el} + \mathbf{V}_{N-N})\Psi_{el}(\mathbf{q}_i; \mathbf{q}_k) = E_{el}(\mathbf{q}_i; \mathbf{q}_k) \qquad (1.10)$$

where the electronic coordinates are given by $\mathbf{q}_i$, the stationary nuclear positions by $\mathbf{q}_k$ and E_{el} is the electronic energy of the system. The values of $\mathbf{q}_i$ are independent variables, whereas the values of $\mathbf{q}_k$ are parameters.

Given the example of a diatomic molecule, a potential energy curve can be obtained by calculating the value of E_{el} at different inter-nuclear distances. A series of these calculations generates a potential energy profile, allowing identification of an equilibrium bond length at the minimum of the curve. Calculation of E_{el} for all possible nuclear coordinates in a system of three or more atoms facilitates the construction of a hypersurface on which the potential energy is defined by the nuclear geometry, called a potential energy surface (PES). Exploration of the PES allows for discovery of global and local minimum energy structures, intermediate products and transition states on a reaction coordinate, through scrutiny of the energy at a particular set of nuclear coordinates.

Molecular structure theories adopt the Born-Oppenheimer approximation for its effective simplification of the coupled nuclear-electronic motion problem, in addition to its accuracy; this assumption works well for ground state molecules and only introduces very small errors. The model breaks down in the situation where there are multiple PES close in energy to one another, or even intersecting. In these cases the coupled equations must be considered. However for the work within this study, the Born-Oppenheimer approximation is successfully applied for all calculations involving electronic structure determination.

1.1.2   Slater determinants

In a system of multiple electrons, each electron is indistinguishable. If the positions of two electrons are swapped, the distribution of electron density in the system remains the same. The Pauli exclusion principle states that no two identical fermions, such as electrons, may simultaneously occupy the same quantum state within the same system. When considering an atom with two or more electrons, this means that none may have the same set of quantum numbers. As a result, for two equivalent electrons, the wave function of the system is antisymmetric with respect to the exchange of their coordinates:

$$\Psi(1,2,...N) = -\Psi(1,2,..N) \tag{1.11}$$

This requirement is fulfilled by expressing the wave function as a Slater determinant, which changes sign with permutation of the coordinates of two electrons. In the case of a

multi-electronic system, the generalised Slater determinant for N total electrons is as follows:

$$\psi_{SD} = \frac{1}{\sqrt{N!}} \begin{vmatrix} \chi_1(1) & \chi_2(1) & \cdots & \chi_N(1) \\ \chi_1(2) & \chi_2(2) & \cdots & \chi_N(2) \\ \vdots & \vdots & \ddots & \vdots \\ \chi_1(N) & \chi_2(N) & \cdots & \chi_N(N) \end{vmatrix} \tag{1.12}$$

where χ_N represents single electron wave functions, or spin-orbitals [3]. In the context of a molecule, the single electron wave functions are molecular orbitals. Rows are labelled by the coordinates of each electron: (1), (2) $\cdots$ (N), whereas each column uses a different orbital function: χ_1, $\chi_2 \cdots$, χ_N. If the labels of (1) and (2) are exchanged, the rows of the determinant are exchanged; a general property of determinants is that the interchange of two rows leads to a change of sign. The expanded form of the determinant (ψ_{SD}) will have the opposite sign when a pair of electronic coordinates are switched, by switching rows within the determinant, thereby fulfilling the antisymmetry requirement. In the dis-allowed case of two equivalent electrons occupying the same spin-orbital, two columns would be identical [4]. The evaluation of the determinant would then be zero, indicating that the probability of two electrons with identical spin occupying the same orbital was zero.

1.1.3 Variational principle

In order to obtain the ground state energy of a system, the wave function giving the lowest energy must be found. This corresponds to the electronic configuration with lowest value of E_{el}. Difficulty then arises, as ground state energy cannot be computed exactly. The variational theorem states that the calculated energy of any guess wave function can only be greater than or equal to the real ground-state energy (E_0) of the system. This provides a criterion for selection of the best guess wave function, as the energy is always bounded from below, where:

$$E = \langle \Psi | \mathbf{H} | \Psi \rangle \geq E_0 \tag{1.13}$$

for a normalised wave function. Thus, when choosing between different trial wave functions, the solution with the lowest energy is the one closest to the exact value.

1.1.4 Hartree-Fock self-consistent field method

In practice, equation 1.10 can only be solved *exactly* in very few circumstances; no exact solutions can be found for problems involving three or more interacting particles, such as in

the case of a helium atom possessing two electrons and a nucleus. For systems of complexity greater than one electron, further approximations must be made.

The Hartree-Fock (HF) approximation was the first practically applicable method for calculation of the ground-state energy of atoms with fixed nuclear positions. The self-consistent field (SCF) method was proposed by Hartree in 1928 [5, 6]. N electrons are treated as individual particles occupying single-electron spin orbitals and move independently of the dynamics of any other fermions in the system. The effective interaction of one electron with all other fermions is averaged and applied as a static external field, in the form of a spherical potential around the electron (called the mean-field approximation). In this way, the N-body problem is reduced to a 1-body problem. The approximation neglects exchange in the electron-electron interaction; the calculated Hartree wavefunction alone does not include any contribution from electron correlation, and incorrectly implies that the electrons are distinguishable. Fock developed this idea by introducing Slater determinant wave functions [7]. The effects of exchange on the coulombic repulsion were incorporated, achieved by taking the trial wave function as a single Slater determinant.

For an electron in orbital χ_i in the field of nuclei M and other electrons χ_j, the Hamiltonian operator is comprised of three terms, corresponding to the three contributions to the energy. The core Hamiltonian operator, $\mathbf{H}^{core}$ comprises of the kinetic energy of each electron, and the electron-nuclear interaction:

$$\mathbf{H}^{core}(1) = -\frac{1}{2}\nabla_1^2 - \sum_{A=1}^{M}\frac{Z_A}{r_{1A}} \tag{1.14}$$

where Z_A is the nuclear charge and r_{1A} is the separation of electron (1) with nucleus A. In a mono-electronic system, this would be the only operator present.

The coulomb operator, $\mathbf{J}_j$ corresponds to the averaged interaction potential between each pair of electrons in the same orbital, and with other electrons in other orbitals χ_j:

$$\mathbf{J}_j(1) = \int d\tau_2 \chi_j(2)\frac{1}{r_{12}}\chi_j(2) \tag{1.15}$$

where $d\tau_i$ indicates the integration is over the spatial and spin coordinates of electron i, and r_{12} is the distance between the two electrons.

The exchange operator $\mathbf{K}_j$, is only non-zero for electrons with the same spin, arising

due to the antisymmetry of the wavefunction:

$$\mathbf{K}_j(1)\chi_i(1) = \left[\int d\tau_2 \chi_j(2)\frac{1}{r_{12}}\chi_j(2)\right]\chi_j(1) \tag{1.16}$$

defined in terms of its effect when acting on χ_i. The Hamiltonian operator written in terms of its core, coulomb and exchange contributions is as follows:

$$\left[\mathbf{H}^{core}(1) + \sum_{j=1}^{N}\{\mathbf{J}_j(1) - \mathbf{K}_j(1)\}\right]\chi_i(1) = \sum_{j=1}^{N}\varepsilon_{ij}\chi_j(1) \tag{1.17}$$

and can be simplified to:

$$\mathbf{F}_i\chi_i = \sum_j \varepsilon_{ij}\chi_j \tag{1.18}$$

where $\mathbf{F}_i$ is the Fock operator, and ε_{ij} is the energy of orbital χ_j. The operator is a one electron Hamiltonian for an electron in a multi-electron system. For "closed shell" problems where there are no unpaired electrons, the operator has the form:

$$\mathbf{F}_i(1) = \mathbf{H}^{core}(1) + \sum_{j=1}^{N/2}\{2\mathbf{J}_j(1) - \mathbf{K}_j(1)\} \tag{1.19}$$

$\mathbf{H}^{core}$ consisting of the kinetic energy terms can be solved exactly, the electron-electron repulsion $\mathbf{J}_j$ must apply the mean-field approximation but the exchange component $\mathbf{K}_j$ is solved iteratively. Starting with an initial guess wave functions for the occupied orbitals χ_i, solution of the one-electron HF eigenvalue equations generates a new set of orbitals. Applying the variational principle, the spin orbitals are varied to minimise the energy. This process propagates using the newly generated orbitals for the next optimisation, until the difference between the final solution and its previous iteration falls within an acceptable threshold and is "self-consistent".

1.1.5 Open shell systems

The forced pairing of electrons of opposing spin into a shared orbital is referred to as the *restricted* scheme (figure 1.1). For closed shell systems, this treatment is appropriate. For species with unpaired electron spin such as in transition metal complexes or radicals, an alternative model allowing singly occupied orbitals must be adopted. The *restricted-open* scheme maintains electron pairing within orbitals except in the case of the highest occupied molecular orbital (HOMO), which is singly occupied. An alternative model is the

unrestricted scheme, where all electrons are unpaired and reside in their own orbitals. A caveat of the unrestricted model is its susceptibility to spin contamination, which has consequences at large bond separations. This artificial mixing of spin states leads to a lowering of the obtained energies when compared to the restricted variants [8].
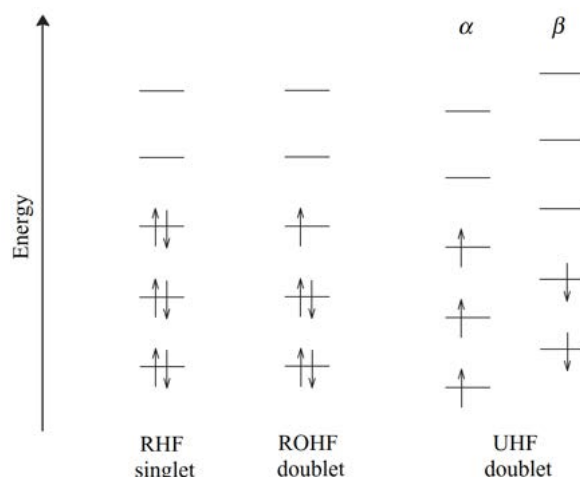

Figure 1.1: The electron ordering schemes corresponding to the restricted Hartree-Fock (HF), restricted-open HF (ROHF) and unrestricted HF (UHF) methods of calculation for closed and open shell systems [4].

1.1.6 Electron correlation

The energy difference between the real energy and the result obtained from HF is called the correlation energy, $E_{corr.}$.

$$E_{corr.} = E_{exact} - E_{HF} \qquad (1.20)$$

The $E_{corr.}$ term can be divided into two components. The static correlation component arises as a system cannot be fully described by a single set of molecular orbitals (MO)s, and the dynamic correlation contribution derives from the neglect of instantaneous electron repulsion interactions. The latter includes the description of instantaneous dipolar interactions, leading to van der Waals forces, which are lost when the electron repulsion terms are averaged. Post-HF methods such as perturbation theory and coupled-cluster techniques aim to account for the difference by inclusion of the contribution from correlation as an additive term, or *via* multi-electron wave functions. However, these methods become prohibitively expensive with increasing numbers of electrons, such that the system size is limited to small molecules for calculations of high accuracy. The high computational demand associated with handling a many-electron wave function is circumvented in density functional theory (DFT), by expression of the total energy in terms of electron density.

1.2 Density functional theory

There are two approaches for solving the Schrödinger equation for a polyatomic system with many electrons. *Ab initio* methods generate solutions from "first principles", without information gained from experimental results. By contrast, *semi-empirical* methods deal with parameters fitted to experimental quantities, such as enthalpies of formation or dipole moments. DFT derives from the Thomas-Femi-Dirac model, whereby electron correlation is modelled via functionals of the electron density, $\rho(r)$. Currently, it forms the most widely used approach for quantum mechanics (QM) problems. When compared to HF and post-HF methods, DFT provides increased computational efficiency. Modern hybrid functionals are able to produce results on the order of MP2 accuracy, utilising only the resource of a HF calculation. The NC monomers, dimer and trimer models examined in this study consist of between 30 - 75 atoms; DFT provided the best pay-off between accuracy and efficiency for application on a system of this size.

1.2.1 Hohenberg-Kohn formalism

Modern DFT is based on two fundamental theorems proposed by Hohenberg and Kohn in 1964 [9]. The first theorem states that for the ground state of system, there exists a unique energy and non-degenerate electron density. The density can therefore be used to determine the Hamiltonian of a system, thereby also describing its ground state energy $E[\rho(r)]$, wave function and other properties of the system. The energy is a functional of the density:

$$E[\rho(r)] = \int \rho(r)V(r)\,d(r) + F[\rho(r)] \tag{1.21}$$

where $V(r)$ is the external potential, with the first term of the equation arising from the interaction of electrons with $V(r)$ (usually a coulombic attraction between electrons and nuclei). $F[\rho(r)]$ is a universal functional of the density, representing the total kinetic energy and electron-electron repulsion. It is not possible to explicitly express $F[\rho(r)]$ in terms of $\rho(r)$, so its exact form is not known.

The second theorem states that the ground state energy can be obtained *via* minimisation of $E[\rho(r)]$. Since equation 1.21 gives the exact energy of the original Hamiltonian, by applying the variational principle, the lowest possible value of $E[\rho(r)]$ gives the real solution for the ground state energy, and therefore $\rho(r)$. It is not possible to verify that the found $\rho(r)$ giving the lowest value of $E[\rho(r)]$ corresponds to a wave function obeying the Pauli

exclusion principle requirement for antisymmetry. This problem and the unknown identity of $F[\rho(r)]$ were addressed by the Kohn-Sham equations.

1.2.2   Kohn-Sham DFT

The Kohn-Sham scheme establishes a system with N non-interacting electrons, in a similar manner to HF [10]. The wave function is described by a single Slater determinant of one-electron orbitals, and the electron density is set to be identical to that of the exact ground state wave function. Using this approximation, the energy of the system can again be divided up into its component contributions:

$$E[\rho] = E_{KE}[\rho(r)] + E_H[\rho(r)] + E_V[\rho(r)] + E_{XC}[\rho(r)] \tag{1.22}$$

where E_{KE} is the kinetic energy of the non-interacting electrons, E_H the Hartree electrostatic energy corresponding to the electron-electron repulsion between electrons, E_V the interaction between the electrons and the external potential due to the nuclei, and E_{XC} the exchange-correlation energy, encapsulating non-classical exchange and correlation contributions not accounted for by the other terms. Referring back to the Born interpretation (equation 1.1), the density can be obtained from the sum of the square moduli of the wave function:

$$\rho(r) = \sum_{i=1}^{N} |\psi_i(r)|^2 = |\Psi|^2 \tag{1.23}$$

Aside from the kinetic energy term in equation 1.22, the remaining terms can be summarised into an effective potential v_{eff}:

$$v_{eff} = v_H(r) + v_V(r) + v_{XC}(r) \tag{1.24}$$

where $v_H(r)$ is the electron repulsion potential and $v_V(r)$ the electron-ion potential. The exchange-correlation potential $v_{XC}(r)$ is the functional derivative of E_{XC}. If E_{XC} is known then $v_{XC}(r)$ can be computed from the following equation:

$$v_{XC}(r) = \frac{\delta E_{XC}}{\delta \rho} \tag{1.25}$$

The kinetic energy term in equation 1.22 can be expressed in terms of the one-electron

wave function:

$$E_{KE}[\rho(r)] = -\frac{1}{2}\nabla^2 \sum_{i=1}^{N} \langle \psi_i | \nabla^2 | \psi_i \rangle \tag{1.26}$$

Combining equations 1.24 and 1.26, a new Hamiltonian can be written, only considering the non-interacting system:

$$\mathbf{H} = -\frac{\nabla^2}{2} + v_{eff} \tag{1.27}$$

Using the Kohn-Sham formulation of the Schrödinger equation, the one-electron orbitals $\psi_i(r)$ have the form:

$$\left(-\frac{\nabla^2}{2} + v_{eff}(r)\right)\psi_i(r) = \varepsilon_i \psi_i(r) \tag{1.28}$$

where $v_{eff}(r)$ is the effective potential, $\psi_i(r)$ the Kohn-Sham orbitals and ε_i the Kohn-Sham orbital energies.

The Kohn-Sham equations are solved self-consistently. Evaluation of equation 1.22 gives the total electronic energy. A guess density is supplied for the initial evaluation of equation 1.28, to generate a set of orbitals. This in turn informs the next iteration with an improved density value, until convergence is reached.

1.2.2.1 Exchange-correlation functionals

Local density approximation

In practice, the exact solution for E_{XC} in equation 1.24 is not known, so an approximation is used. The simplest method is the local density approximation (LDA), based upon a uniform electron gas. ε_{XC} is calculated per electron as function of the density, and integration over all space gives the E_{XC} for the whole system:

$$E_{XC}^{LDA}[\rho(r)] = \int \rho(r)\varepsilon_{XC}[\rho(r)]\,dr \tag{1.29}$$

This method has demonstrated good results for structural properties such as bond lengths and lattice constants, often improving on HF results. The model falls down when considering systems with many molecules, overestimating binding energies and atomisation energies, and performing worse than HF for open shell atoms.

Generalised gradient approximation

To account for inhomogenous electron density present in real systems, the local gradient of the density $\nabla\rho(r)$ can be taken into account at each coordinate, on top of the existing dependency on the density $\rho(r)$. This gradient corrected approach is called the generalised

gradient approximation (GGA):

$$E_{XC}^{GGA}[\rho(r)] = \int \rho(r)\nabla[\rho(r)]\,dr \qquad (1.30)$$

The results obtained using GGA greatly improves upon LDA, such as in the calculation of bond dissociation energies. The GGA is split into its exchange and correlation contributions, which can be solved individually:

$$E_{XC}^{GGA} = E_X^{GGA} + E_C^{GGA} \qquad (1.31)$$

The function of $\nabla\rho(r)$ is not uniquely defined and no true form is known; further developments saw the proposal of numerous gradient correction schemes, often fitting to experimental parameters. Functionals that have been well established in literature include:

- B88: the exchange functional developed by Becke, and contains an empirical parameter β=0.0042 fitted to give the best agreement with the HF energies of the noble gases [11].

- LYP: a widely used GGA correlation functional, developed by Lee, Yang and Parr, with empirical fitting to the helium atom. Combination with the B88 exchange functional gives the BLYP method [12].

- PBE: the exchange-correlation functional developed by Perdew, Burke and Ernzerhof derived purely from *ab initio* calculations [13]. The PBE family of functionals have parameterisations optimised for different materials and interfaces, such as small molecules, crystal structures and metal surface energies [14, 15, 16].

1.2.3 Hybrid functionals

In DFT, the influence of the exchange contribution to E_{XC} is significantly larger than that of correlation, which only adds minor corrections [17]. In hybrid DFT, a portion of exact exchange is introduced into the DFT exchange energy *via* linear combinations of HF and GGA exchange. This assists to counteract the self-interaction problem, a significant source of error in most approximate exchange-correlation functionals used for Kohn-Sham DFT (KS-DFT) calculations. This spurious interaction of an electron with itself does not appear in HF where the exchange is defined exactly, and a cancelling of the coulomb and exchange-correlation energies occurs [18]. The description of the exchange-correlation is imperfect in

DFT; the exchange and coulomb energy terms do not completely cancel out, and an energy contribution is experienced even in a one electron system. An observable manifestation of this in larger systems is the underestimation of reaction barriers [19].

Perhaps the most widely used functional of this category is Becke, 3-parameter, Lee-Yang-Parr hybrid functional (B3LYP) [20, 21]. It is employed in the current study to examine the degradation reactions of NC. The formalism is as follows:

$$E_{XC}^{B3LYP} = E_X^{LDA} + a_0(E_X^{HF} - E_X^{LDA}) + a_X(E_X^{B88} - E_X^{LDA}) + E_c^{LDA} - a_C(E_C^{LYP} - E_C^{LDA}) \quad (1.32)$$

a_0, ca_X and a_C are parameters fitted to experimental atomisation energies, ionisation potentials, proton affinities and atomic energies. The semi-empirical coefficients have values of 0.20, 0.72 and 0.81, respectively, indicating that the B3LYP hybrid functional contains 20% HF exchange, 72% B88 exchange and 81% electron correlation contribution from LYP. B3LYP is of particular interest in the study of NC as it has been applied in comparable computational investigations on glucose and its analogues, which forms the base structure of the NC monomer [22, 23].

There are documented cases where B3LYP performs extremely poorly, such as in the description of $\pi \rightarrow \sigma$ structural transformations [24], and medium-long range dispersion interactions [25]. In the first case, no similar transitions are expected for the reactions studied in this work. When considering the medium-range electron correlation reactions that may occur for the investigated species, the distance at which the intermolecular interactions take place and at which B3LYP performance suffers (1.5-3.5 Å), is of relevance. The calculations falling within this range will therefore be performed with both B3LYP and the ωB97X-D long-range corrected hybrid functional (ωB97X-D), in order to validate and compare results.

Grimme proposed an empirical DFT method with dispersion correction to include van der Waals interactions, described as density functional theory with dispersion correction (DFT-D) [26, 27]. The general form of the DFT-D scheme is used to calculate the total energy of the system, with the addition of an empirical atomic-pairwise dispersion correction:

$$E_{DFT-D} = E_{KS-DFT} + E_{disp} \quad (1.33)$$

The ωB97X-D dispersion corrected functional was presented by Chai *et. al*, based on the

ωB97X, which is used to calculate the KS-DFT energy, E_{KS-DFT} [28, 29]. The approach is founded on Becke's B97-D GGA functional [30, 27]. For the B97-D functional, expansion coefficients were added to the original B97 and optimised to reduce the density functional at small separations where lower electron correlation was expected. At medium-long ranges, the density functional description was dictated by the semi-empirical dispersion correction term. In the case of ωB97X-D, the unscaled dispersion correction is defined as follows:

$$E_{disp} = -\sum_{i=1}^{N-1}\sum_{j=i+1}^{N} \frac{C_6^{ij}}{R_{ij}^6} f_{damp}(R_{ij}) \tag{1.34}$$

where N is the number of atoms in the system, C_6^{ij} is the dispersion coefficient for atom pair ij, and R_{ij} is the interatomic distance. At short interatomic distances, dispersion is zero. The asymptotic, pairwise van der Waals (vdW) potentials are maintained by the damping function:

$$f_{damp}(R_{ij}) = \frac{1}{1 + a(R_{ij}/R_r)^{-12}} \tag{1.35}$$

The function decreases to 1 as R_{ij} increases, but also diminishes quickly at small values of R_{ij} to prevent the divergence observed for the undamped case (figure 1.2). R_r is the sum of the vdW radii of the atoms ij, whilst a determines the strength of the dispersion corrections. The ωB97X-D functional incorporates 100% long-range exchange, 22% short-
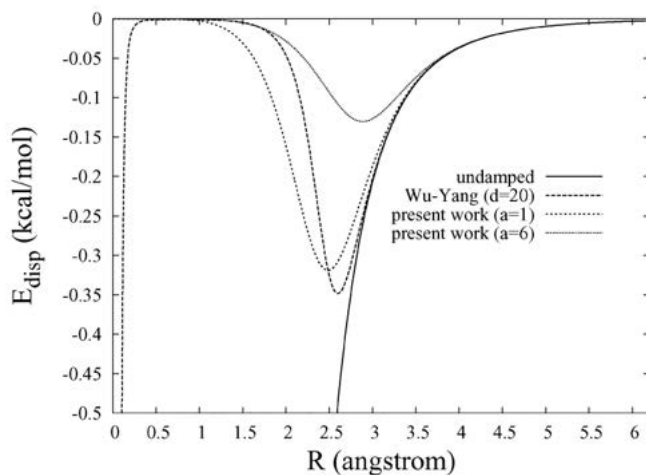
Figure 1.2: Dispersion energy of Ne_2 with and without the damping function (equation 1.35). The function of Wu and Yang ($f_{damp}^{WY}(R) = 1/(1+e^{-\frac{dR}{R_r-1}})$) is also compared [31]. Reproduced from the work of Chai *et. al* [28, 29] with permission from the PCCP Owner Societies.

range exchange, a modified B97 short-range exchange and B97 correlation, with empirical

dispersion corrections. When the constraint ω is reduced to 0, ωB97X-D is equivalent to the B97 functional with the addition of the dispersion correction. The performance of ωB97X-D will be compared to that of B3LYP in this work with particular attention paid to the reaction energies.

1.2.4 Basis set approximation

A basis set is the collection of mathematical basis functions, used in linear combination, to construct the molecular orbitals (MO). An individual MO can be defined as:

$$\psi_i = \sum_{\mu=1}^{N} c_{\mu i}\chi_\mu \tag{1.36}$$

where $c_{\mu i}$ is the molecular orbital expansion coefficient and χ_μ corresponds to the one-electron occupied orbitals, often atomic orbitals, also called *basis functions*. N is the total number of basis functions, which are all chosen to be normalised. The smallest possible basis set is a single basis per occupied orbital on each atom in a molecular system, termed the "minimal basis". The HF limit is when the addition of further bases does not lower the energy of the system any further.

Slater type orbitals (STO) with exponential dependence $Ae^{-\alpha r}$, are the intuitive choice for atomic functions; α controls how quickly the function decays (radial extent), with higher values for higher effective nuclear charge. They are extremely similar in their mathematical expression to the real atomic orbital, however, mathematically challenging to implement in molecular orbital calculations. Gaussian type orbitals (GTO) of dependence $Ae^{-\alpha r^2}$, offer a more practically viable approximation. Linear combinations of primitive gaussians are used to form the actual basis functions. The constructed basis functions are then called contracted gaussians, and have the form:

$$\chi_\mu = \sum_p d_{\mu p}g_p \tag{1.37}$$

where $d_{\mu p}$ are fixed constants. The expansion to the MO therefore takes the form:

$$\psi_i = \sum_\mu c_{\mu i}\left(\sum_p d_{\mu p}g_p\right) \tag{1.38}$$

In this study, Pople style basis sets will be employed, with general format **X-YZg** [32]. Split valence basis sets such as these, describe the core electrons using fewer basis functions than

the interacting valence electrons; the valence electrons play a much more significant part in bonding and intermolecular interactions. An example is **6-31+G***, where the core electrons are described using a single contracted gaussian consisting of six primitive functions. The valence orbital is split into two contracted gaussians, where one is described by three primitive gaussians, and the other, one primitive gaussian. The **+** sign corresponds to diffuse functions, the extension of the basis function as it tails away from the nucleus. This is particularly important when describing the behaviour of ions. The ***** indicates the addition of polarisation functions, in this case, d-functions to all non-H atoms. Higher order modifications also add p-functions to H atoms, additional d-functions to non-H atoms, d-functions to H atoms, with increasing levels of polarisation. This mixing of orbitals facilitates a better description for the correct shape of the MO. Increasing the number of basis functions on each occupied orbital allows for expansion or contraction, increasing flexibility in response to the environment.

Basis set superposition error BSSE is a false lowering of the energy that can occur when two species in a system with finite bases sets approach one another to form a complex. Particle A borrows the extra basis functions belonging to particle B and an artificial stabilisation is observed. The error arises from the inconsistency in treatment between the individual particles at large separations, and the complex at short distances. This is particularly pertinent when performing PES scans where bond breaking or formation is expected, and in the consideration of reaction energies. The effect is particularly pronounced for smaller basis sets. Counterpoise correction can be used to circumvent basis set superposition error (BSSE); each calculation is performed twice, once using the mixed basis set of the complex and once with the separate bases of the two species, and this energy difference is subtracted from the uncorrected energies [33, 34]. However this comes at the expense of higher computational cost. Preliminary investigations into the species examined in this study showed that the use of counterpoise correction offered minimal improvements to the energy, and the additional CPU time was not proportionate to the marginal improvements. Calculations were performed at sufficiently high basis that the effects of BSSE were insignificant, and counterpoise correction was not used for further investigations.

1.3 Implementation & Analysis

The QM calculations employed in this study typically involved a geometry optimisation, followed by a frequency calculation conducted in Gaussian 09 revision E.01 (G09) [35].

This section will provide an generic overview of the methods and techniques used to prepare input or analyse the optimised geometry output from a QM calculation. Subsequent investigations into transition state structures, reaction coordinates and analysis of critical bonding points will be explained. The details of individual calculation schemes are included in the methodology section at the the start of each chapter. This includes any details of the QM methods and basis sets chosen, individual optimisation procedures, types of calculation or special keywords used, and any non-standard software or technical details of importance.

1.3.1 Molecular mechanics geometry optimisation

In the case of the larger models in this study (60 atoms and above), QM geometry optimisation was a laborious and expensive process, particularly with the presence of numerous floppy $O-H$ bonds and small methyl group rotations. In order to reduce the required time and computational cost, these structures were optimised using a low-level molecular mechanics geometry calculation to minimise large forces in the system, prior to the finer refinements made during the QM optimisation. Molecular mechanics MM uses classical Newtonian mechanics to model chemical structures and properties; the electrons are not explicitly handled, bypassing the Schrödinger's equation [36, 4]. Molecules are instead treated as a "ball on a spring", where the strength of interaction is defined by the atom types and force constants.

Each molecular mechanics (MM) approach is defined by its force field, where the energy of the system is described by a parametric function, fitted to experimental or high level computational data. Different force fields are therefore fitted to different chemical systems.

The general functional form of a force field is:

$$E_{FF} = E_{str} + E_{bend} + E_{tors} + E_{vdw} + E_{el} + E_{cross} \tag{1.39}$$

where E_{FF} is the energy of the system. The first three terms can be referred to as the 'bonding' terms: E_{str} is the energy function for bond stretching between two atoms, E_{bend} the energy required to bend a bond angle and E_{tors} is the energy of rotation around a bond. The remainder are thus called 'non-bonding' terms: E_{vdw} and E_{el} refer to the energy of non-bonding van der Waals interactions and of electrostatic interactions, respectively. E_{cross} defines the coupling of the first three terms.

In this study, the universal force field (UFF) [37] and Merck molecular force field 94 (MMFF94) [38, 39, 40, 41, 42] force fields are tested on NC dimer and trimer structures. UFF is an empirical, all-element model, in principle able to describe the whole periodic table. It has been parameterised on individual elements, hybridization and connectivity; all the atom types in the NC unit are included, and UFF has successfully been applied in the study of cellulose dissolution [43]. MMFF94 is a forcefield parameterised from high level QM calculations for small molecules, organics and proteins. It has been used to sample different torsional conformers of cellulose [44] and to study the dynamics of bio-active polysaccharides [45].

1.3.2   Potential Energy Surface scans

Geometry scans or PES scans were used to probe the local energy landscape corresponding to a specific change in geometry. During the course of a scan, a structural property - such as a selected bond length, angle or dihedral is adjusted in incremental steps, as specified by the given scan parameters. In the case of a relaxed scan, at each step, the adjusted parameter is frozen and a geometry optimisation is performed, allowing the rest of the system to relax around the modified bond. Each scan yields a PES of the explored pathway. In the case of bond breaking or formation, the presented energy profile is a reaction coordinate diagram. In these cases, an energy maximum followed by a trough indicates a transition state and intermediate reaction product, respectively. The structural co-ordinates at the peak of the curve can be extracted and used for subsequent frequency calculations or a transition state search, to validate the mechanistic pathway. Intrinsic reaction coordinate calculations also test the reactant and product along the reaction pathway, to ensure that they lie on the same PES. To explore the predicted degradation mechanisms of NC, the scanned parameters were assigned to the bonds undergoing the most significant transformation during a particular step of the mechanism. In the case that more than one significant bond was altered, multiple scans with different bond specifications were compared. In this way, multi-dimensional scans could be performed. Two-dimensional scans were used to probe simultaneous processes in the system, however, these proved computationally intensive due to the high number of coordinate points to be calculated. Relaxed geometry scans were performed on the optimised reactant geometry using the Opt=ModRedundant keyword to specify the scanned coordinate, the number of scan steps and the method for energy optimisation. A rigid scan consisted of a single point energy calculation of the structure at each

step, rather than full relaxation of the wider system, as in the relaxed scans.

1.3.3 Transition state searches

Transition state searches are called through the Opt=TS, QST2 or QST3 keywords in G09. The Opt=TS method attempts to optimise an input "guess" geometry to a maximum. The guess geometry can be drawn by hand, obtained *via* a PES scan, from coordinates in literature or generated using the QST2 function. A transition state (TS) can be identified by the single imaginary frequency corresponding to the vibration transitioning from product to reactant. Often, a TS calculation alone will not be able to isolate the correct transition state and is usually used in conjunction the QST2 or QST3 methods. The QST2 option is able to generate a transition state geometry using the Synchronous Transit Quasi-Newton (STQN) method [46]. Here, the transition geometry is assumed to be around midway between a given reactant and product; the calculation interpolates between the starting and end point, probing the energy profile. Thus, the corresponding atom labels must match in both the reactants and products. QST3 performs a similar function, but also considers an input guess transition state structure. It is widely acknowledged that transition state searching is challenging. In addition to the techniques above, the task requires a certain measure of chemical intuition when constructing guess structures, as the calculation is sensitive to small changes in geometry.

1.3.4 Solvent model

To account for solvent effects in the reactions of NC, a self-consistent reaction field (SCRF) method was applied [47]. These methods treat the solvent as a uniform dielectric constant (ε) in the background.

The solvated molecule is placed in a cavity within the SCRF. The solute dipole induces a dipole in the solvent medium surrounding the cavity, which in return leads to an electric field within the cavity called the reaction field. The shape of the cavity is dictated by the the specific SCRF approach; in this study, the polarisable continuum model (PCM) is used [48, 49]. PCM models the cavity as interlocking van der Waals radii around each atom. The charges at the van der Waals surface are split into a series of small rectangles and the value of the point charge at that surface element is calculated by:

$$q_i = -\left[\frac{\varepsilon - 1}{4\pi\varepsilon}\right] E_i \Delta S \qquad (1.40)$$

where ε is the dielectric, E_i the electric field gradient and ΔS the area of the surface element. The coulombic contribution of each surface element to the other charges are calculated and iteratively refined until self-consistent [50]. This calculated charge potential (ϕ_r) is then added to the solute Hamiltonian:

$$\mathbf{H} = \mathbf{H}_0 + \phi_r \tag{1.41}$$

and the SCF reaction continues as normal. New surface charges are calculated at each SCF cycle until the overall surface charge is also self-consistent for the optimised system. As this method only includes the electrostatic contribution, an obvious limitation to this technique is that any reactions involving direct interaction with solvent molecules, such as stablisation by solvation shells *via* van der Waals or hydrogen bonding interactions, will be missed. In these cases the explicit solvent molecules should be added. However, for models where explicit interaction with the solvent is not required but solvent dieletric properties strongly influence the reaction environment, these methods can be very effective. This method has demonstrated successful application in the study of cellulose and glucose reactions in solvent [51, 52]. For calculations in solvent, the SCRF=PCM keyword will therefore be included in G09 calculation specifications, with water (ε=78.4) as the default solvent.

1.3.5   Topology analysis using the quantum theory of atoms in molecules

Topology analysis is a method of obtaining useful properties from the 3D representation of the electron density obtained from a QM calculation. A quantitative way to obtain information on the topology of the electron density, is by taking the first derivative of the gradient ($\nabla(\rho)$). In 1991, Bader proposed a technique to analyse the electron density using the quantum theory of atoms in molecules (QTAIM) [53]. The points in the topological landscape at which $\nabla(\rho)$ is zero (excluding points at infinity) signify a stationary point. With respect to intermolecular interactions, these correspond to interaction centres, and are deemed Critical Points (CP). The matrix of partial second derivatives of the gradient is referred to as the *Hessian*. The Hessian is a (3×3) symmetric matrix; diagonalisation sets the off-diagonal terms to zero and generates the principal axes of curvature. The sum of the diagonal terms returns the laplacian of the electron density ($\nabla^2(\rho)$); evaluation of $\nabla^2(\rho)$ identifies the characteristic of the critical point (CP). In the context of electron density, the CP can be classified into four types based on the number of negative eigenvalues of the Hessian (table 1.1):

Table 1.1: Features of different types of critical point from QTAIM topological analysis.

Critical Point	Label	Negative eigenvalues	Attribute	Representation
Nuclear (NCP)	(3,-3)	3	Local maximum	Atomic nuclei
Bonding (BCP)	(3,-1)	2	2nd order saddle point	Bonding site
Ring (RCP)	(3,+1)	1	1st order saddle point	Steric point or centre of ring system
Cage (CCP)	(3,+3)	0	Local minimum	Centre of cage system

Nuclear critical points (NCP) are so called, as they are generally located at atomic nuclei positions. All three eigenvalues of the Hessian matrix of the function are negative, corresponding to a local maximum on the electron density landscape. The number of NCP is usually equal to the number of atoms, though there are exceptions, such as in Li_2 which has a greater number of NCP than atoms, and for KrH^+, with a lower number. When two eigenvalues of the Hessian matrix of a function are negative, a second-order saddle point is present. These sites are usually located between attractive atom pairs, and so are referred to as a bonding critical point (BCP). As the electron density at the BCP is closely related to bond strength, the magnitude of $\nabla^2(\rho)$ will give an indication of the bonding type [54]. If one eigenvalue of the Hessian is negative, there exists a first-order saddle point. This generally appears in the center of ring systems and highlights a local steric effect, hence it is known as a ring critical point (RCP). When none of the eigenvalues are negative, it corresponds to the local minimum. For electron density analysis, these points generally appear in the center of cage systems, such as in pyramidal structure. These are referred to as a cage critical point (CCP).

The positions of CPs are searched by the Newton method, an initial guess point must be assigned; the minimisation will always converge to the CP that is closest to the guess point. By assigning different guesses and iterating over each of them, all CPs can eventually be found. Once searches of CPs are finished, the Poincaré-Hopf relationship [55] can be used to verify that the obtained topology is self-consistent, and that all CPs are found. For an isolated system, the relationship states that:

$$n(3,-3) - n(3,-1) + n(3,+1) - n(3,+3) = 1 \tag{1.42}$$

The gradient path linking BCP, or two local maxima, can be referred to as a "bond path". Presence of a bond path indicates an atomic interaction path available for a variety bonding interactions; these will lie along covalent bonds, as well as non-covalent interactions such as intra molecular bonding or H-bonding. A network of bond paths is known as molecular graph. Scrutiny of the graph returns a reliable image of the geometry of the molecule.

Chapter 2

Model building and validation

2.1 Introduction

A wide range of reaction products are experimentally observed during the low temperature decomposition and slow ageing of NC. Small gaseous species such as CO_2, CO, CH_2O, N_2O, NO_2 were identified using IR spectroscopy, whilst the presence of larger species such as glycolic acid and oxalate were revealed by analysis of the complex reaction mixture after laboratory simulated ageing[56, 57]. Generation of these products is attributed to the range of possibleattack sites along the polysaccharide backbone and at side groups, as well as the numerous possible secondary reactions following denitration. These include depolymerisation and ring-cleavage, and can involve contaminants and acids residual in the NC matrix following synthesis. These are left behind due to imperfect washing procedures, or produced by low level ambient degradation [58, 59].

Storage conditions such as the choice of wetting solvent, temperature, pressure, humidity and fluctuations in these conditions over time, contribute to the spectrum of products evolved. This has implications for the shelf life of NC formulations; a practical example is the propellant stored under a pilot's seat for emergency ejection from the cockpit [60, 61]. The propellant device will include a mixture of energetic materials, plasticisers and stabilisers in ratios adhering to established industry safety standards. During the lifetime of the propellant, it will endure a great number of flights, each involving variable temperature and pressure cycles. Understanding of the ageing reactions will shed light on the possible interactions between the energetic materials and the stabilising mixture, informing better industrial practices, safety standards and products with improved service life.

In addition to environmental factors and contaminants, the degradation properties of NC depend on the unique polymer chain structure, largely defined by the parent cellulose

feedstock. Scanning electron micrograph (SEM) images of *Miscanthus* cellulose following nitration show a bloating of the cellulose fibres, with almost full retention of the fibre structure integrity (figure 2.1). Cellulose fibres found in nature are formed of macrofibres, which in turn are formed of microfibrils ranging from 3 - 50 nm in diameter (figure 2.2) [62]. Each microfibril is assembled from stacked polysaccharide chains held together by van der Waals and hydrogen bonding interactions. Each linear chain is formed by a sequence of individual monomer units, in this case β-D-glucopyranose. Hydrogen bonding networks determine the supramolecular arrangement of the cellulose polysaccharide chains, and variation leads to a mixture of crystalline and amorphous regions [63, 64]. Regions of high crystallinity are more difficult to penetrate by solvent, thus are more resistant to hydrolytic decomposition methods; amorphous regions are more porous, exhibit less hydrogen bonding, and are more prone to digestion by both microbes and chemicals [65]. Hydrolysis in NC is largely attributed to the presence of spent acids in the system. Small amounts of moisture present in the bulk or from the air, have also been suspected to accelerate hydrolytic ageing. The interplay of reactions between small acid species, water and the polysaccharide, in particular at the nitrate sites, are of critical importance in interpreting the mechanistic pathways leading to widespread degradation throughout the material.
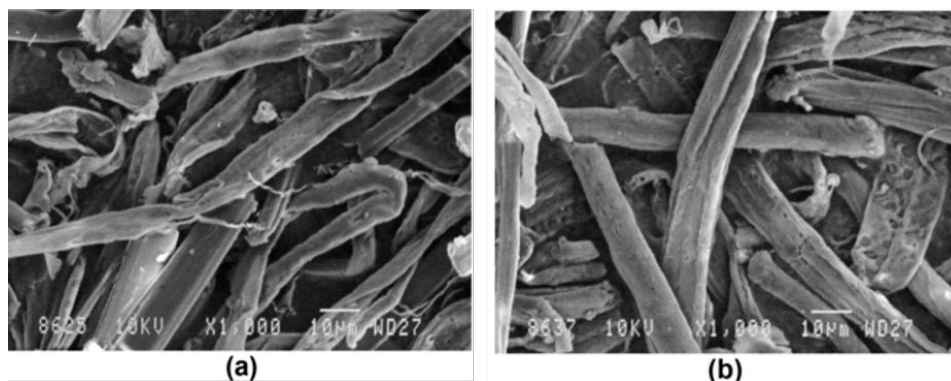
Figure 2.1: Scanning electron micrograph (SEM) images of **a)** Miscanthus cellulose and **b)** Miscanthus nitrocellulose, after nitration. From the work of Gismatulina *et al.*[66]. Reproduced with permission from the publisher.

Density functional methods are routinely used to explore the energetics of small molecular reactions [68, 69, 70]. When probing the details of individual chemical reactions using computational methods, the extended polymer structure becomes unwieldy due to the large number of atoms. It is therefore necessary to reduce the system to a representative model within a manageable scale. In 2012, Shukla *et al.* truncated the NC polymer structure to a
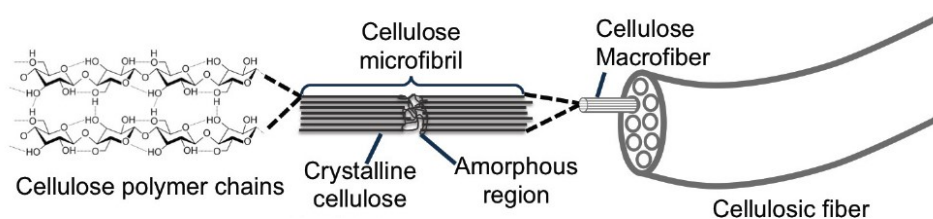
Figure 2.2: Natural cellulose fibres are constructed from individual linear strands of cellulose poly-
mer, inter-linked by hydrogen bonds to form microfibrils. The intermolecular bonding
structure between multiple strands influence degradation properties by altering the crys-
tallinity and solvent porosity of the bulk material. Adapted from the work of Dumanli
[67] with permission from the publisher.

single-ring monomer for investigation into the alkaline hydrolysis behaviour using B3LYP
DFT [71]. The study analysed the S_N2 nucleophilic attack at the nitrate-carbon site, lead-
ing to release of the nitrate ion in favour of a hydroxyl group (figure 2.3). Comparisons
between the monomer, dimer and trimer structures found the dimeric structure to be the
smallest repeat unit encompassing all bonding and non-bonding interactions, and thus the
minimum model that can fully describe the denitration behaviour of the polymer. This can
be attributed to the 1→4 glycosidic linkage between each of the β-D-glucopyranose rings.
The angle of the glycosidic oxygen leads to an alternating, non-planar orientation for each
additional ring added (figure 2.4) giving rise to inter-ring interactions and steric effects that
cannot be observed in the monomer.

In this chapter, the electronic properties of the monomer, dimer and trimer truncations
of the NC polymer were compared. The most suitable model size for subsequent mecha-
nistic investigations was determined with consideration for accurate representation of the
chemistry of the full system, within the limitations of computational resource. Hydroxyl
(-OH) and methoxy (-OCH$_3$) capping groups were tested at chain ends in the C1, C4 posi-
tions, to explore their interaction with the glucopyranose rings and effect on the distribution
of charge on the chosen model.

2.2 Methodology

2.2.1 Geometry optimisation

The monomer starting structure was constructed using the geometry of β-D-glucopyranose
obtained from literature [72], with the substitution of three nitrate groups at each of the
carbon 2, 3 and 6 sites. For dimer and trimer structures, additional glucopyranose rings
were appended to the first ring in a 1→4 position, with alternating planarity (figure 2.4).

Each unit was capped with either methoxy or hydroxyl groups and geometry optimised using quantum mechanical (QM) methods.

Selected dimer and trimer molecules were pre-optimised with a MM using UFF [37] and MMFF94 [38, 39, 40, 41, 42] force fields. This was to determine whether an initial 'rough' optimisation using a less expensive MM method could lead to a reduction in the QM optimisation time for the larger structures, or facilitate easier identification of global minimum structures. The UFF force field was chosen as a general all-element model; MMFF94 was parameterised for organic compounds and includes hydrogen bonding.

Following MM pre-optimisation, the dimer cases did not show any notable speed-up in convergence on the minimised structure, or any significant difference in the final optimised geometry. Further investigations did not implement MM pre-optimisation for dimer geometries.

Minimisation of trimer geometries proved more challenging, oftentimes with conver-

● oxygen   ● nitrogen   ● carbon   ○ hydrogen
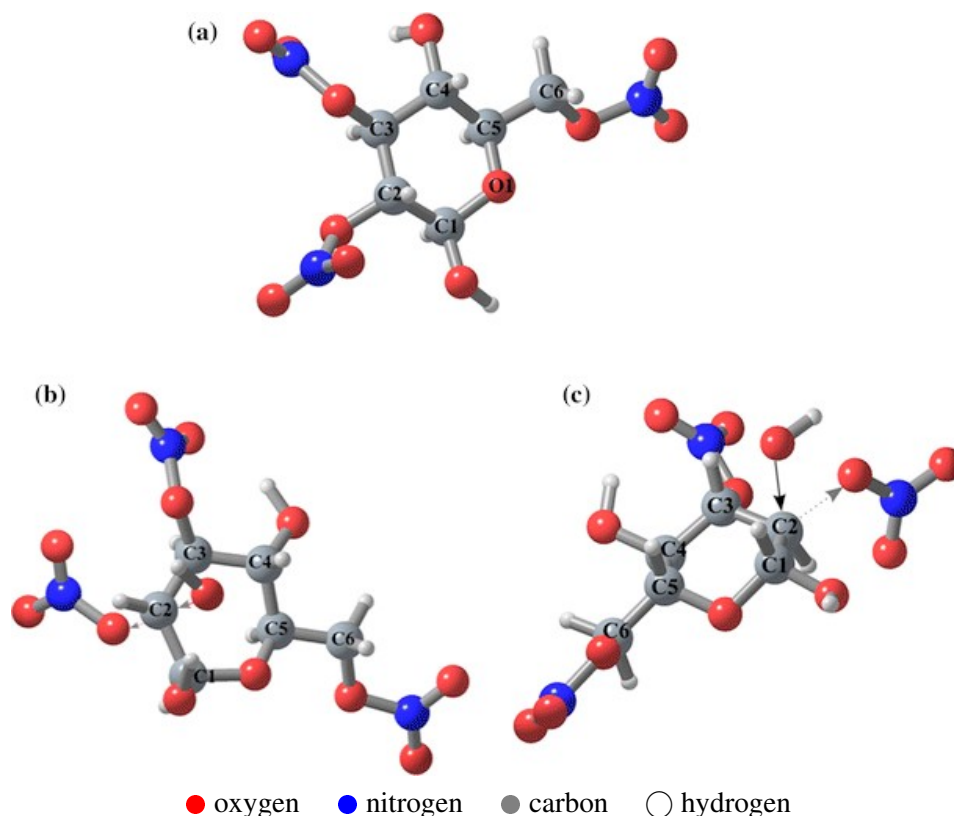
Figure 2.3: a) Numbering scheme of 2,3,6-trinitro-β-D-glucopyranose, as a monomer of NC. **b)** Transition state showing S_N2 (opposite side) attack by OH⁻ and **c)** angular attack (same side) by OH⁻ during the addition–elimination process at the C2 site of NC from the work of Shukla *et al.* The solid arrow indicates nucleophilic attack and the dashed arrow the leaving group. Reproduced with permission from the publisher.

gence failure, due to the presence of many floppy bonds and high degrees of rotational freedom for hydrogen atoms and along side chains. This lead to a smooth, slow evolving potential energy surface that is difficult to explore using gradient optimisation methods. MM pre-optimisation of the bi-methoxy capped trimer structure generated a starting input geometry for QM optimisation that enabled faster convergence to a final structure, reducing the number of steps required. However, it was found that a trimer input geometry derived from an already-optimised dimer structure, with duplication of the first ring and appending it to the end of the chain (figure 2.4(c)), provided a lower energy starting conformer and more stable optimisation procedure. Thus, rather than construction of a new trimer geometry "from scratch", the trimer structures used in the study were constructed from extension of the fully optimised dimer structures.

In some instances, it was found that the final optimised geometries varied according to the input starting geometry. In the cases of more than one possible converged geometry for the same species, the conformer with lowest absolute energy was chosen.

(a) Monomer with DOS=3.
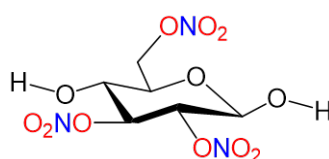
(b) Dimer with DOS=3.
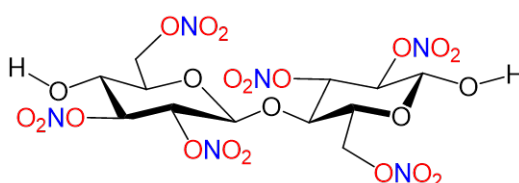
(c) Trimer with DOS=3, constructed from the dimer.
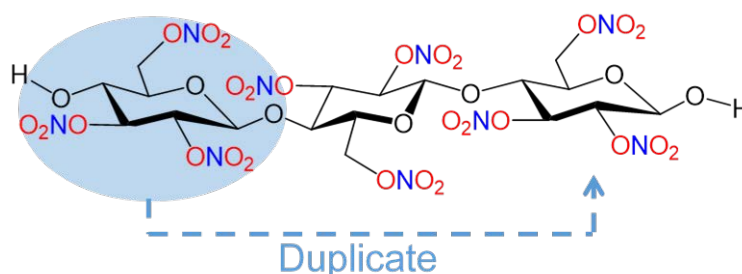
Figure 2.4: Truncated NC units, whereby each additional glucopyranose ring is added in the 1→4 position, as in the structure of cellulose. The trimer was constructed from the optimised dimer, with duplication of the first ring (shown with the blue arrow). The degree of substitution (DOS) refers to the replacement of the cellulose hydroxyl side groups for nitrate groups.

2.2.2 Labelling system

The numbering scheme for structures is detailed in figure 2.5. Counting from the oxygen of the first glucopyranose ring as atom 1 (O1), the numbering of carbons proceeds in a clockwise direction. For simplicity, the nitrate groups are numbered 1 - 3, also moving clockwise around the ring. The oxygen linking the nitrate to the ring is labelled (Ox). Oxygen on the terminal ends of the nitrate group are labelled (Ot). Identical oxygen labelling is applied across all nitrate groups.

Labels are given from the largest structure to the smallest: [ring; substituent group; component atoms]. For example, a terminal oxygen (Ot) on the nitrate at the C6 position (N3) of the second ring (R2), would be referred to as R2N3Ot. When referring to only the nitrogen of this nitrate, the label would be R2N3. For the carbon at the C6 position on the second ring, the label would be R2C6.

2.2.3 System size and chain ends

In order to investigate the influence of different capping groups, the fully nitrated dimer structure was used as a reference, following the minimum complete structure approximation established by Shukla *et al.*. Chain ends were capped with methoxy groups, or a combination of a methoxy and a hydroxyl groups (figure 2.6). The differences in charge distribution and the nature of intra-molecular interactions were probed using QTAIM and inspection of the electrostatic potential (ESP) around the molecule. When considering the system size, the ESP and QTAIM topology analyses were compared across monomer, dimer and trimer models. To simplify optimisation of the trimer structure and to explore interactions at lower degrees of substitution, nitration was limited to the C2 site. The C2 position was found by Shukla *et al.* to be the first to be nitrated, and last to be denitrated [71]. The monomer was nitrated only at C2, the dimer nitrated only at R1C2 and the trimer nitrated at R1C2 and R3C2.

2.2.4 Computational details

The B3LYP functional was chosen for initial exploration of the electronic properties of the system. It is an efficient and extensively benchmarked method for main group elements, suitable for the current model system size, where the largest trimer extends to 76 atoms[70, 73, 74]. All electronic structure calculations in this section, including geometry optimisation and thermodynamic calculations were performed in vacuum to the level of B3LYP/ 6-311+G(d,p) with tight convergence criteria (table 2.1), implemented in the G09

Figure 2.5: The numbering scheme for dimers used in this study. Ring 1 (R1) is the first ring, whereby oxygen (O1) is *one bond* separated from the glycosidic oxygen linking the two rings. Ring 2 (R2) is where O1 is *two bonds* separated from the glycosidic oxygen. The nitrate oxygen on the terminating ends are referred to as (Ot), and the nitrate oxygen connected to the glucopyranose ring is referred to as (Ox).
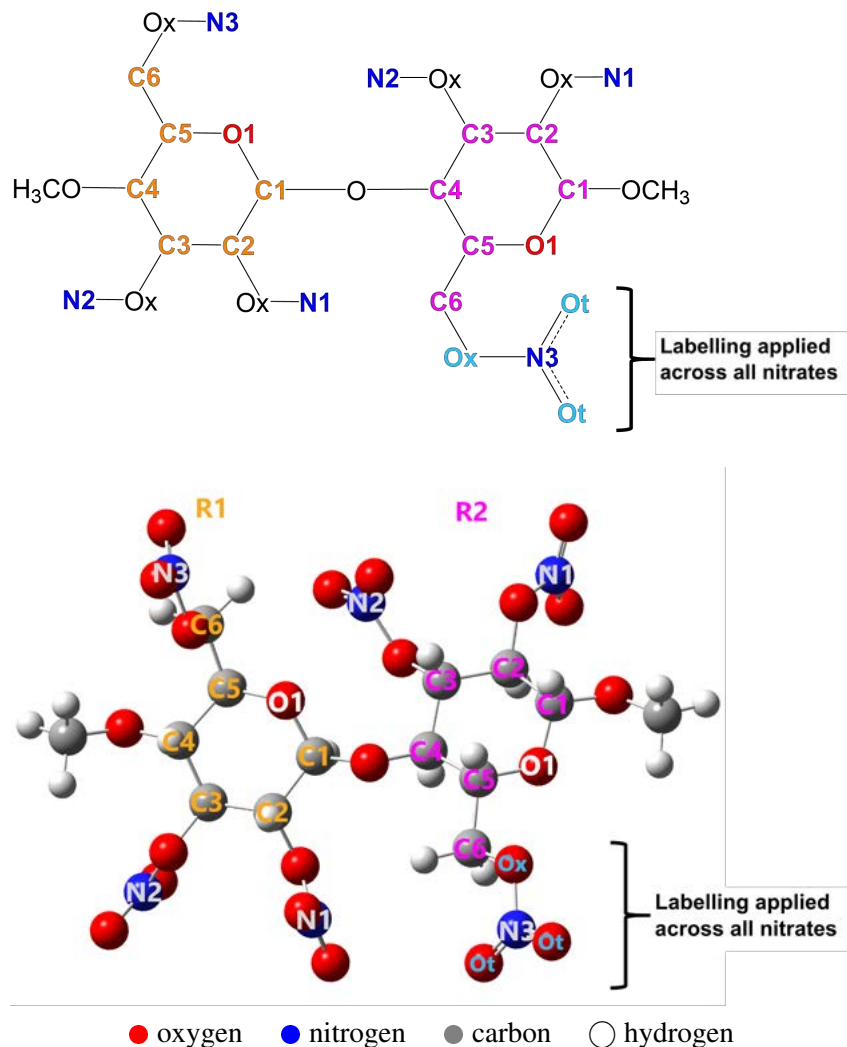
quantum chemistry suite [35].

Table 2.1: Convergence criteria used in G09. Units in Hartree/Bohr.

Convergence criteria	Normal	Tight
Maximum Force	4.5×10^{-4}	1.5×10^{-5}
Root Mean Square Force	3.0×10^{-4}	1.0×10^{-5}
Maximum Displacement	1.8×10^{-3}	6.0×10^{-5}
Root Mean Square Displacement	1.2×10^{-3}	4.0×10^{-5}

Structures were built using the Gauss View 5.0.8 (GView) graphical user interface [75]. Molden 5.0.2 [76, 77] and GView packages were used for visualisation. Avogadro

molecular editor 1.1.1 [78] was used for MM pre-optimisation. UFF and MMFF94 force fields were applied with Steepest Descent algorithm [79, 80] with 500 steps and energy convergence of 1×10^{-7} kJmol^{-1}. Electrostatic potential (ESP) surfaces were mapped to the electron density, extracted from G09 formatted checkpoint files following optimisation. Gaussian's CubeGen utility was used to generate the 3D point grids for mapping; density and ESP cubes were generated with 80^3 points (default grid point density). ESP maps were visualised using GView. QTAIM topological analyses including CP analysis on the optimised structures were performed using MultiWFN 3.6 [81].

2.3 Truncating the polymer

2.3.1 Comparison of capping groups

Fully nitrated dimers (DOS=3) were bi-capped with methoxy (CH_3/CH_3), methoxy-hydroxyl (CH_3/OH) or hydroxy-methoxy (OH/CH_3) groups at C1 and C4 positions (figure 2.6). The effect of each capping group combination on the dimer geometry, electronic properties and intramolecular non-bonding interactions within the dimer were inspected.

QTAIM electron density topology analysis of all dimers revealed notable intermolecular interaction across the two rings, in particular where the C6 side chain was able to interact with the nearest nitrate group of the opposite ring (figure 2.7). All three capping group combinations presented similar characteristics; nuclear critical points (NCP) lay at all atomic sites and each chemical bond was described by a BCP. Ring critical points (RCP) lay at ring centres and at points of concentrated steric interference within side chain moieties. A single CCP was observed in the region between R1C5 - R1C6 - R2N2, where the arrangement of the side chains formed a pyramidal cage-like environment (table 2.2).
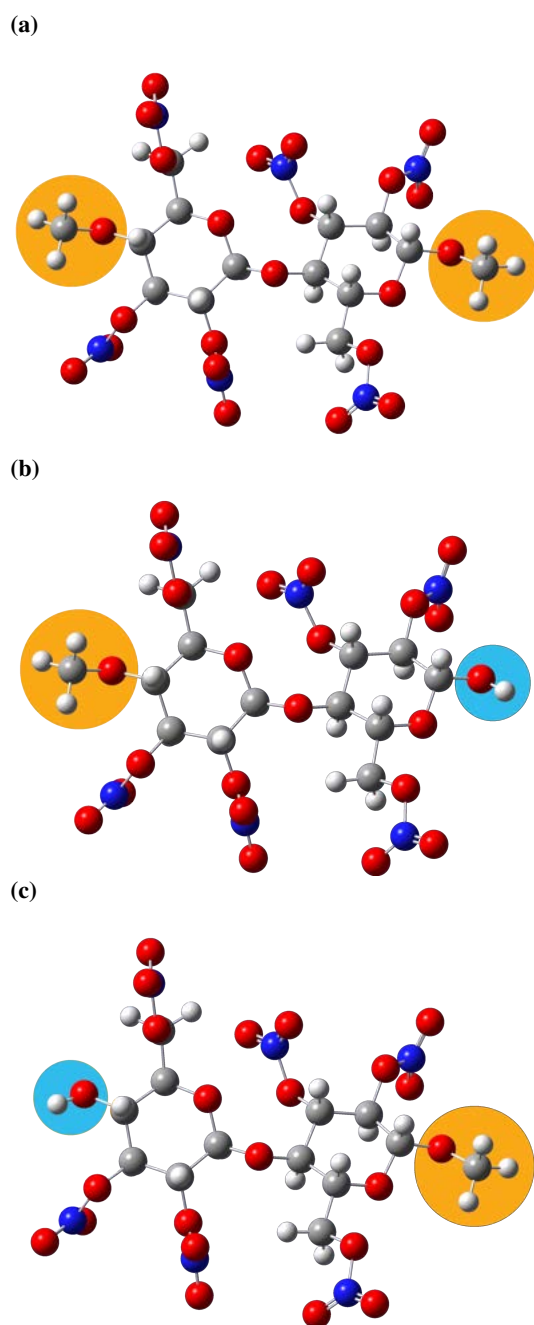
(a)

(b)

(c)

Figure 2.6: Fully nitrated NC dimer with **a)** methoxy groups capping chain ends on both ring 1 and ring 2 (CH_3/CH_3), **b)** a methoxy capping group on ring 1 and hydroxyl on ring 2 (CH_3/OH), **c)** hydroxyl group on ring 1 and methoxy capping group on ring 2 (OH/CH_3).

Figure 2.7: All critical points identified by QTAIM topology analysis. Nuclear critical points (NCP are located at atomic nuclear sites, bonding critical points (BCP), (● orange spots) lie on chemical bonds, or on intramolecular bonding paths (— shown in orange); ring critical points (RCP) (● yellow spots) denote centres of steric interaction and the cage critical point (CCP) (● green spot) shows the centre of a cage-like system.

(a) Critical points idenitified for the CH_3/CH_3 dimer.
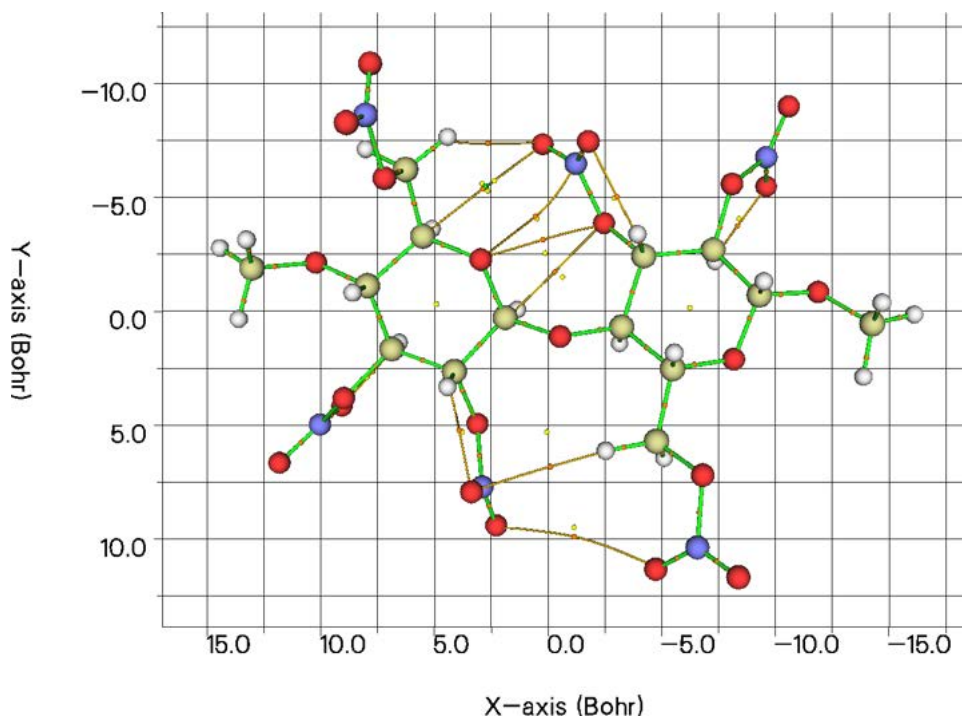
(b) Critical points for the CH_3/OH dimer.
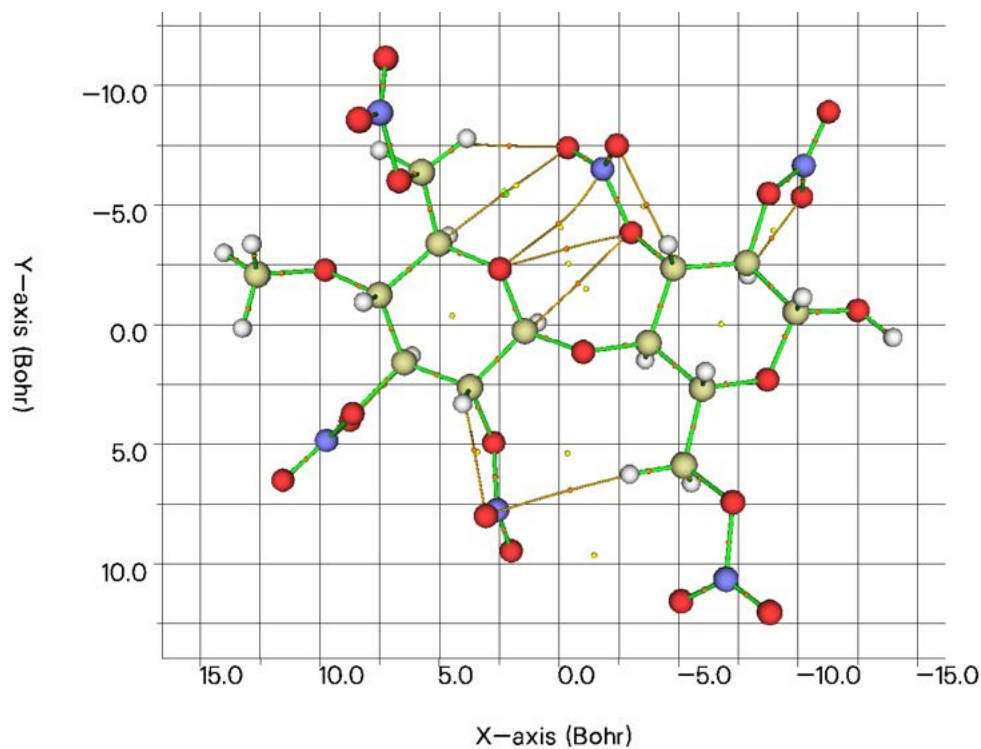
Figure 2.7: Continued.

(c) Critical points for OH/CH$_3$ dimer.
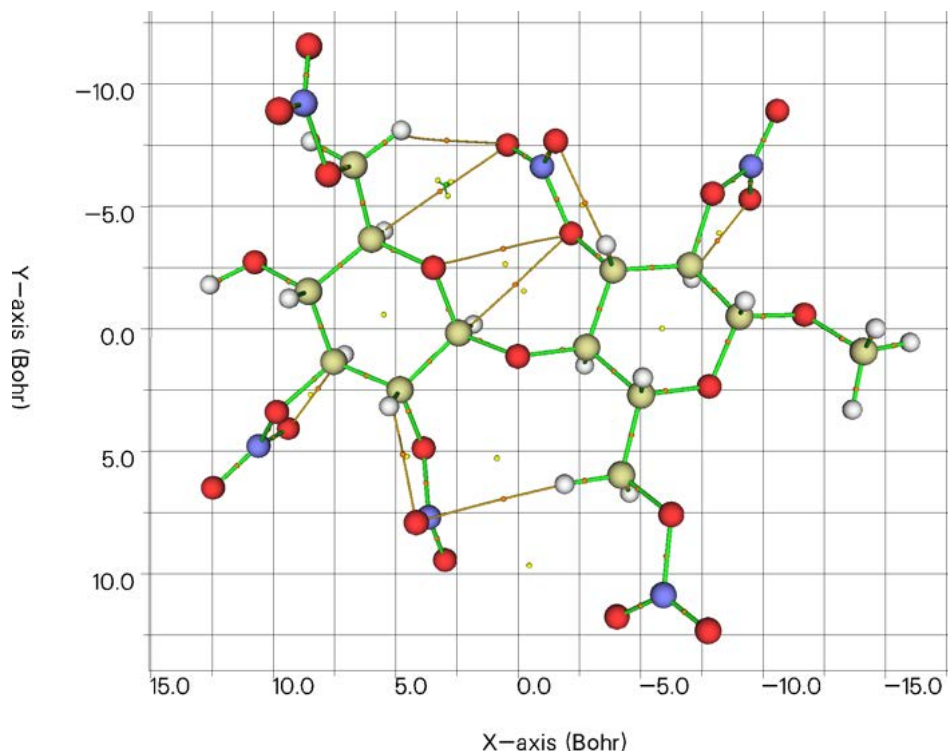
Hydrogen bonding was observed between the nitrate groups directly connected to the ring and their associated α-hydrogens (figure 2.8). N1 and N2 nitrates are orientated in the eclipsed conformation relative to the α-hydrogen, bringing the terminal nitrate oxygen within H-bonding distance and generating a steric critical point between the oxygen and α-hydrogen (table 2.3). This was not the case for C6 nitrates, which are not directly connected to the ring. The flexibility of the C6 alkyl chain allows for relaxation of the nitrate to the gauche orientation, relative to the CH$_2$ group. The increased distance between the terminal oxygen of the nitrate and the α-hydrogens exceeded H-bonding distance and reduced steric crowding.
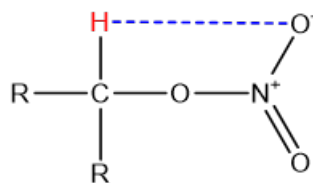

Figure 2.8: α-hydrogen relative to the nitrate group, highlighted in red; the terminal oxygen (Ot) - α-H interaction is highlighted in blue.

Table 2.2: Topology analysis of dimers with capping groups. * CH_3/CH_3 and CH_3/OH only; ** CH_3/CH_3 only ; *** Intramolecular steric centres located between rings, and between nitrate groups and nearest α-hydrogen on the ring.

Dimer	CP type	Number	Interaction centres	Intramolecular bonding
	NCP	63	All atomic nuclei	-
CH_3/CH_3	BCP	75	64 chemical bonds 11 intramolecular bonds	**R1 - R1** R1C2H - R1N1Ot **R2 - R2** R2C3H - R2N2Ot R2C2H - R2N1Ot **R1 - R2** R1C3H - R1N2Ot R1C6H - R2N2Ot R1C5H - R2H2Ot R1O1 - R2N2* R1O1 - R2N2Ox R1C1H - R2N2Ox R2C6H - R1N1Ot R1N1Ot - R2N3Ot**
	RCP	14	R1, R2 ring centres, Steric centres***	-
	CCP	1	R1C5 - R1C6 - R2N2	-
	NCP	60	All atomic nuclei	-
CH_3/OH	BCP	71	61 chemical bonds 10 intramolecular bonds	**R1 - R1** R1C2H - R1N1Ot **R2 - R2** R2C3H - R2N2Ot R2C2H - R2N1Ot **R1 - R2** R1C3H - R1N2Ot R1C6H - R2N2Ot R1C5H - R2H2Ot R1O1 - R2N2* R1O1 - R2N2Ox R1C1H - R2N2Ox R2C6H - R1N1Ot
	RCP	14	R1, R2 ring centres,***	-
	CCP	1	R1C5 - R1C6 - R2N2	-
	NCP	60	All atomic nuclei	-
OH/CH_3	BCP	70	61 chemical bonds 9 intramolecular bonds	**R1 - R1** R1C2H - R1N1Ot **R2 - R2** R2C3H - R2N2Ot R2C2H - R2N1Ot **R1 - R2** R1C3H - R1N2Ot R1C6H - R2N2Ot R1C5H - R2H2Ot R1O1 - R2N2Ox R1C1H - R2N2Ox R2C6H - R1N1Ot
	RCP	13	R1, R2 ring centres,***	-
	CCP	1	R1C5 - R1C6 - R2N2	-

Table 2.3: Distances between terminal oxygen of nitrates and nearest α-hydrogen.

Nitrate oxygen	Nearest α-H	Distance / Å	Dihedral	Conformation
R1				
R1N1Ot	R1C2H	2.2	-3.5	Eclipsed
R1N2Ot	R1C3H	2.1	2.6	Eclipsed
R1N3Ot	R1C6H	2.5	25.4	Gauche
R2				
R2N1Ot	R2C2H	2.2	3.4	Eclipsed
R2N2Ot	R2C3H	2.2	9.4	Eclipsed
R2N3Ot	R2C6H	2.5	-24.9	Gauche

Inter-ring H-bonding occurred between C6 hydrogens and the terminal oxygens of the nearest nitrate on the other ring (at the C3 position), in addition to N - O interactions and O - O interactions. Upon replacement of a hydroxyl capping group for a bulkier methoxy, the geometry of the nitrate groups adjusted to accommodate. It can be seen in the case of CH_3/CH_3 in figure 2.7.a), that there is an additional BCP and intramolecular bonding path between R1N1Ot and R2N3Ot that was not present in the structures with only one methoxy group, and an R1O1 - R2N2 interaction that is not present i n OH/CH_3. Inspection of nitrate-nitrate distances show that with substitution to methoxy capping groups, the inter-nitrate distances did not change significantly (table 2.4). Despite a lower number of intramolecular bonding interactions, OH/CH_3 did not exhibit larger bonding distances between interaction centres.

Table 2.4: Distances between nitrate groups across different capping group combinations show that the nitrate geometries between rings in the dimer remain the same regardless of capping group.

Capping group	Nitrate-nitrate pair	Distance / Å
	R1N1 - R1N2	4.0
	R1N1 - R2N3	4.8
CH_3/CH_3	R1N3 - R2N2	5.2
	R2N2 - R2N1	4.1
	R1N1 - R1N2	4.0
	R1N1 - R2N3	4.8
CH_3/OH	R1N3 - R2N2	5.2
	R2N2 - R2N1	4.1
	R1N1 - R1N2	4.0
	R1N1 - R2N3	4.8
OH/CH_3	R1N3 - R2N2	5.3
	R2N2 - R2N1	4.1

Figure 2.9: Critical points identified by QTAIM topology analysis of NC dimer nitrated at C2 position for **a)** NC repeat unit with two $-OCH_3$ capping groups (CH_3/CH_3) dimer, **b)** CH_3/OH dimer and **c)** OH/CH_3 dimer. Nuclear critical points (NCP are located at atomic nuclear sites, bonding critical points (BCP), (● orange spots) lie on chemical bonds, or on intramolecular bonding paths (— shown in orange); ring critical points (RCP) (● yellow spots) denote centres of steric interaction and the cage critical point (CCP) (● green spot) shows the centre of a cage-like system.

(a) CH_3/CH_3 dimer
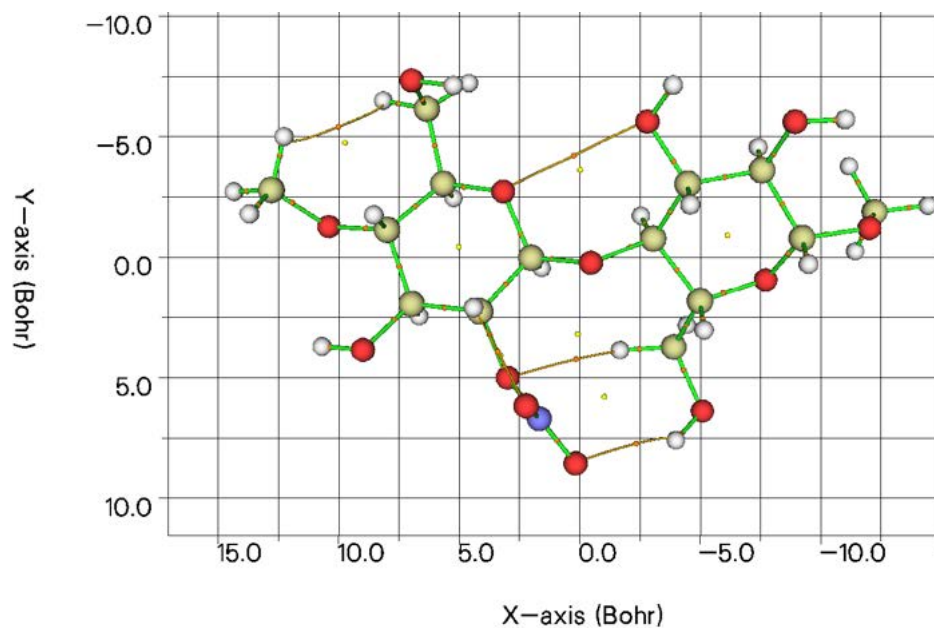
(b) CH_3/OH dimer
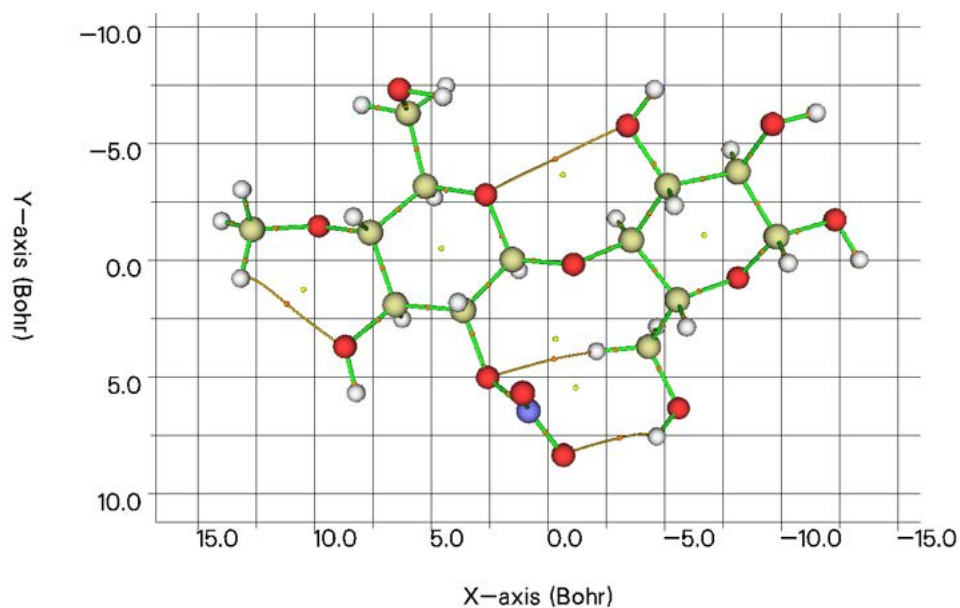
Figure 2.9: Continued.

(c) OH/CH$_3$ dimer
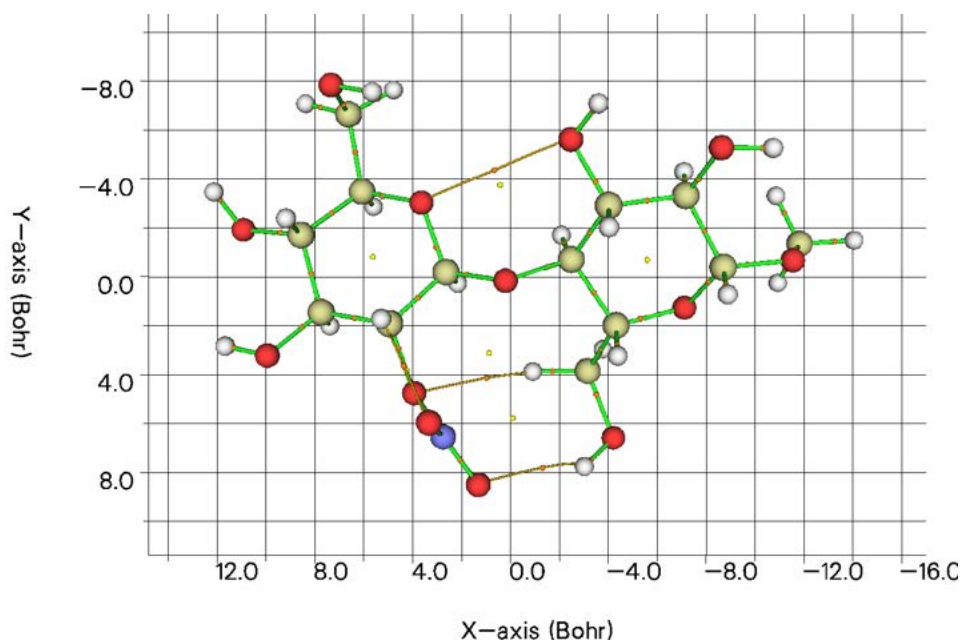
Topology analysis on dimers with lower levels of nitration show an interaction between unsubstituted hydroxyl side chains with the capping group on ring 1 (figure 2.9). NC dimers nitrated at only the R1C2 position exhibit H-bonding and H-H interaction between the capping group hydrogens and those of C6, and O-O interactions between R1O1 and hydroxyl oxygens at R2C3. As was observed in the fully nitrated dimer (fig 2.7), change of the capping group partially influences the change of geometry around the interacting sites, though not necessarily nitrate-nitrate distances (2.4). Comparison of the torsion angle between the two rings when different end groups are attached to the dimer reveals that OH/CH$_3$ combination leads to a small 0.6 ° increase in the relative rotation (table 2.5). Though this may appear marginal, any alteration in the twisting configuration between rings will modify the

Table 2.5: Torsion angles between the two rings in the R1C2 nitrated dimer (DOS=1), when capping groups are modified shows that the NC repeat unit with −OH capping group on ring 1 and −OCH$_3$ group on ring 2 (OH/CH$_3$) combination presents a greater twist between the rings.

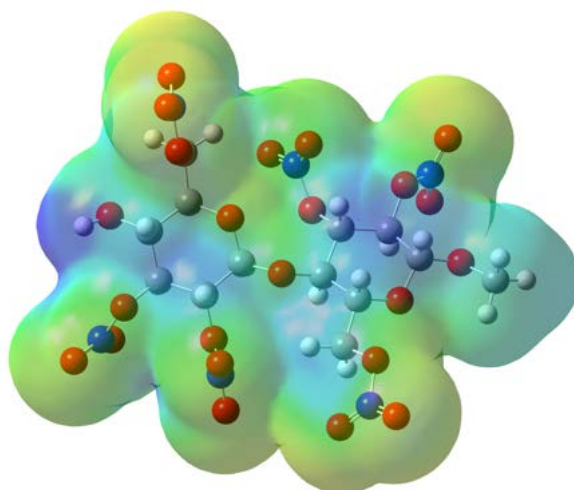| Dimer	Ring torsion angle
CH$_3$/CH$_3$	-177.1
CH$_3$/OH	-177.1
OH/CH$_3$	-176.5
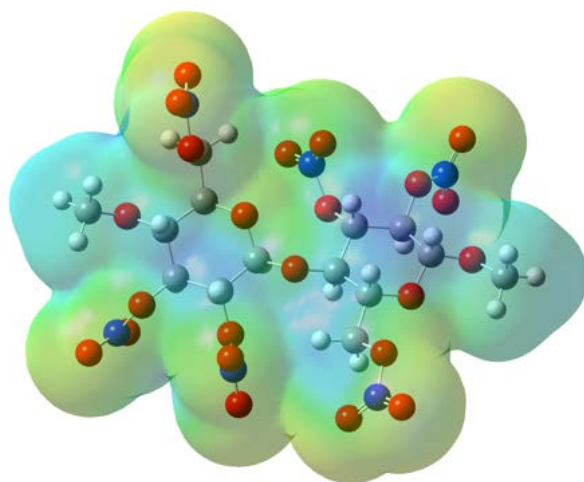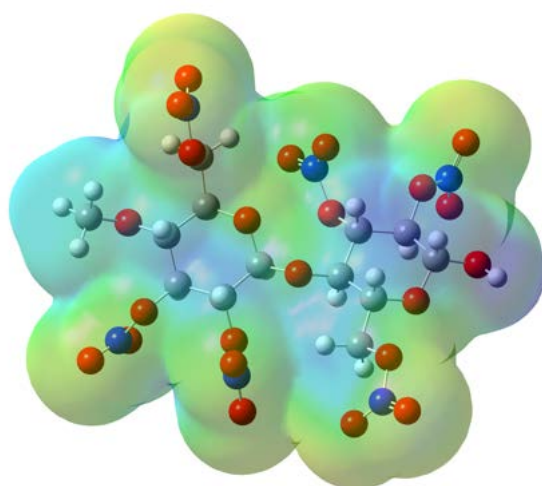
Figure 2.10: Electrostatic potential maps of NC dimers fitted with different capping group combinations in order to inspect the change in charge distribution, **a)** CH_3/CH_3, **b)** CH_3/OH, **c)** CH_3/OH.

strength of the R1N1 - R2C6 hydroxyl and the R1O1 - R2C3 hydroxyl interaction, offering increase stabilisation of the R1N1 nitrate group (figure 2.9c). However in this case the magnitude of the change is unlikely to significantly induce a change in reactivity.

The ESP maps represent the charge density around the molecule (figure 2.10). A more negative value (increasingly red) indicates an area of higher electron density, whilst a more positive value (increasingly blue) indicates an area of lower electron density. It can be seen that the areas with lowest electron density lie around the centre of the glucopyranose rings and at the C6 position of the side branches. This can be explained by the number of adjacent oxygens drawing the electron density away from the less electronegative alkyl groups. The most electron rich areas are the outermost oxygens of the nitrate groups (Ot positions). The terminal oxygens draw electron density from the nitrogen lone pairs and are resonance stabilised. The presence of the hydroxyl capping group promotes a small decrease in the concentration of electron density around the adjacent ring. This is illustrated by the slight deepening of the blue shading around the ring directly bonded to the hydroxyl. The hydroxyl group itself presents the lowest concentration of electron density, suggesting that the terminating hydrogen may be prone to nucleophilic attack. For the extended polymer, it is expected that the electron-density profile of each glycosidic oxygen between monomers is analogous. Capping groups should therefore mimic the charge density around the central oxygen of the dimer, as closely as possible. The oxygen of both methoxy and hydroxyl capping groups exhibit a lower concentration of electron density than that of the bridging oxygen between the two rings. This deficiency is particularly pronounced in the case of the hydroxyl capping group, suggesting that the methoxy group provides a more representative approximation for the extended polymer with respect to charge density. Whilst a terminating hydroxyl end group provides a useful proxy for the polymer chain ending, the methoxy groups more accurately mimic the charge distribution, geometry and intramolecular bond character within the chain, without addition of artificial capping group interactions.

2.3.2 Model size

The electrostatic potential and topology analysis of the partially nitrated monomer, dimer and trimer were compared in order to explore the limitations of each truncation. The monomer was nitrated at C2, the dimer at R1C2 and trimer model nitrated at R1C2 and R3C2 sites. Analysis of the CPs in the monomer revealed steric centres and a non-bonding interaction with the capping group. The terminal oxygen - α-hydrogen interaction at the C2

Figure 2.11: Electrostatic potential (ESP) maps of NC monomer, dimer and trimer units.

(a) ESP map of NC dimer nitrated at the C2 position.
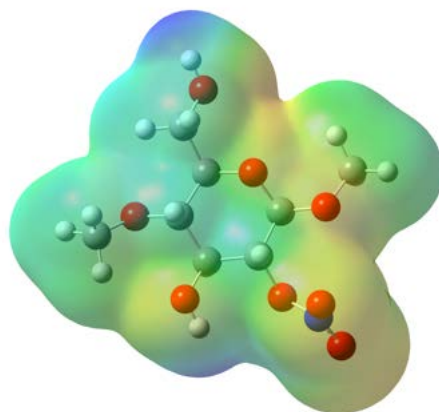
(b) ESP map of NC dimer nitrated at the R1C2 position.
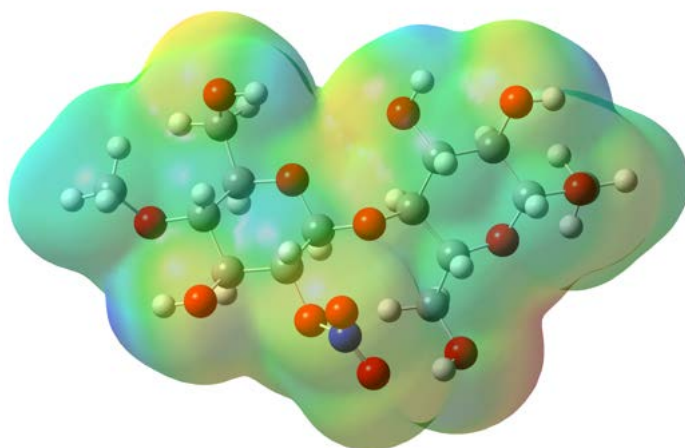
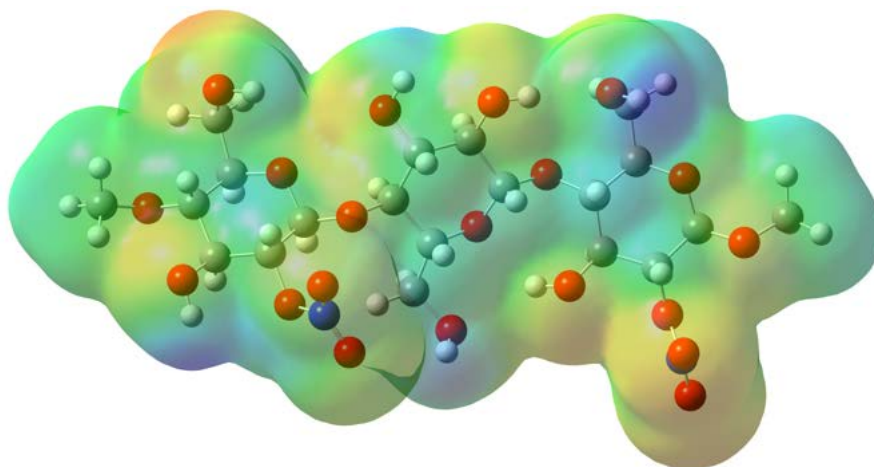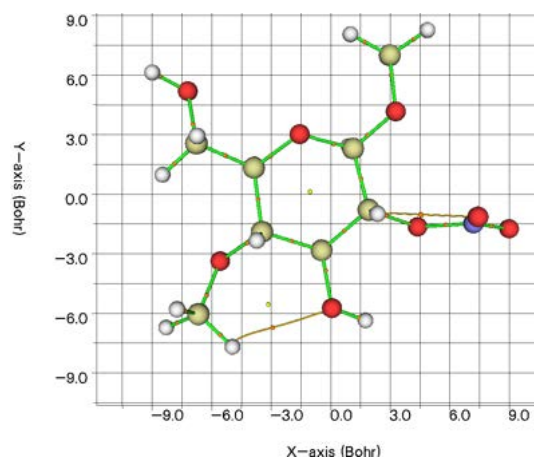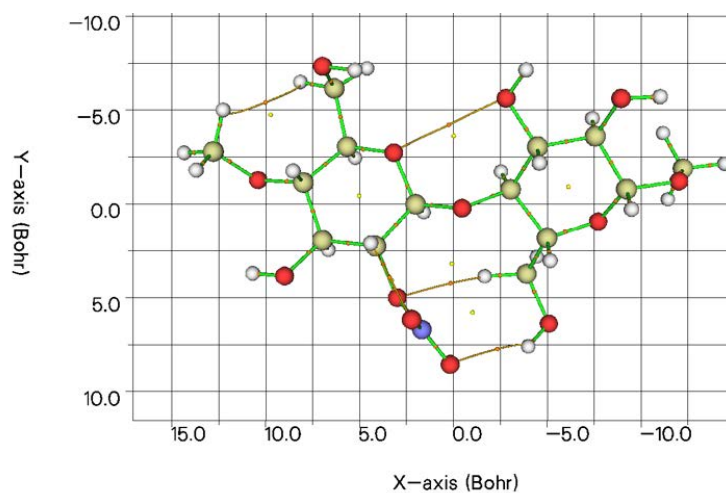**(c)** ESP map of NC trimer nitrated at R1C2, R3C2.

Figure 2.12: Critical point analysis of NC monomer, dimer and trimer units. Bonding critical points (BCP), (● orange spots) lie on chemical bonds; intramolecular bonding paths (— shown in orange); ring critical points (RCP) (● yellow spots) denote centres of steric interaction and the cage critical point (CCP) (● green spots) shows the centre of a cage-like system.
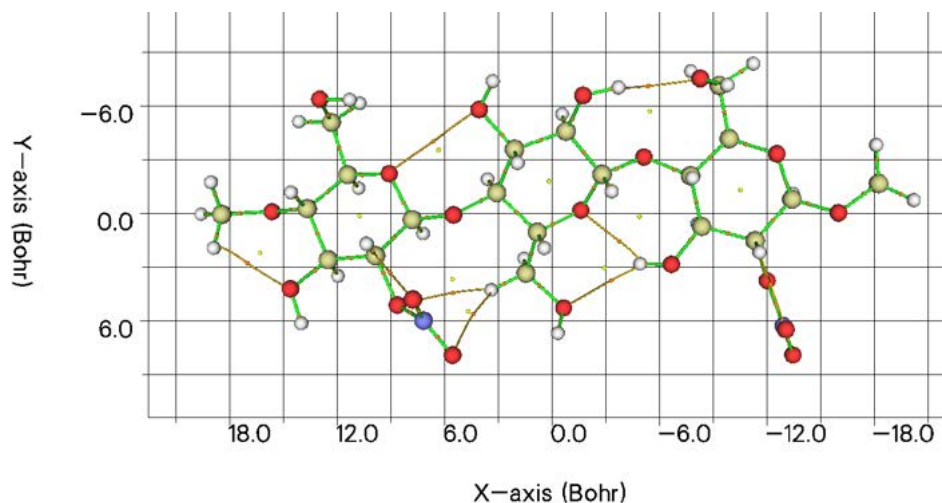
(a) Critical point analysis of NC monomer nitrated at C2 position.

(b) Critical point analysis of NC dimer nitrated at R1C2 position.

(c) Critical point analysis of NC trimer nitrated at R1C2, R3C2.

nitrate was observed, as was seen in the fully nitrated systems (figure 2.11c)). The trimer unit displayed a more extensive network of hydrogen bonding between rings, facilitated by the higher number of unsubstituted hydroxyl groups on the second ring (figure 2.11c)). Compared with the dimer and trimer models, the monomer presents all the intra-ring interactions observed in the larger units, omitting only the between-ring interactions. Though Mulliken charges are highly variable with basis set and the inclusion of diffuse functions, they may offer a general overview of the relative partial charge distribution in the molecule. Figure 2.13 and table 2.6 display the Mulliken charges of each of the different sized models. The large difference in charges for the C1 capping oxygen between monomer and the larger models is due to the absence of a second connected ring. Carbon sites within the glucopyranose ring present the greatest variation between each model. Attention to the changes in orientation of the side chains offer explanation for the observed charge distribution. The orientation of the C4 capping group is slightly altered for the dimer, as compared to the monomer and trimer, leading to the more negative charge at C4 for the dimer. The geometry of the nitrate at the C2 site is also most similar for the monomer and trimer, explaining the contrast between the charge concentration at C2 for these two species and the dimer. The Mulliken charges are therefore extremely sensitive to fine alterations in the geometry and should not be taken as a reliable measure for the charge distribution.

Whilst the monomer lacks the essential interactions between rings and side chains present in the polymer, when exploring the chemistry of a localised group of atoms - such as in the case of the denitration reaction - it is a suitable approximation for a primary investigation into the mechanistic details at these key reaction sites. The validated mechanisms can then later be expanded to the dimer and larger systems to re-introduce ring-ring interactions and higher steric effects. As such, the monomer structure offers a compromise of computational efficiency and accurate representation for the geometry, partial charges and intra-ring non-bonding interactions of the larger system.

Figure 2.13: a) NC monomer nitrated at C2. **b)** Monomer a) shaded by Mulliken charges. More negative atoms are shaded in red whilst more positive atoms are shaded in green. Scale bar ranges between ±0.5 a.u..
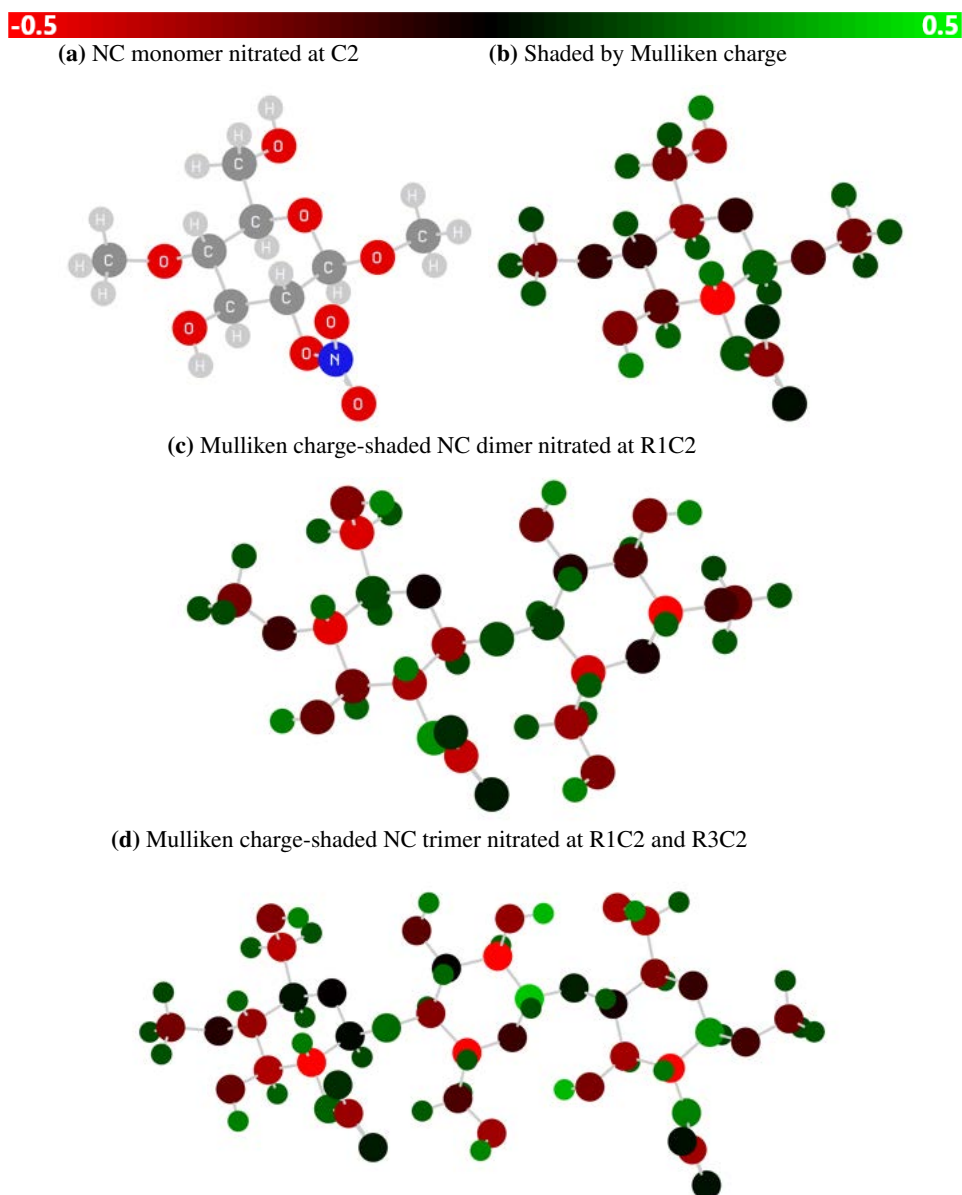

(a) NC monomer nitrated at C2

(b) Shaded by Mulliken charge

(c) Mulliken charge-shaded NC dimer nitrated at R1C2

(d) Mulliken charge-shaded NC trimer nitrated at R1C2 and R3C2

Table 2.6: Comparison of Mulliken charges for the CH_3/CH_3 monomer and the first glucopyranose ring (R1) of the dimer and trimer, all nitrated in the C2 position. Charges are expressed in a.u.. For explanantion of labelling scheme, see section 2.2.2. Shaded values indicate charge differences greater than ±0.1 a.u.

R1 Atom	Monomer	Dimer	Trimer	ΔTrimer-Dimer	ΔTrimer-Monomer
O1	−0.1	−0.0	−0.0	0.0	0.1
C1	0.2	−0.3	0.0	0.3	−0.2
C1H	0.1	0.1	0.1	0.0	0.0
C1 Ocap	−0.2	0.2	0.2	0.1	0.4
C2	−0.6	−0.3	−0.6	−0.3	0.0
C2H	0.2	0.2	0.2	0.0	0.0
N1Ox	0.2	0.3	0.2	−0.1	0.0
N1	−0.3	−0.4	−0.3	0.1	−0.0
N1Ot1	0.0	0.1	0.1	0.0	0.0
N1Ot2	0.1	0.1	0.1	0.0	0.0
C3	−0.2	−0.2	−0.3	−0.1	−0.2
C3H	0.2	0.2	0.2	0.0	0.0
C3O	−0.2	−0.2	−0.2	−0.0	0.0
C3OH	0.3	0.2	0.2	0.0	−0.0
C4	−0.1	−0.4	−0.3	0.2	−0.2
C4H	0.2	0.2	0.2	0.0	0.0
C4 Ocap	−0.1	−0.1	−0.1	0.0	0.0
C5	−0.3	0.1	0.0	−0.1	0.3
C5H	0.2	0.2	0.2	0.0	−0.0
C6	−0.2	−0.4	−0.4	0.1	−0.1
C6H1	0.2	0.2	0.2	0.0	0.0
C6H2	0.2	0.2	0.2	−0.0	−0.0
C6O	−0.3	−0.3	−0.3	0.0	0.0
C6OH	0.2	0.3	0.3	−0.0	0.0

2.4 Summary

In this section the polymer structure of NC was truncated to a system size suitable for application of density functional theory, for use in subsequent investigation into the decomposition mechanisms. Methoxy and hydroxyl capping group approximations were compared. ESP maps showed that the methoxy group performed better, exhibiting a charge density more similar to that of the glycosidic oxygen in larger polymer chain units. Topological analysis using QTAIM highlighted non-bonding interactions between both hydroxyl and methoxy chain endings with side chains of the dimer. Findings showed that the methoxy capping group provided a more sterically and chemically similar approximation for the extended polymer, and was adopted for work in further chapters.

Topological analysis of monomer, dimer and trimer models found that the 2-ring and

3-ring systems were the most consistent with respect to charge density distribution and profile of intramolecular interactions. It was assumed that the largest model would be most representative of the polysaccharide, as suggested in by Shukla *et al.*[71]. Despite the absence of inter-ring non-bonding interactions, the monomer model was deemed sufficient for initial investigations into the chemistry of NC. Further studies aimed to probe the chemistry at individual nitrate sites on the ring by analysis of reaction energies and transition states. Medium-to-long range interactions present less significance during these initial mechanistic investigations at localised sites. By contrast, the additional time required for exploration of more intricate PES would be significant for the larger models.

The exclusion of secondary non-bonding interactions and reduction in the degrees of freedom due to truncation of the model size simplifies and speeds-up structure searches and identification of the minimum energy path (MEP) from reactants to products. Thus the monomer model will be used for further studies involving single-site reaction mechanisms and transition state searching.

A limitation to the work done in this section is that all calculations were performed in the gas phase. This is relevant to most NC ageing reactions taking place in the dry bulk or in product formulations where the material has not been placed in wetted storage. However for the reactions that must occur in solvent, such as hydrolysis, the structures explored here do not include solvation effects. The most common wetted storage solvents used for NC are water or water-alcohol mixes [82]. Interactions with water in particular will strongly affect the character of intramolecular non-bonding interactions and the geometry around hydroxyl groups due to the polarity of the medium, and availability of hydrogen bonding moieties. However, solvent interactions are not expected to significantly change the chemistry of the nitrate site between the monomer and trimer systems. These effects will partially be taken into account in later chapters with the inclusion of an implicit solvent. A possible extension to the work here would be the repeat of the investigation with both implicit and explicit solvent in order to determine the magnitude of the changes, with particular attention paid to alternative orientation of side chains and capping groups.

Chapter 3

Mechanisms of denitration under ambient conditions

3.1 Introduction

3.1.1 Thermolytic reactions

The first stage of thermolytic decomposition for nitrate esters is generally agreed to be homolytic fission of the O-N bond linking the nitrate to the alkyl chain, leading to the loss of $\cdot NO_2$ (equation 3.1) [83, 84, 85]. Though nitrate homolysis is an endothermic reaction, the weak O-N bond has a typical dissociation enthalpy of 42 kcal mol^{-1} and is easily cleaved when exposed to elevated temperatures, UV light or impact [86]. Whilst the thermolytic degradation of energetic materials has been widely studied experimentally, the ambient, slow ageing mechanisms are less well documented. Low-temperature decomposition routes are influenced by many factors over a protracted lifetime, and in practical use, materials are usually subject to evolving environmental conditions. External changes in pressure, humidity, stress and temperature cycling introduce variation in the degradation patterns of energetic materials. The presence of moisture has been observed to lower the activation energy and accelerate decomposition [84]. Internal factors including impurities, residual solvent, and crystal growth within the bulk, also alter decomposition behaviour.

$$R-ONO_2 \longrightarrow R-O\cdot + \cdot NO_2 \tag{3.1}$$

$$RH-ONO_2 \longrightarrow R=O + HNO_2 \tag{3.2}$$
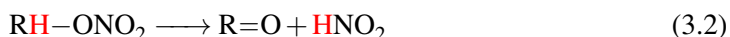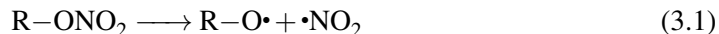
The degradation of nitrate esters at temperatures over 100°C is primarily *via* thermolytic processes, whilst under 100°C, decomposition is largely thought to be the result of hydrolysis [88]. Tsyshevsky *et al.* studied the intramolecular reactions leading to deni-

1. $\cdot NO_2$ loss

2. HNO_2 loss

3. OONO rearrangement

4. γ-attack

5. $ONO_2 \cdot$loss

6. C$-$C cleavage ($CH_2O + NO_2$)

7. C$-$C cleavage ($CO + HNO_2$)
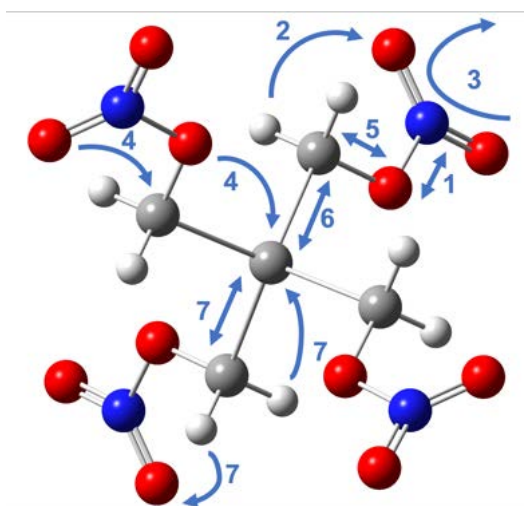
● oxygen   ● nitrogen   ● carbon   ○ hydrogen

Figure 3.1: Intramolecular thermolytic reactions in pentaerythritol tetranitrate (PETN), adapted from the work of Tsyshevsky *et al.* with permission from the publisher [87].
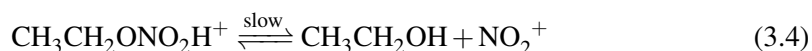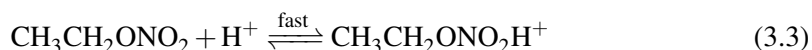
tration in pentaerythritol tetranitrate (PETN) in both the vacuum and the bulk crystal [87] (figure 3.1). Seven mechanisms for the removal of NO_2 were explored. Corresponding to the labels in figure 3.1: (1) homolytic cleavage of the O$-NO_2$ bond, (2) the elimination of nitrous acid (HNO_2) which is usually considered a competing reaction to homolytic fission, (3) the nitro-peroxynitrite rearrangement (O$-$ONO), (4) γ-attack of the terminating nitrate oxygen atom and the bridging nitrate oxygen at their relative γ-carbon sites, (5) the homolytic C$-$O bond cleavage, (6) and (7) two variations of the homolytic C$-$C bond cleavage. It was found that the two most significant decomposition reactions were homolysis of the nitrate ester O$-NO_2$ bond (equation 3.1) and intramolecular elimination of HNO_2 (equation 3.2). Whilst elimination of HNO_2 was found to be the most energetically favourable denitration pathway, homolytic fission dominated preliminary decomposition steps due to the lower activation barrier and faster rate of reaction. It was suggested that global decomposition processes were determined by the interplay between these two mechanisms. Initial homolysis facilitated wide-spread denitration, complemented by exothermic HNO_2 elimination, promoting self-heating of the system and further bond dissociations. The presence of $\cdot NO_2$ and HNO_2 have previously been linked to the autocatalytic rates observed for later-stage decomposition of nitrate esters [89, 90, 91], though some studies solely attribute it to the presence of acids [59, 92, 93, 94]. Other studies also implicate the

action of •NO and HNO$_3$, in addition to •NO$_2$ and HNO$_2$ [95, 96]. Inspection of these products generated from initial processes, with observation of the species permeating through to later stages, will shed light on the most likely contributors to autocatalysis.

3.1.2 Acid hydrolysis reactions

Spent acids remain in the NC matrix following synthesis, even with thorough washing procedures. Additional acidic species are released via the subsequent reactions of •NO$_2$ following homolysis. These acids proceed to react with other moieties in the system, such as unsubstituted alcohol side chains on the polysaccharide, or small molecules free in the bulk.

When exploring the interaction of nitroglycol and nitroglycerin in acid solution, Camera *et al.* [97] proposed a protonation-denitration scheme (scheme 3.1) whereby initial protonation at the nitrate was rapid (equation 3.3), but the subsequent release of the nitronium ion was slow and rate determining (equation 3.4).

$$CH_3CH_2ONO_2 + H^+ \xrightleftharpoons{\text{fast}} CH_3CH_2ONO_2H^+ \tag{3.3}$$

$$CH_3CH_2ONO_2H^+ \xrightleftharpoons{\text{slow}} CH_3CH_2OH + NO_2{}^+ \tag{3.4}$$

Scheme 3.1: The relative rate of stepwise protonation and denitration of nitrate esters, using ethyl nitrate as an example. From the work of Camera *et al.* [97].

NC in storage is kept wetted with solvents to prevent self-ignition [99, 100]. Material with 12.6%N or lower must be stored in 25% water by mass, or in a controlled mixture of solvents, stabilisers and plasticisers. The material is therefore always exposed to water, with the fast-exchange of protons expected at inter-facial surfaces. In the study of organonitrates and organosulfates generated from isoprene in the aerosol phase, Hu *et al.* found that primary and secondary nitrates were resilient to hydrolysis for pH > 0, whilst tertiary nitrates underwent hydrolytic nucleophilic substitution easily, reacting with water to form alcohols [98]. In tertiary nitrates, the carbon is fully substituted with no attached hydrogens. This group is usually sterically hindered and stabilising to carbocations, condition on the
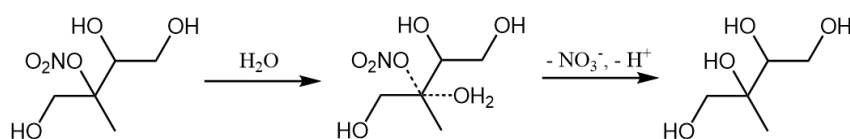
Scheme 3.2: Hydrolysis of a tertiary nitrate derived from the reaction of isoprene in the aerosol phase, from the work of Hu *et al.* [98].

electron donation ability of the substituents remaining after nitrate removal. If formation of a carbocation intermediate is involved in the hydrolysis mechanism, this may explain why the tertiary nitrates exhibited highly efficient denitration, even under neutral conditions.

Though no specific mechanistic detail is given, the action of a protonated transition state during hydrolysis is alluded to through the contrast between the rate of acid-catalysed and neutral hydrolysis reactions. Neutral hydrolysis of the tertiary nitrates occured rapidly, but hydrolysis only occurred for primary and secondary nitrates under strongly acid catalysing conditions, and at a much slower rate. Additionally, the presence of adjacent OH groups hampered the rate of hydrolysis for some aerosol dispersed organonitrates. In the neutral hydrolysis of tertiary nitrates, increasing the number of adjacent OH groups lead to protracted hydrolysis lifetimes. Interestingly, the retardation effect of adjacent OH groups was not observed for the the acid catalysed cases. Hu proposed that this could be due to the interaction of OH with the transition state of the neutral hydrolysis system, compared to the protonated transition state of the acid catalysed system, impeding the reaction only in the former case. The cause of this effect is unclear, and without understanding of the mechanisms involved, it is difficult to explain.

There is evidence that nitration and denitration of nitrate esters is also influenced by the presence of nitrate groups at neighbouring positions. Matveev *et al.* demonstrated that for poly-nitroesters the rate of liquid-phase decomposition did not increase linearly with number of nitrate reaction centres. It was found to mainly dependend on individual structures (table 4.1) [101]. The trend in reactivity could be partially explained by the inductive effect of the nitro groups [83]. The inductive effect arises when a difference in the electronegativity between atoms connected by a σ bond leads to a polarisation, or permanent dipole, in the bond. Electron donating groups increase the δ^- partial charge on neighbouring atoms through the release of electrons, whilst electron withdrawing groups pull electron density away, generating a δ^+ charge on connected atoms. The NO_3 presents a stronger electron withdrawing effect than OH, which is a donating group. The presence of an adjacent nitrate appears to facilitate denitration, whereas the presence of hydroxyl groups hinders this process, for neutral hydrolytic schemes. The resonance effect, arising from π donation by lone pairs on oxygen and nitrogen is negligible between substituents at different sites on the polysaccharide ring, as the ring is saturated.

The investigation by Hu *et al.* exclusively focused on nitrates generated from an iso-

Table 3.1: Comparison of rate constants of decomposition for various polynitrate esters at 140°C. ΔT is the decomposition temperature range, E is the experimental activation barrier for decomposition, log$A$ is the pre-exponential factor, T_c is the combustion temperature, k_{expt} is the rate constant for decomposition. Collated by Matveev *et al.*[101] from the work of Afanas'ev *et al.* (*) [102] and Lur'e *et al.*(**) [103].

Compound	ΔT / °C	E / kcal mol^{-1}	log$A$ [s^{-1}]	k_{expt} / 10^{-6}s^{-1}
$O_2NOCH_2CH_2CH_2ONO_2$*	72–140	39.1	14.9	1.7
$O_2NOCH_2CH_2CH_2CH_2ONO_2$*	100–140	39.0	14.7	1.1
$O_2NOCH(CH_3)CH(CH_3)ONO_2$*	72–140	40.3	14.9	5.0
$O_2NOCH_2CH_2OCH_2CH_2ONO_2$**	80–140	42.0	16.5	1.9
$O_2NOCH_2CH(OH)(CH_2ONO_2)$*	80–140	42.4	16.8	2.3
$O_2NOCH_2CH(ONO_2)(CH_3)$*	72–140	40.3	15.8	3.0
$[(O_2NOCH_2)CH(ONO_2)CH(ONO_2)]_2$ (hexanitromannite)**	80–140	38.0	15.9	63.0

prene precursor, upon dispersion as an aerosol. The nitrate groups present in NC are either of primary (C6) or secondary (C2, C3) structure, indicating that ambient hydrolysis is unlikely according to this scheme. However, solvent effects are expected to differ for condensed-phase reactions and aerosol phases. A greater build-up of acid concentration can be achieved in a closed, condensed system, and the lifetime of an aerosol is relatively short-lived when considering the timescale of slow ageing processes in NC. Thus, the work of Hu *et al.* does not provide a direct comparison for the NC polymer but highlights the possible contribution from both neutral and acid-catalysed hydrolysis routes, and effect of increasing levels of substitution on the wider structure.

In this section, the possible mechanisms for nitrate removal from the NC backbone are explored. The homolytic fission and HNO_2 elimination thermolytic processes suggested by Tsyshevsky will be compared to the acid hydrolysis scheme. Though the relative rates of reaction are not compared, the extended timescales involved in ambient ageing imply that the dominating reactions correspond to those most thermodynamically favourable.

3.2 Methodology

The energies of homolytic fission (equation 3.1) and elimination of HNO_2 (equation 3.2) were calculated for PETN, as a test system before extension to the NC monomer. The free energies of reaction (ΔG) were calculated according to equations 3.5 and 3.6 to reproduce

the work of Tsyshevsky *et al.*, using the published geometries of PETN and its derivatives obtained from the authors (R. Tsyshevsky, personal communication, 19 April 2017).

$$\Delta G_{Homolysis} = (G_{RO\bullet} + G_{\bullet NO_2}) - G_{RONO_2} \qquad (3.5)$$

$$\Delta G_{HNO_2 elim.} = (G_{R=O} + G_{HNO_2}) - G_{RONO_2} \qquad (3.6)$$

R = pentaerythritol trinitrate (PETRIN), NC monomer

In the case of the homolysis reaction, only the denitrated radical product geometry was provided. The product of HNO_2 elimination was given as a complex of the HNO_2 leaving group and the newly formed aldehyde. A single point energy and frequency calculation were performed on each of the species to determine the reaction energies; no geometry optimisation was performed on the given structures except for in the case the $\bullet NO_2$ molecule, where the geometry was not supplied. A separate $\bullet NO_2$ molecule was independently geometry optimised.

The intramolecular reactions of the NC monomer were modelled according to scheme 3.3. Rigid and relaxed PES scans were attempted for both reactions for the NC monomer to obtain an energy profile, and in the case of HNO_2 elimination, identify a transition state. The homolysis reaction was treated as barrierless. Where the scans were unable to identify a valid transition state geometry, guess transition state geometries were constructed and optimised.
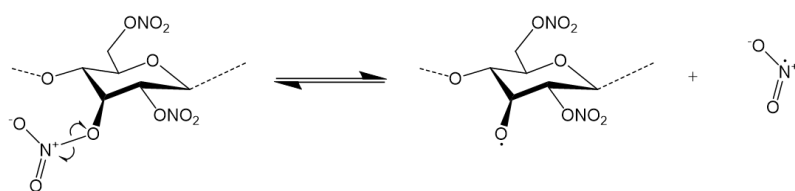
**(a)** Removal of a nitrate group *via* homolytic fission of NC
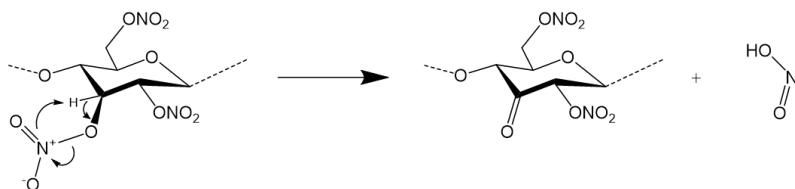
(b) Removal of a nitrate group *via* elimination of HNO_2.

Scheme 3.3: The proposed intramolecular reactions for the initial denitration step during NC degradation.

The possible protonation sites for the NC monomer were explored by placing a proton

at each of the different oxygen sites surrounding the nitrate group. The structures were then geometry optimised and energies of protonation were compared. H_3O^+ was modelled as the donating species; as NC is usually stored wetted in water, the hydronium ion is the most likely source of protons (equation 4.11).

$$RONO_2 + H_3O^+ \longrightarrow RONO_2H^+ + H_2O \tag{3.7}$$
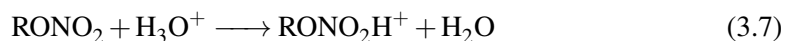
It is also possible that the proton is donated by other acidic species in the system, particularly HNO_2 or HNO_3. This is more likely at later stages of degradation when a higher concentration of acid has been generated by secondary reactions. For investigations into the hydrolytic methods of nitrate removal following protonation, or a concerted mechanism involving a proton donor, an ethyl nitrate molecule was used as a truncation of the monomer. This facilitated a speedup of initial PES scanning by reducing the degrees of freedom, whilst presenting the moieties necessary for preliminary TS searches for the hydrolytic scheme. This was with the intention of later using the found TS geometries to inform guesses for the NC monomer structure.

3.2.1 Computational details

All geometry optimisations, thermochemistry calculations and PES scans were performed in G09. Geometry optimisation and thermal calculations were to the level of 6-31+G(2df,p) using ωB97X-D and B3LYP, with default convergence criteria (max. force 4.5×10^{-4} H/Bohr, RMS force 3×10^{-4} H/Bohr, max. displacement 1.8×10^{-4} H/Bohr and RMS displacement 1.2×10^{-4} H/Bohr). ΔG values were obtained by the difference between the thermally corrected free energies of products and reactants. Zero-point corrected energies were determined by addition of individual zero point energies to the free energy:

$$\Delta G^{ZPE} = \sum (G_{products} + ZPE_{products}) - \sum (G_{reactants} + ZPE_{reactants}) \tag{3.8}$$

Whereby the zero-point energy (ZPE) was obtained from the QM frequency calculation by evaluation of the energy of the lowest vibrational level over all molecular vibrations:

$$E_{ZPE} = E + \sum_{i}^{modes} \frac{1}{2} h\omega_i \tag{3.9}$$

Where E is the energy of the molecule at the minimum (for geometry optimisations) or maximum (for transition state optimisations), *modes* refers to the vibrational modes, h is Planck's constant and ω is the vibrational frequency. For reaction energy calculations, the ZPE energies were scaled by the empirically derived factor of 0.9756 for ωB97X-D/6-31G(2df,p) [104]. This was to correct for deviation arising from an incomplete description of electron correlation and neglect of anharmonicity during the calculation of vibrational frequencies [105, 2].

PES scans were performed to ωB97X-D/6-31+G(d) or unrestricted ωB97X-D, in the case of $O-NO_2$ dissociation. As high accuracy energy values for structures generated during PES scans were not required, calculations were performed at a lower level to conserve time and computational effort. Rigid scans were carried out by fixing bond lengths, angles and dihedral values as constants. Only the variable of interest was allowed to change. This was with the exception of relaxation of other specified coordinates required for accommodation of the new geometry, following each step of the scan. For example in the homolysis of the $O-NO_2$ bond, as the NO_2 group departed the internal O–N–O angle was also allowed to relax, in addition to the angle of the departing NO_2 relative to the remainder of the molecule. In two-dimensional scans, two variables were scanned simultaneously. For the same reaction, the elongation of a the $O-NO_2$ bond was scanned with simultaneous approach of a proton, to monitor the effect of protonation for the same reaction. Relaxed scans were performed in Gaussian using the "modredundant" function, whereby the whole structure was geometry optimised after each step of the scan. Scans were performed with step size of 0.1 Å. The number of steps varied with the property investigated, though the majority of the phenomena were observed within 20 steps (2 Å). Scans were attempted in vacuum, and for the protonation cases, implicit solvent using PCM with water (ε=78.4) [48].

3.3   Results and discussion

3.3.1   Thermolytic decomposition mechanisms

The energies of homolytic fission and intramolecular elimination of HNO_2 from a PETN nitrate group are shown in table 3.2. The energy values published by Tsyshevsky *et al.* are denoted in parenthesis. As the reaction proceeds with no barrier, the ΔG_r and E_a values are the same in the case of homolytic fission.

PETN reactant, TS and product geometries were supplied by the authors (R. Tsy-

shevsky, personal communication, 19 April 2017) except in the case of the •NO$_2$ homolysis product, which was not provided. The •NO$_2$ leaving group used in the homolysis reaction calculation was independently geometry optimised, with its energy contributing additively to the products of the reaction. The PETN−HNO$_2$ TS and product was provided as a complex. The same method and basis (ωB97X-D/ 6-31+G(2df,p)) were used in order to recreate the published reaction energies, however, the calculated values fall below the literature values by 0.3 - 1.2 kcal mol^{-1}. A possible explanation may be that the geometries provided do not exactly match those used in the study, particularly in the case of •NO$_2$. A contribution may also arise from variation in calculation setup and the use of a different version and compilation of the G09 program, leading to fluctuations in the exact values obtained. These differences would be amplified when combining individual energies for the calculation of reaction energy values. Cumulatively these changes may explain the discrepancy between the observed values and those in the publsihed study. Nevertheless, the calculated value for the activation energy of homolytic fission of PETN is comparable to the experimentally derived values of 45.9±1.2 - 47.3±0.3 kcal mol^{-1} [106, 107, 108], and ΔH_r falls within the experimental bounds ofnitrate homolysis in alkanes (35.6±0.3 - 42±0.3 kcal mol^{-1}) [109].

The homolytic fission reaction was applied to a NC monomer singly nitrated at C2

Table 3.2: Calculated free energies of reaction at 298.15 K (ΔG_r), reaction enthalpies (ΔH_r), activation barriers (E_a) with zero-point correction (ZPE) for the intramolecular reactions of PETN, and the NC monomer calculated at ωB97X-D/ 6-31+G(2df,p). Values expressed in kcal mol^{-1}.

Reaction	ΔG_r	ΔG_r^{ZPE}	ΔH_r	ΔH_r^{ZPE}	E_a	E_a^{ZPE}
PETN						
•NO$_2$ loss	26.4	21.4	40.4	35.5 $(35.8)^a$	40.4^b (41.2)	35.5 (35.8)
HNO$_2$ loss	−23.5	−21.0	−20.3	-17.7 (-18.6)	46.5 (47.3)	41.5 (42.7)
NC monomer						
•NO$_2$ loss	27.7	23.1	40.7	36.1	40.7	36.1
HNO$_2$ loss	−32.4	−35.8	−19.3	-22.7	43.5	39.5

[a] values from the work of Tsyshevsky *et al.* [87].
[b] values for the activation energy and total energy of reaction are the same for bond dissociation via homolytic fission.
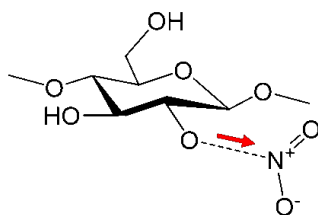
Figure 3.2: The $O-NO_2$ bond was elongated during rigid and relaxed PES scan to simulate homolytic fission for the NC monomer.

(figure 3.2). The $O-NO_2$ bond was incrementally stretched using geometry scanning, to obtain an energy profile of the reaction. For the rigid scan (figure 3.3), only the internal angle of the departing NO_2 and coordinates referencing its orientation relative to the rest of the molecule were allowed to relax. As the scan progressed, the NO_2 internal angle increased from 129.2° to 134.6°, at maximum separation of 5 Å from the bridging oxygen (Ox). This corresponds to the literature value for the $O-N-O$ internal angle (134.3°) confirming the formation of a $\cdot NO_2$ radical.
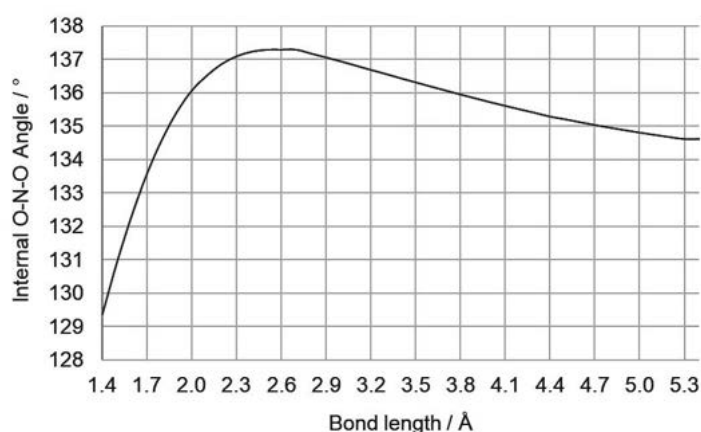

Figure 3.3: The change in the $O-N-O$ internal angle as the NO_2 group is pulled away from the NC monomer during a rigid geometry scan of homolytic fission.

In the case of the NC monomer, both rigid and relaxed scans failed to capture the TS for cleavage of the nitrate group via interaction with the α-hydrogen. A guess transition state was constructed based on the TS of the analogous reaction for PETN (figure 3.4b), and optimised to produce the structure of the correct imaginary vibration. The pattern for the NC monomer resembles that found for PETN; homolysis is endothermic but with lower activation barrier, whilst HNO_2 elimination is exothermic, with a much higher barrier. It is anticipated therefore, that the rate of homolytic fission will be faster, whilst HNO_2 loss will happen more slowly, whilst contributing to system heating and increasing acid concentra-
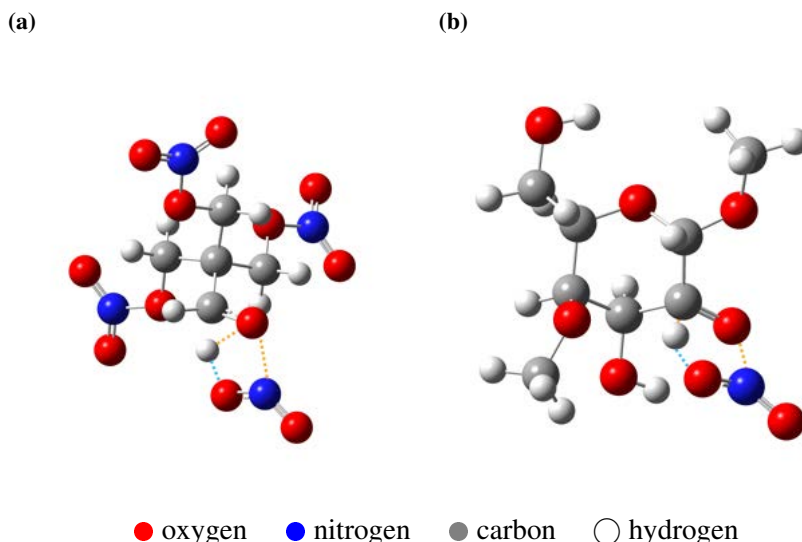
tion.

(a) **(b)**

● oxygen   ● nitrogen   ● carbon   ○ hydrogen

Figure 3.4: TS for the elimination of HNO_2 by removal of the α-hydrogen by the NO_2 leaving group in a) PETN and b) NC. Orange dashed lines indicate bonds breaking and blue dashed lines indicate bonds forming.

3.3.2 Acid hydrolysis mechanism

3.3.2.1 Protonation site

In polar, protic solvents such as water, the fast-exchange of protons between the aqueous medium and the monomer is expected. Computational studies by Jebber *et al.* and Liu *et al.* probed the protonation behaviour of β-glucose [110, 111]. Key findings demonstrated that the most favoured protonation site in glucose was greatly influenced by the conformation of the C6 side branch. For the C6 hydroxymethyl chain orientated in the gauche position, protonation of the ring-oxygen produced the most stable structure.

The protonated NC monomers explored in this section are shown in figure 3.5. The bridging oxygen (Ox), the C1 capping group oxygen, and the terminal nitrate oxygen sites (Ot) were protonated and their relative energies compared in order to determine the site most likely to stabilise the proton at thermal equilibrium. Protonation also occurs on other sites in the molecule, such as at unsubstituted hydroxyl oxygen sites, the capping group oxygen on C4 and O1 in the glucose ring. Whilst it is possible that protonation at these further sites in the monomer would contribute to degradation, these processes would occur *via* alternative mechanisms without the involvement of denitration. For the purposes of studying acid hydrolysis, only the sites peripheral to the nitrate leaving group were explored.

The energies for the optimised protonated monomer conformers are listed in table
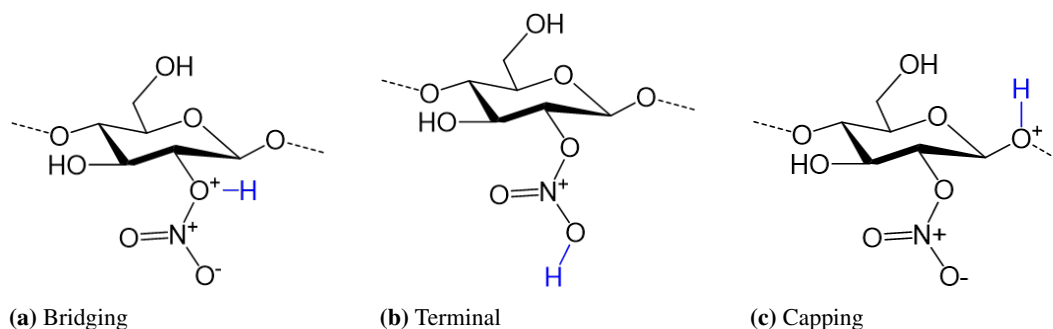
(a) Bridging   **(b)** Terminal   **(c)** Capping

Figure 3.5: Protonation sites on the NC monomer for hydrolysis of the nitrate at the C2 position.

Table 3.3: Free energies of protonation, for each of the oxygen sites of interest on the CH_3/CH_3 monomer of NC, nitrated at the C2 site.

Protonation site	ΔG_r /kcal mol^{-1}			
	ωB97X-D	PCM (water)	B3LYP	PCM (water))
Bridging	-26.9	2.8	-29.8	2.7
Terminal (syn)	-30.1	12.8	-31.8	11.4
Terminal (anti)	-20.6	10.7	-22.8	9.2
Capping	-30.1	0.9	-31.8	-1.1

4.1. There is good agreement between ωB97X-D and B3LYP values in the vacuum, with B3LYP predicting a slightly lower reaction energy in all cases. This is likely due to the known underestimation of reaction energies by B3LYP, particularly in systems involving multiple C-C bonds [112] and with weak, non-covalent interactions [113, 114]. These issues are treated in ωB97X-D with the inclusion of medium and long term dispersion, and has been shown to improve the accuracy of modelled C-C bond lengths [115], in particular outperforming B3LYP in calculations involving hydrogen bonding networks [116]. The large difference in the reaction energies between the gaseous and implicit solvent values are explained by the instability of H_3O^+ in vacuum, where it prefers to lose the proton and exist as water. Ionic species exhibit much greater reactivity in the gaseous phase compared with their neutral counterparts [117, 118, 119]. When in solution, the positive charge is solvent stabilised; the proton is less readily released.

In the gaseous phase, the most thermodynamically favoured protonation sites are at the terminal (syn) and capping positions. Inspection of the optimised geometries explains the similarity of their ΔG_r values. The protonated terminal (syn) and capping monomers (figures 3.6c) and 3.6e)) present nearly identical geometries in vacuum. In the terminal (syn) case, the proton has moved towards the capping group oxygen, effectively undergoing
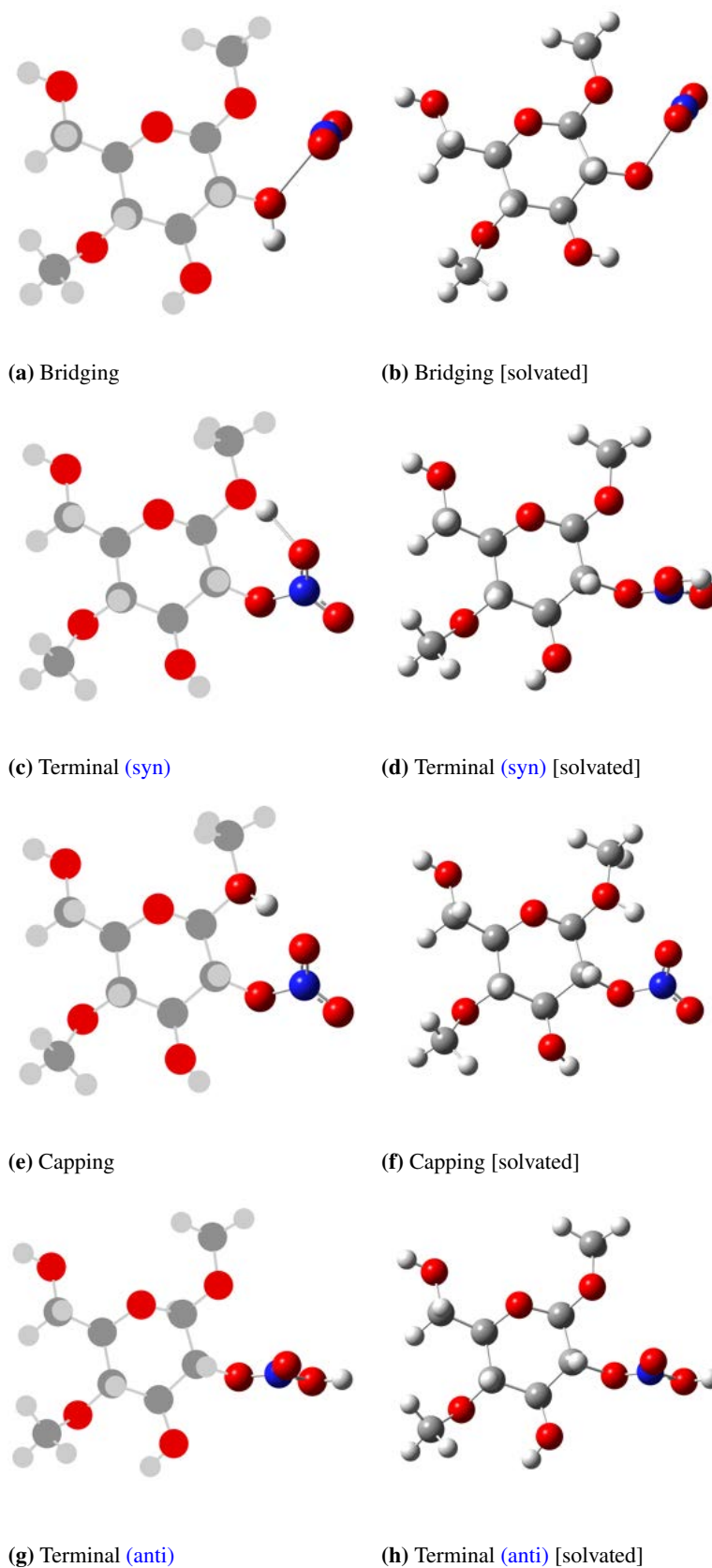
(a) Bridging   (b) Bridging [solvated]

(c) Terminal (syn)   (d) Terminal (syn) [solvated]

(e) Capping   (f) Capping [solvated]

(g) Terminal (anti)   (h) Terminal (anti) [solvated]

Figure 3.6: Protonated NC monomer structures after geometry optimisation to the level of ωB97X-D/6-31+G(2df,p). *Left column:* In vacuum. *Right column:* In implicit solvent (PCM = water). The interacting parts of the molecule are highlighted in 3D in the structures on the left (optimised in gas phase.)

a proton transfer and generating the same structure as the protonated capping monomer. This is in contrast to the solvent phase (figure 3.6d)), where the protonated nitrate group is rotated perpendicularly to the ring and the proton remains on the terminal oxygen; the solvent presents stabilisation for the protonated Ot. This indicates that the terminal (syn) site is is only likely to remain protonated in solvent, and that protonation at the site in vacuum is highly unstable. The remainder of the monomers exhibit only minor changes in geometry between vacuum and solvent. Under solvent conditions, the most stable site for protonation is the capping group (which is unlikely to lead to denitration), followed by the bridging oxygen.
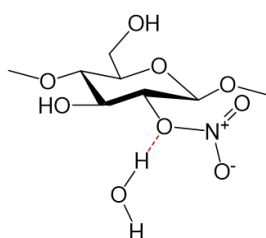

Figure 3.7: The attempted coordination geometry of a single water molecule to a NC monomer.

Water as the protonating species was also attempted (figure 3.7), by optimisation of one, two and three water molecules in coordination with the nitrate site in the NC monomer. The same was repeated with the hydronium ion to probe likely coordination geometries. However in both cases, no stable complexes could be isolated. It is anticipated that a much larger network of waters around both the regions surrounding the nitrate moiety and the wider molecule, are required to achieve a stable water coordination structure. This would be of interest for further investigation into the mechanism of neutral hydrolysis involving the autoionsation of water [120]. Evaluation of the energy of protonation at each site found that the bridging and capping oxygens were the most likely sites; with only the bridging isomer likely to contribute to denitration. However, protonation at the terminal structures will also be explored as the starting point for the subsequent denitration stage.

3.3.2.2   Denitration by hydrolysis

Following the protonation step, possible transition states for the removal of the nitrate were investigated. Direct dissociation of NO_2 from the protonated species was explored (figure 3.8a)), along with the simultaneous approach of a proton and cleavage of the NO_2(figure 3.8b)). The scan of the proton moving towards the bridging site was also conducted, to

determine whether any elongation of the O−NO$_2$ occurred as a result of the formation of the proton-oxygen bond (figure 3.8c)).
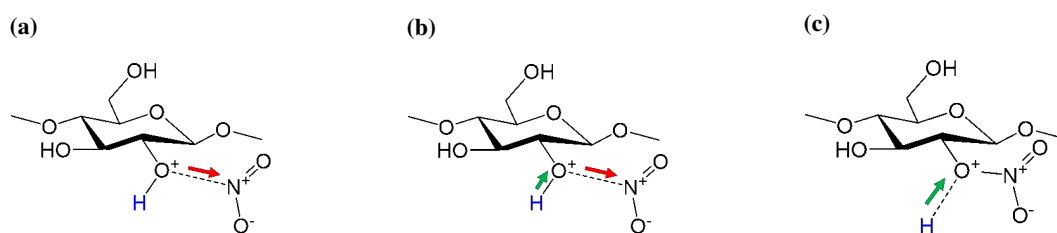

Figure 3.8: The scanned coordinates of a) dissociation of NO$_2$, b) concerted protonation and NO$_2$ dissociation and c) proton approach. Green arrows indicate bond formation, red arrows indicate dissociation.

The relaxed PES scan of NO$_2$ removal from ethyl nitrate protonated at the bridging site was used as a preliminary test for the mechanism of denitration, following protonation (figure 3.9). Unrestricted ωB97X-D was used in case of the formation of •NO$_2$ instead of the expected NO$_2^+$, with 20 steps of 0.1 Å. However, bond dissociation was not illustrated in the energy profile even when extending the scan distance to a maximum of 6.4 Å. Instead, a steady increase in the energy was observed. It was observed that as the nitro group distance increased, its internal angle increased to 180°, confirming the formation of NO$_2^+$. It is anticipated that the departing NO$_2^+$ will further react with water in the system to produce acids conducive to further hydrolysis. As the scan proceeded, the molecule rotated and the NO$_2^+$ leaving group aligned with the hydroxyl in an orientation suitable for peroxy group formation (figure 3.9d). This mechanism was previously considered in the degradation reactions of PETN; it was found that the energy of this process was higher than that of HNO$_2$ elimination, where the nitrate was not initially protonated. The formation of the peroxy bond was not facilitated by the scan parameters due to forced increase of the O−N distance. The same process was not observed when the scan was applied to the NC monomer. As the formation of the peroxy geometry required re-orientation of the whole molecule, the energy of this rearrangement was not favourable for the bulky NC unit. In the real polymeric system, it may induce distortion of the sugar ring, proving even more energetically demanding.

Proposed 4-membered ring and 6-membered ring TS were also investigated in order to determine whether they formed energetically and geometrically reasonable structures facilitating nitrate removal, with reformation of the alcohol group on the sugar ring (figure

3.10). Optimisations were attempted with both full geometry relaxation, and various frozen coordinate schemes for each proposed TS. R groups were truncated even further to methyl nitrate ($R = CH_3$), in effort to limit degrees of freedom during optimisation of the TS structures. Despite this, no structures were able to achieve convergence *via* full relaxation. Freezing the bulk of the molecule with relaxation only around the nitrate group and its' coordinating species, followed by relaxation of the wider molecule with fixed coordinates around the nitrate allowed sequential optimisation of different moieties, increasing chances of global energy minimisation. It was possible to optimise the 4-membered ring bridging TS on the NC monomer with frozen TS ring geometry *via* preliminary optimisation of the ring structure with methyl nitrate. The optimised ring geometry was then placed on the monomer, with fixing of thee coordinates, allowing the remainder of the molecule to relax. A rigid scan was then performed of the 4-membered ring transition state, starting from the bridging site protonated monomer (figure 3.10(d)). It was revealed that as the nitrate moved away from the system, the proton moved to the capping group site rather than remain on the bridging oxygen as a hydroxyl, as was initially expected. Instead, a ketone group was formed between the bridging oxygen and the ring. At subsequent steps, the ketone group caused the C2 - C3 bond to elongate and break. The scan eventually showed the NO_2 leaving group reclaiming the proton from the capping group oxygen, leading to ring fission. The activation and kinetic barrier involved in ring fission ($\delta G = 56.9$ kcal mol^{-1}) is much higher than that of denitration ($\delta G = 10.1$ - 24.8 kcal mol^{-1}) [121]; a study on the acid hydrolysis
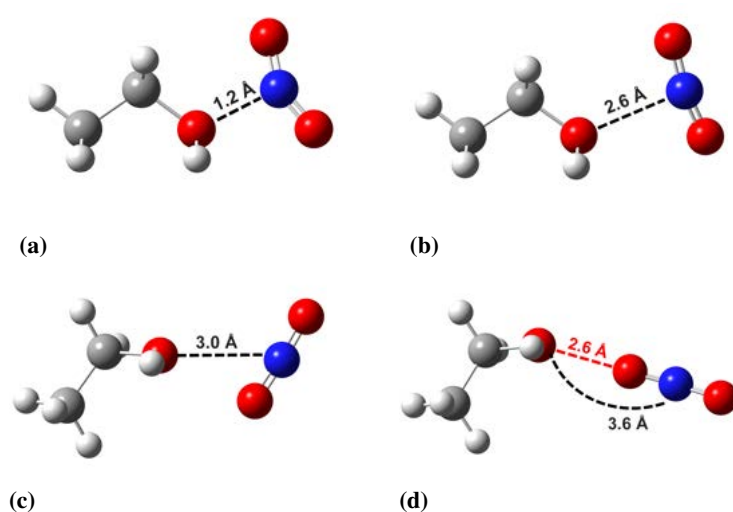

Figure 3.9: Geometries from steps 1, 7, 11 and 26 of the geometry scan of Ox protonated ethyl nitrate (EN) denitration.
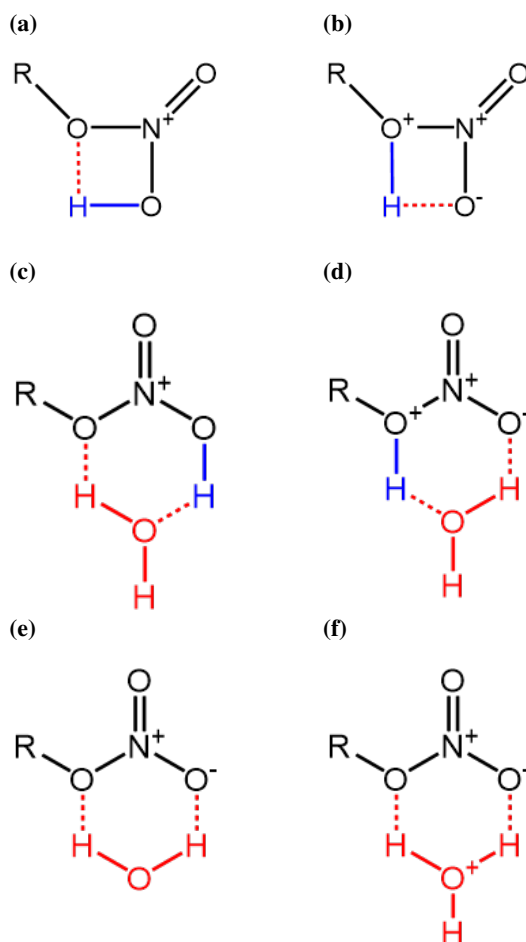
Figure 3.10: Proposed 4-member and 6-member ring transition states for the denitration of a nitrate ester, under various hydrolytic conditions. R = CH_3 in the case of methyl nitrate, R = CH_2CH_3 in the case of ethyl nitrate and R = $(H_3CO)_2C_6H_9O_3$ for the monomer.

of glucose and xylose demonstrated that ring-opening intermediates were either extremely short lived, or not observed at all [122]. The open-chain product of the scan is likely due to the geometric constraints placed on the geometry of the departing NO_2 group, rather than a likely physical process. However, it sheds light on the scheme by which ring fission may occur under conditions of elevated temperature or pressure, which has been implied in previous work involving the formation of a ketone at earlier stages of the reaction.

Attempts to isolate the other TS structures were unsuccessful, even when simplifying the side chain to methyl nitrate and under implicit solvent conditions.

3.4 Summary

In this section, three different denitration reactions were explored as the first stage in ambient decomposition of NC. The reactions were firstly tested on PETN, where prior studies by
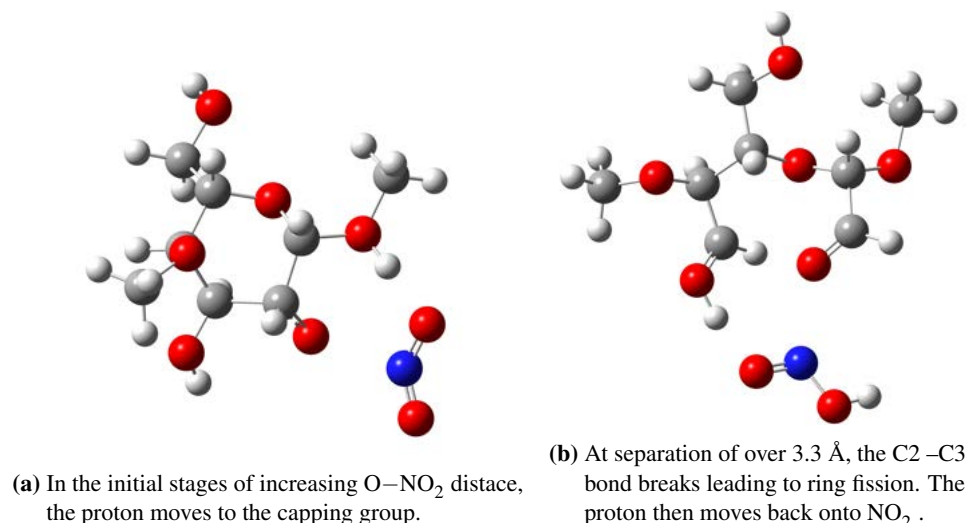
(a) In the initial stages of increasing $O-NO_2$ distance, the proton moves to the capping group.

(b) At separation of over 3.3 Å, the C2 –C3 bond breaks leading to ring fission. The proton then moves back onto NO_2 .

Figure 3.11: Relaxed scan of NO_2 departure, starting with the 4-membered ring structure.

Tsyshevsky *et al.* had confirmed homolytic fission and elimination of HNO_2 reactions to be the dominant mechanisms in thermolytic ambient ageing [87]. A singly nitrated monomer was used with methoxy capping groups, to simulate a unit in the NC polymer chain.

Thermolytic cleavage of the nitrate group was modelled *via* homolysis and elimination of HNO_2. In the case of PETN it was found that the reaction energies closely matched those in the published study and in the case of homolysis, fell within range of experimental measurements for enthalpy of reaction and activation energy. The same process was repeated for the NC monomer, singly nitrated at the C2 site. The energy of homolytic fission was in good agreement with the expected value based on the outcome of the PETN product. PES scans of homolysis confirmed the loss of $\cdot NO_2$ for the NC monomer.

The elimination of HNO_2 *via* intramolecular α-H transfer was compared with homolysis. The calculated energies of reaction and activation energy values gave good agreement with the published values in the case of PETN [87]. Calculated NC values were also within the anticipated range, based on the reaction for PETN. PES scans were unable to locate a TS for the NC monomer, however, a successful guess geometry was generated based on the analogous TS structure in the reaction for PETN. Enthalpies of reaction showed that this process was more exothermic in the case of NC than for PETN, and that the elimination of HNO_2 was more thermodynamically favourable in NC compared to homolysis. However, homolysis may occur more rapidly, as is the case for PETN.

The protonation sites on the NC monomer were probed for the most favourable position. It was found that in the gas phase, capping and bridging site protonation lead to the

same protonated final structure. In the solvent phase, the capping site was energetically preferred seconded by the bridging site. Protonation at the capping group site and subsequent reaction would more likely lead to chain scission; this avenue was disregarded in further studies focussing on the acid hydrolysis pathway, in favour of protonation at the bridging oxygen site where the geometry allowed for easy nitrate removal.

Optimisation of water - monomer and hydronium - monomer complexes were attempted, in order to obtain information on the nature and orientation of the protonation complex. It was not possible to isolate any stable structures, implying that a larger stabilising network of waters is likely required.

Dissociation of NO_2 from the protonated analogues of ethyl nitrate and the NC monomer were scanned using a variety of rigid and relaxed PES schemes. In the removal of NO_2 from protonated ethyl nitrate, the release of NO_2^+ was indicated by the change of geometry around the nitrate from bent to linear, as the $O-NO_2$ bond elongated. Rotation of the remaining ethanol and complexed NO_2^+ showed orientation suitable for formation of a peroxide. This rotation was not observed in the case of the monomer, however the leaving group still presented as NO_2^+. 4 and 6 membered ring TS were also tested for the denitration reaction. Unexpectedly, it was found that none of the 6-membered ring structures could be isolated, regardless of truncation of the system to a protonated methyl nitrate model, or using the un-protonated monomer to simulate concerted protonation-denitration. In the case of the bridge-protonated NC with formation of the 4-membered ring TS at the C2 nitrate, it was possible to relax the NC monomer structure around the ring so long as the ring geometry itself was frozen. As the leaving group moved further from the remainder of the molecule, the hydroxyl group located at C2 formed a ketone, losing the proton to the departing NO_2^+, to form HNO_2 in later stages of the scan. Eventually ring fission occurred, as the HNO_2 move sufficient distance away, and the formation of the ketone forced the adjacent $C-C$ bond in the ring to stretch, and then break. It is known that the energy required for this process is much higher than that of denitration, so is unlikely to contribute to the initial stages of ambient ageing.

In summary, this section explored the degradation reactions responsible for denitration, the primary step leading to more extensive decomposition. With respect to thermolytic mechanisms, it was found that homolysis and HNO_2 elimination were both feasible initial denitration routes. HNO_2 elimination was more energetically favourable and likely to

dominate in ambient, purely thermodynamic conditions. Investigation into acid hydrolys pathways found that protonation at the NC bridging site was most likely, and whilst a TS could not be obtained for the reaction, it was confirmed that hydrolytic denitration occurred with the release of NO_2^+. This work should be extended with further exploration of water complexation around the NC monomer through the use of explicit solvent.

In the next chapter the reactions of the species generated as a result of the primary denitration steps will be studied to elucidate the formation pathways of the final experimentally observed degradation products.

Chapter 4

Post-Denitration Reactions

4.1 Introduction

Products of the preliminary denitration step of NC can be evolved as gases or remain trapped in the polymer matrix. Reactive nitrogen dioxide radicals generated from homolysis of the O-N bond are likely to migrate within the bulk and attack other sites on the polysaccharide, initiating branched radical chain reactions. These lead to deeper decomposition of the polymer *via* chain scission and rupture of glucose rings, with eventual complete disintegration of the molecule, assisted by products released by ongoing acid hydrolysis. Nitrous and nitric acids are released directly from denitration or via transformation of released NO_x species. In addition to catalysing hydrolysis, they increase the acidity of the overall system, lowering the pH and stimulating further hydrolytic processes [98]. The final product mixture is dictated by the numerous side reactions involving autocatalysis, radical reactions and product interactions.

When studying the ageing of NC using ultraviolet–visible spectroscopy (UV-vis), Moniruzzaman *et al.* observed increasing concentrations of reaction products, beyond those generated from first-stage decomposition, with increasing heat treatment and over longer timescales [123, 88]. The studies used the reaction of nitrates with an anthraquinone dye (SB59) (figure 4.1) to probe the reactivity at each of the C2, C3 and C6 sites of NC, using ^{1}H NMR spectroscopy and UV-vis (figure 4.2). The reaction of SB59 with NO_x released by denitration (figure 4.3) mimics the action of stabilisers such as diphenylamine (DPA) and 2-Nitrodiphenylamine (2-NDPA) commonly used in NC formulations. The secondary amine groups of the dye consume any nitrates in the system, eliminating the possibility of successive reactions generating acidic species. Un-aged NC thin films, and films aged at 40°C, 50°C, 60°C and 70°C for timescales of up to 2000 hrs for 40°C, were compared.
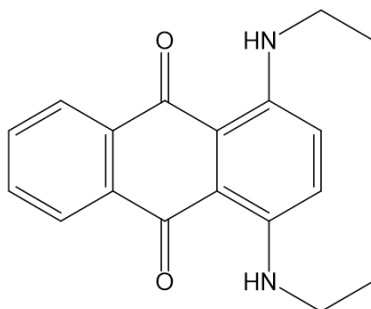
Figure 4.1: 1,4-bis(ethylamino)-9,10-anthraquinone dye (SB59) used to probe the release of nitrates from NC using UV-vis and ^{1}H NMR spectroscopy [88]. The action of nitrate absorption by the dye imitates that of stabilisers commonly used with nitrate ester formulations.

UV absorbances at 600 nm and 650 nm were characteristic of the SB59 dye before reaction with NO_x. The isosbestic point identified at 552 nm showed a proportional relationship between the decrease in concentration of SB59 as it was consumed, with the concentration of the [SB59 + NC] product as it increased.

For samples aged at temperatures >40°C, the isosbestic point demonstrated a downwards shift with increasing dye consumption. The drift from the isosbestic point, in addition to the appearance of new absorbance peaks below 400 nm, allude to the presence of new species in the reaction mixture not generated by the primary reaction of SB59 and NC. It is likely that these arise from the continued reaction of SB59 derivatives with NC degradation products, or further derivatives thereof, as suggested in figure 4.3 III, IV and V. In the case of the 70°C treated run, the final measurement (indicated by the royal-blue line in bold in figure 4.2d)) deviated from the isosbestic point entirely, with more than 81% consumption of the original dye concentration. This suggests that the samples exposed to the higher ageing temperatures presented spectra dominated by products formed *via* secondary reactions.

Following cleavage of the nitrate ester *via* homolytic fission, elimination of HNO_2, or hydrolysis, the resulting residues are available for further reaction with the polymer or other free molecules in the system. In the study of PETN ageing at high temperatures (115°C - 135°C) in vacuum, and low temperatures (20°C - 65°C) in acetonitrile solution, Shepodd *et al.* commented that thermolysis produced a more complex and varied mixture, due to deeper degradation and recombination of radicals [85]. By contrast, the low temperature hydrolytic process emphasised formation of PETRIN was followed by side reactions with reduced likelihood of radical recombination in solution compared to in a solid, as $\cdot NO_2$

(a) NC film aged at 40°C.
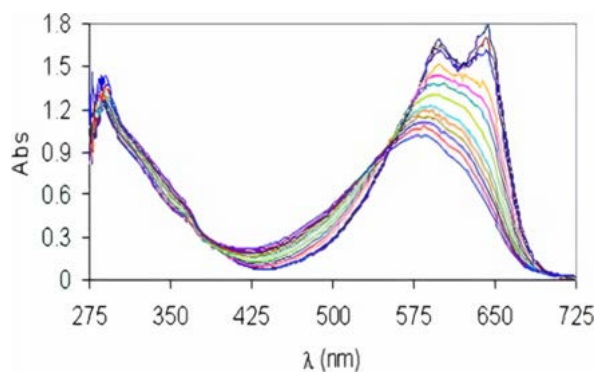
(b) NC film aged at 50°C.
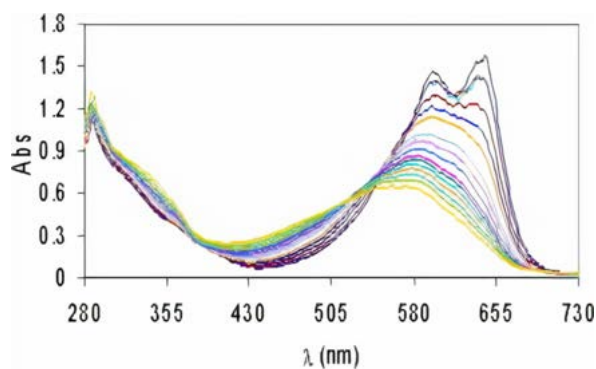
(c) NC film aged at 60°C.
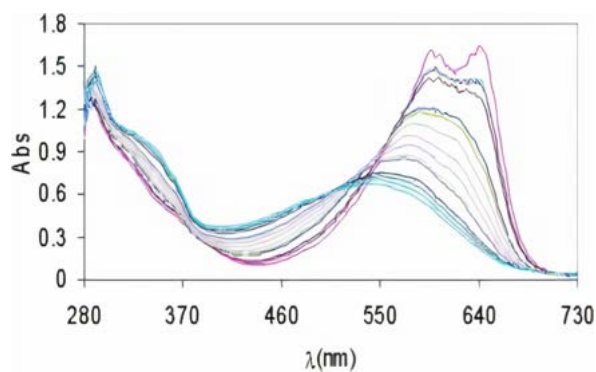
(d) NC film aged at 70°C.
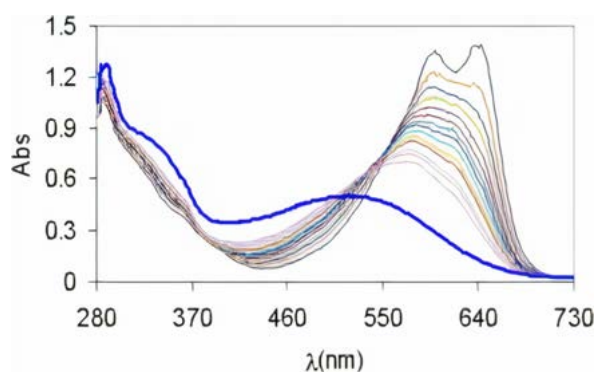
Figure 4.2: UV-vis spectra of aged NC-based film, from the work of Moniruzzaman *et al.*[88]. The peaks at 600 nm and 650 nm are attributed to the π - π^* transitions in the anthraquinone dye (SB59). Spectral lines with highest absorbance peaks in this region correspond to the sample prior to heat treatment. Appearance of peaks below 400 nm indicate the formation of new SB59 derivatives due to secondary reactions. Adapted with permission from the publisher.
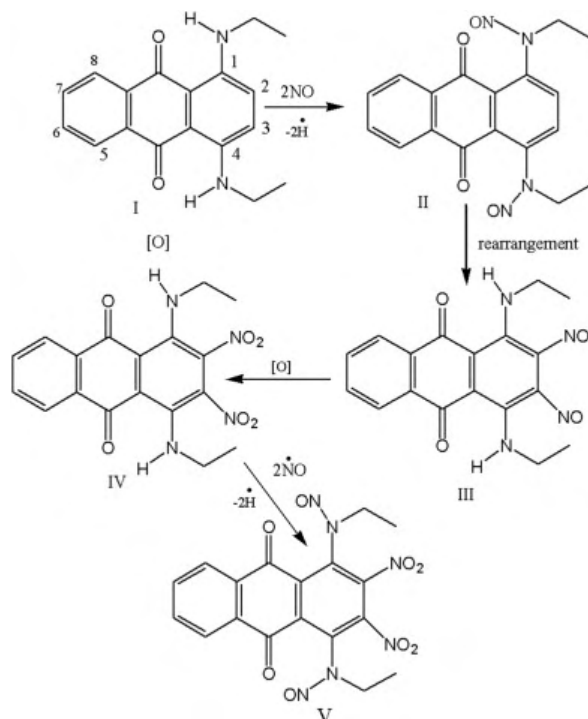
Figure 4.3: Proposed pathway for the reaction of SB59 dye with •NO released as a result of deni-
tration of NC [88]. Reproduced with permission from the publisher.

would be more likely to diffuse and react elsewhere.

Chin *et al.* proposed schemes for the propagation of secondary reactions initated by
both the thermolysis (scheme 4.1) and hydrolysis of nitrate esters (scheme 4.2) [58]. The
hydrolysis scheme was adapted from an earlier work by Camera *et al.* involving the nitrate
ester decomposition and subsequent reactions of EN (where R = CH_3CH_2 for the scheme
above) [97]. The original study included an expansion of the hydrolysis step (equation
4.11), where the involvement of NO_2^+ was illustrated (scheme 4.3).

It was highlighted by Camera, that the oxidation of alcohol by nitric acid (equation 4.6)
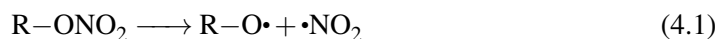is slow and thus rate-limiting. This mechanism is likely to occur *via* a series of intermediate
reactions of which the details are not known. However, following the generation of nitrous
acid, subsequent oxidations occur rapidly. According to Rigas *et al.*, alcohols are more
susceptible to wet oxidation than esters [124]. A higher concentration of unsubstituted
hydroxyl groups in the system, and therefore a fewer nitrate ester groups (or a lower degree
of substitution (DOS) value), decreases overall stabililty.

Equations 4.7 - 4.10 describe a possible branched radical chain mechanism, fed by the
nitrous and nitric acids produced by the hydrolysis and alchohol oxidation reactions during
the initiation stage. By contrast, the propagation reactions in the branched radical chain

Scheme 4.1: Thermolytic initiation proposed by Chin *et al.* [58]

$$R-ONO_2 \longrightarrow R-O\bullet + \bullet NO_2 \tag{4.1}$$

Propagation

$$R-O\bullet + \bullet NO_2 \xrightarrow{R-ONO_2} R-ONO_2 + \bullet NO + \bullet NO_2$$
$$+ N_2O_4 + H_2O + N_2O$$
$$+ CO_2 + CO + C_2H_2O$$
$$+ \text{other organic fragments} \tag{4.2}$$

$$2\bullet NO + O_2 \longrightarrow 2\bullet NO_2 \tag{4.3}$$

$$2\bullet NO_2 \rightleftharpoons N_2O_4 \tag{4.4}$$
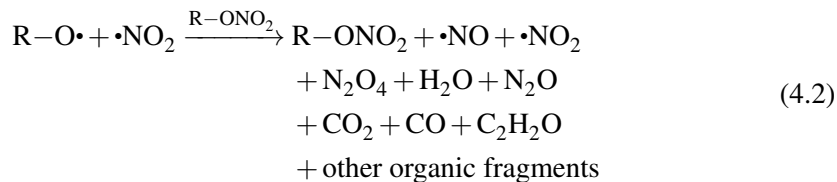
Scheme 4.2: Hydrolytic initiation proposed by Chin *et al.* [58]

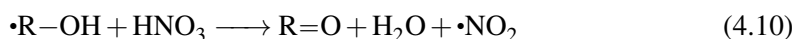$$R-ONO_2 + H_2O \longrightarrow R-OH + HNO_3 \tag{4.5}$$

$$R-OH + HNO_3 \longrightarrow R=O + HNO_2 + H_2O \tag{4.6}$$

Propagation

$$HNO_3 + HNO_2 \rightleftharpoons N_2O_4 + H_2O \tag{4.7}$$

$$N_2O_4 \rightleftharpoons 2\bullet NO_2 \tag{4.8}$$

$$R-OH + \bullet NO_2 \longrightarrow \bullet R-OH + HNO_2 \tag{4.9}$$

$$\bullet R-OH + HNO_3 \longrightarrow R=O + H_2O + \bullet NO_2 \tag{4.10}$$
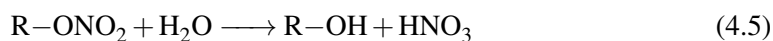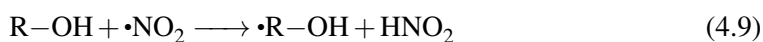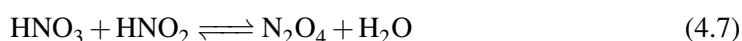
mechanism for thermolysis are poorly characterised (equation 4.2) and defined only by the observable products. Due to their rapid and varied nature, these reactions have been difficult to follow spectroscopically.

Aellig *et al.* presented an alternative scheme for the decomposition of benzyl nitrate ($R = PhCH_2$) in scheme 4.4, involving more interaction with the solvent [125]. Both the Camera/Chin and Aellig schemes above produce final end products observed in the decomposition of NC. In particular, Aellig's scheme accounts for the production of N_2O, which

Scheme 4.3: Hydrolysis scheme for ethyl nitrate from the work of Camera *et al.* [97]

$$CH_3CH_2ONO_2 + H^+ \xrightarrow{\text{fast}} CH_3CH_2ONO_2H^+ \tag{4.11}$$

$$CH_3CH_2ONO_2H^+ \xrightarrow{\text{slow}} CH_3CH_2OH + NO_2^+ \tag{4.12}$$

$$NO_2^+ + 2H_2O \xrightarrow{\text{fast}} HNO_3 + H_3O^+ \tag{4.13}$$
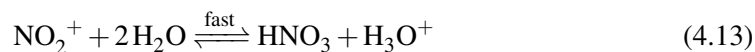
forms a significant part of the decomposition eluent [126]. Whilst the schemes do not a propose an exhaustive description of the full spectrum of reactions that take place in the NC matrix during its slow ageing, the early stage reactions of the key species responsible for decomposition are encapsulated.

Scheme 4.4: HNO$_3$ decomposition initiation proposed by Aellig *et al.* [125].

$$4\,HNO_3 \rightleftharpoons 4\cdot NO_2 + 2\,H_2O + O_2 \tag{4.14}$$

$$2\cdot NO_2 + H_2O \rightleftharpoons N_2O_4 + H_2O \tag{4.15}$$

$$N_2O_4 + H_2O \longrightarrow HNO_3 + HNO_2 \tag{4.16}$$

Propagation

$$R-OH + HNO_2 \rightleftharpoons R-ONO + H_2O \tag{4.17}$$

$$R-ONO \longrightarrow R{=}O + HNO \tag{4.18}$$

$$\cdot NO_2 + HNO \longrightarrow HNO_2 + \cdot NO \tag{4.19}$$

$$2\cdot NO + O_2 \longrightarrow 2\cdot NO_2 \tag{4.20}$$

Termination

$$2\,HNO \longrightarrow HON{=}NOH \tag{4.21}$$

$$HON{=}NOH \longrightarrow N_2O + H_2O \tag{4.22}$$
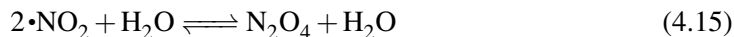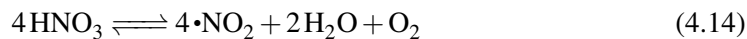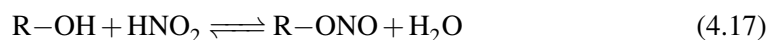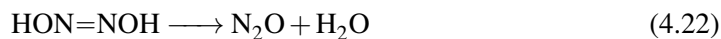
It is widely agreed that first-stage decomposition follows a first-order process (or pseudo-first order, with respect to hydrolysis reactions). A number of studies observe catalytic rate of decay for the longer-term aging processes. Dauerman and Tajima [127] observed that when NC was treated with NO$_2$ gas before heating, the time required for sample ignition halved. He suggested that the NO$_2$ adsorbed onto the surface acted as a catalysing agent.

Neutral and alkaline hydrolysis reactions follow a pseudo-first order process, however it has been suggested that the presence of acid facilitates a catalytic rate of degradation after an initial incubation period. Multiple studies have addressed the decomposition reactions of nitrate esters following the initial scission of the nitrate group [98, 97, 128, 93, 101]. In their work looking into the atmospheric reactions of methynitrate and methylperoxy nitrate Arenas *et al.* suggested it was possible for the homolytic denitration reaction of methynitrate to share a common peroxy intermediate with the peroxide [129]. This could account for some of the lower order NO$_x$ generated. In this section, secondary and extended reaction schemes for the low temperature ageing of NC are explored. Decomposition pathways

defined by Chin, Camera *et al.* and Aellig *et al.* are probed to determine the reactions responsible for the experimentally observed degradation products. The reactions found to be energetically feasible from the proposed routes will be scrutinised to determine whether an autocatalytic pathway can be formed from the thermodynamically validated reaction schemes.

4.2 Methodology

The reactions proposed by Chin *et al.*, Camera *et al.* and Aellig *et al.* were used to construct possible degradation routes for NC, each route starting with either the products of homolytic fission, elimination of HNO_2 or acid hydrolysis. The energies of each reaction in the schemes above were determined after optimisation of the individual reactant and product species. Pathways were constructed based on propagation of the given reactions in a stepwise fashion; subsequent reactions were dependent on the products generated in preceding steps. An abundance of water and oxygen were assumed present in the system, attributed to air exposure under the wetted storage conditions of NC. Unsubstituted alcohol moieties (R-OH) were also presumed abundant due to incomplete nitration during the synthesis of NC [130], and re-generation following denitration *via* hydrolysis. The schemes were modelled with ethyl nitrate (EN) as a smaller test system, then expanded to the NC monomer. Free energies of reaction (ΔG_r) at 298.15 K were used to determine the feasibility of each reaction:

$$\Delta G_r = \Delta G_{product} - \Delta G_{reactant} \qquad (4.23)$$

Where computational or experimental literature values for molecular energies or for reactions energies were available, these were compared with the results generated here. For the cases where the ΔG_r was large and positive, the reaction was omitted from the constructed reaction schemes as it would be unlikely to occur spontaneously under ambient ageing conditions, even when considering the possibility of increased heating in the system as degradation progressed.

4.2.1 Computational details

All geometry optimisations were conducted in G09, using the ωB97X-D and B3LYP functionals. Optimisations and thermochemistry calculations were performed to the level of 6-31+G(2df,p) with tight convergence criteria (max. force 1.5×10^{-5} H/Bohr, RMS force 1.0×10^{-5}, max. displacement 6.0×10^{-5} H/Bohr and RMS displacement 4.0×10^{-5}

H/Bohr, chapter 2 table 2.1) and zero point energy corrected. Calculations were repeated in both vacuum and with a PCM using water (ε=78.4) to introduce implicit solvent effects. Chemical species were constructed using Gauss View 5.0.8 (GView) [75] and for molecules of more than 3 atoms, the GView "Clean" function was used to re-order atoms to a preliminary starting geometry. Energies of optimised structures were checked against literature values listed on NIST Computational Chemistry Comparison and Benchmark Database [131] if analogous molecules to a similar level of theory existed. In most cases, the exact same level of theory was not available but a similar level could still be meaningfully referenced; for example, ωB97X-D/ 6-31G(d,p) instead of ωB97X-D/ 6-31+G(2df,p) was available for most of the common small molecules. These comparisons are detailed alongside the calculated energies in the text.
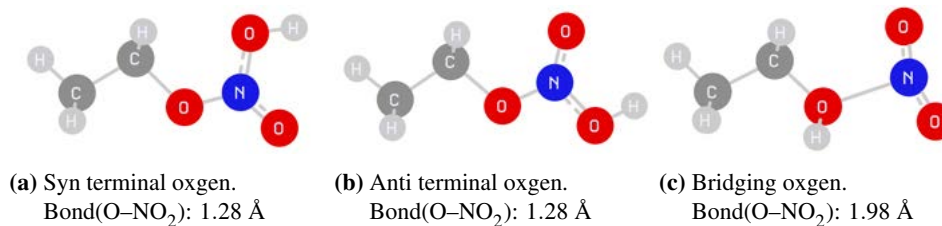
4.3   Results and Discussion

Individual molecules were optimised and their energies were calculated to evaluate the ΔG for each of the reactions in schemes 4.1-4.4 proposed by Chin *et al.*, Camera *et al.* and Aellig *et al.*. The protonation of EN was inspected to determine whether the protonation site matched that of NC, where the bridging site was the most likely to lead to hydrolytic denitration. This would indicate that EN followed the same hydrolytic mechanism, and was therefore likely to share the same extended decomposition scheme initiated by hydrolysis. The proton was placed at each of the possible terminal and bridging sites around the nitrate, and the energy for each isomer was calculated. Table 4.1 shows the protonation energies for the three different oxygen sites on EN. Despite the terminal (syn) oxygen possessing the most thermodynamically favourable energy of protonation, inspection of the reaction geometries (figure 4.4) shows that the bridging structure most resembles that expected for the liberation of the NO_2^+ group at the next step, as was observed in the case of NC (section 3.3.2.1). The higher $\Delta G_{proton.}$ arises from the elongation of the $O-NO_2$ bond that allows stabilisation of the bridging site, whilst preparing to lose the NO_2^+. Further studies involving protonated EN used the values and geometry associated with the protonated bridging site.

The combined list of calculated energies for the reactions in all schemes, for both EN and the NC monomer, are listed in table 4.2. The obtained energies for the formation of N_2O_4 from 2•NO_2 were are out of the experimentally recorded range of 4.7 - 5.9 kcal mol^{-1} [132] (from calculation: ωB97X-D/ 6-31+G(2df,p) ΔG_r = 0.1 kcal mol^{-1} in vacuum and

Table 4.1: Free energies of protonation for each oxygen site on EN.

Protonated site		$\Delta G_{\text{proton.}}$ /kcal mol^{-1}			
		ωB97X-D	PCM	B3LYP	PCM
Terminal (syn)	$CH_3CH_3ONO_2H^+$	-12.3	8.8	-13.8	5.6
Terminal (anti)	$CH_3CH_3ONO_2H^+$	-9.5	9.5	-11.1	5.6
Bridging	$CH_3CH_3O(H^+)NO_2$	-9.3	9.1	-15.3	6.7

(a) Syn terminal oxgen.
Bond(O–NO$_2$): 1.28 Å

(b) Anti terminal oxgen.
Bond(O–NO$_2$): 1.28 Å

(c) Bridging oxgen.
Bond(O–NO$_2$): 1.98 Å

Figure 4.4: Optimised geometries of the possible protonation sites on EN.

1.5 kcal mol^{-1} in water, and B3LYP/ 6-31+G(2df,p), ΔG_r = -0.5 kcal mol^{-1} in vacuum and -0.2 kcal mol^{-1} in water). The B3LYP result incorrectly predicts that the reaction is spontaneous under ambient conditions. This error may arise from a number of factors, including the limitation to short-range interactions in B3LYP, the general tendency of density functional methods to under predict reaction energies, or the geometry optimisation procedure, whereby a small variation or imperfect minimisation in the obtained optimised structures for the reaction species is amplified when combined for the calculation of reaction energies.

For the reaction of $HNO_3 + HNO_2 \rightleftharpoons N_2O_4 + H_2O$ in the gas phase, ωB97X-D/ 6-31+G(2df,p) gave ΔG_r = -2.2 kcal mol^{-1} and B3LYP/ 6-31+G(2df,p) gave ΔG_r = -5.1 kcal mol^{-1}. The corresponding published theoretical reaction energies calculated at ωB97X-D/ 6-31+G(d,p) and B3LYP/ 6-31+G(d,p) were -1.0 kcal mol^{-1} and -4.3 kcal mol^{-1} respectively. The literature and calculated values cannot be directly cross-referenced as the applied basis sets differ, however it can be seen that in either set there is a large relative disparity between the two functionals. Values are lower for B3LYP likely as a result of neglect of mid to long-range correlations that have been included in ωB97X-D; it is therefore expected for the B3LYP result to more heavily underpredict reaction energies when these interactions are signficant in the studied system [29]. This is illustrated in the energies of N_2O_4, where the long-range interaction of each nitrogen with oxygens of the other nitrogen group are missed, and the B3LYP/ 6-31+G(2df,p) energy falls below the ωB97X-D energy by 89 kcal mol^{-1}.

Table 4.2: Calculated energies for the nitrate ester decomposition reactions proposed by Camera *et al.*, Chin *et al.* and Aellig *et al.* [97, 58, 125]. R = CH_3CH_2 for ethyl nitrate (EN), and R = $(H_3CO)_2C_6H_9O_3$ (bi-methoxy capped glucopyraonse monomer unit) for NC. The PCM model applied was water ($\varepsilon = 78.4$).
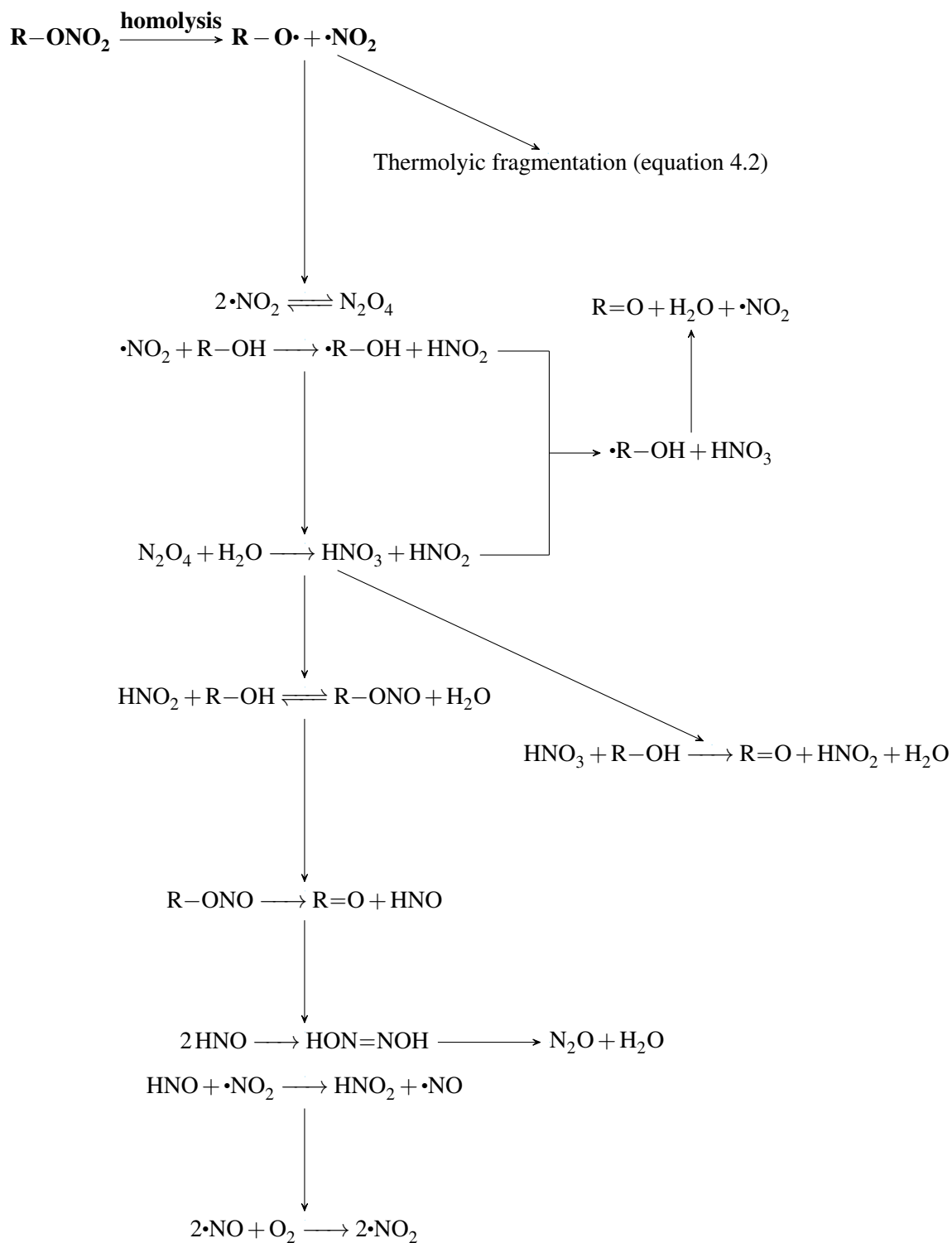
Reaction	ΔG_r /kcal mol^{-1}			
	ωB97X-D	PCM	B3LYP	PCM
$N_2O_4 + H_2O \longrightarrow HNO_3 + HNO_2$	2.3	1.9	5.1	4.2
$N_2O_4 \rightleftharpoons 2 \cdot NO_2$	0.1	1.5	−0.5	−0.2
Radical reactions				
$\cdot NO_2 + HNO \longrightarrow HNO_2 + \cdot NO$	−28.2	−28.7	−27.3	−27.6
$2 \cdot NO + O_2 \longrightarrow 2 \cdot NO_2$	−20.8	−22.0	−21.2	−22.2
Acid reactions				
$HNO_3 + HNO_2 \rightleftharpoons N_2O_4 + H_2O$	−2.2	−1.8	−5.1	−4.2x
$4 HNO_3 \rightleftharpoons 4 \cdot NO_2 + 2 H_2O + O_2$	53.4	58.4	42.6	46.9
$2 HNO \longrightarrow HON{=}NOH$	−39.0	−39.7	−36.6	−37.4
$HON{=}NOH \longrightarrow N_2O + H_2O$	−48.1	−48.2	−50.6	−50.7
Ionic reactions				
$NO_2{}^+ + 2 H_2O \rightleftharpoons HNO_3 + H_3O^+$	−0.9	−1.3	1.8	2.5
EN (R = CH_3CH_2)				
$R{-}ONO_2 + H_2O \longrightarrow R{-}OH + HNO_3$	4.6	5.2	4.0	4.9
$R{-}OH + HNO_3 \longrightarrow R{=}O + HNO_2 + H_2O$	−34.1	−38.4	−37.6	−41.8
$R{-}OH + \cdot NO_2 \longrightarrow \cdot R{-}OH + HNO_2$	16.4	13.9	15.9	13.7
$\cdot R{-}OH + HNO_3 \longrightarrow R{=}O + H_2O + \cdot NO_2$	−50.4	−52.4	−53.5	−55.5
$R{-}OH + HNO_2 \rightleftharpoons R{-}ONO + H_2O$	−3.2	−3.3	−2.6	−2.9
$R{-}ONO \longrightarrow R{=}O + HNO$	−1.5	−5.8	−4.4	−8.5
NC monomer (R = $(H_3CO)_2C_6H_9O_3$)				
$R{-}ONO_2 + H_2O \longrightarrow R{-}OH + HNO_3$	0.7	5.6	0.6	−0.7
$R{-}OH + HNO_3 \longrightarrow R{=}O + HNO_2 + H_2O$	−36.7	−38.3	−41.7	−41.7
$R{-}OH + \cdot NO_2 \longrightarrow \cdot R{-}OH + HNO_2$	14.7	11.2	13.0	23.2
$\cdot R{-}OH + HNO_3 \longrightarrow R{=}O + H_2O + \cdot NO_2$	−51.4	−49.5	−54.7	−56.4
$R{-}OH + HNO_2 \rightleftharpoons R{-}ONO + H_2O$	−4.4	−7.3	−4.3	−0.2
$R{-}ONO \longrightarrow R{=}O + HNO$	−2.9	−1.7	−6.8	−11.2

Simplified schemes for the possible ageing reactions of nitrate esters beginning from homolytic fission, elimination of HNO_2 or acid hydrolysis are illustrated in schemes 4.5 - 4.7. The reaction of $4\,HNO_3 \rightleftharpoons 4\,\cdot NO_2 + 2\,H_2O + O_2$ has a large, positive ΔG_r of 53.4 kcal mol^{-1} (ωB97X-D/ 631+G(2df,p) in vacuum) indicating that this process is highly unlikely to proceed in given ambient temperatures, and so was omitted from the drawn reaction schemes.

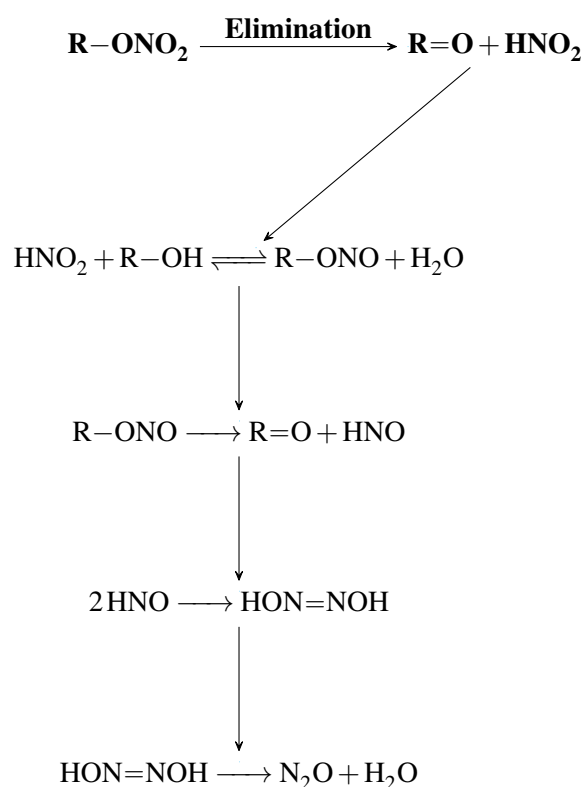When starting with the products of homolytic fission (scheme 4.5), the reaction pathway split into a branched radical chain mechanism and separate acid driven pathway. Reaction of $\cdot NO_2$ with a hydroxyl group (on either the NC monomer or denitrated EN molecule) leads to the formation of an alkyl radical which goes on to react with HNO_3 present in the environment from formation *via* other steps in the pathway, formed during the reaction of NO_2^+ in the hydrolytic scheme, or residual in the system from incomplete washing following NC synthesis, to regenerate $\cdot NO_2$. The $\cdot NO_2$ attack on $R-OH$ is expected to occur rapidly, dominating the reaction scheme but leading to increased concentration of $\cdot NO_2$ in the system to fuel other pathways. Formation of N_2O_4 from $2\cdot NO_2$ and subsequent decomposition into HNO_2 and HNO_3 drives the remaining acid reactions. HNO_3 reactions lead to further formation of $\cdot NO_2$, however, the attack of HNO_2 on hydroxyl groups on the NC backbone generates the experimentally observed end product N_2O whilst the hydroxyl group is converted to a ketone [127, 133].

The generation and re-generation of $\cdot NO_2$ and HNO_2 in the above scheme supports the theory that these may be the species responsible for the autocatalytic rate of decomposition that is observed following a first-order rate induction period [89, 90, 91]. The first-order rate is likely attributed to the denitration step, as the concentration of these species slowly increases and self-heating occurs, leading to the rapid speed-up of the post-denitration reactions. If the liberated HNO_2 does not go on to attack hydroxyl groups on the NC backbone, it is then free to undergo a conversion to generate further $\cdot NO_2$ in the reactions $HNO_2 + HNO_3 \longrightarrow N_2O_4 + H_2O \rightleftharpoons 2\cdot NO_2$ +H2O, indicating that the fate of all nitrogen in the system is towards the formation of $\cdot NO_2$ until it is captured in N_2O. This is supported by scheme 4.6 that begins with the elimination of HNO_2. The reactions of HNO_2 with available hydroxyl groups drives the formation of N_2O, ketone and water as the only end products. The hydrolytic scheme (scheme 4.7) involves the early generation of HNO_3, conversion to HNO_2 and then enters a similar radical chain mechanism to that observed in

$$\mathbf{R-ONO_2} \xrightarrow{\textbf{homolysis}} \mathbf{R-O\cdot + \cdot NO_2}$$

Thermolyic fragmentation (equation 4.2)

$$2\cdot NO_2 \rightleftharpoons N_2O_4 \qquad\qquad R{=}O + H_2O + \cdot NO_2$$

$$\cdot NO_2 + R{-}OH \longrightarrow \cdot R{-}OH + HNO_2$$

$$\cdot R{-}OH + HNO_3$$

$$N_2O_4 + H_2O \longrightarrow HNO_3 + HNO_2$$

$$HNO_2 + R{-}OH \rightleftharpoons R{-}ONO + H_2O$$

$$HNO_3 + R{-}OH \longrightarrow R{=}O + HNO_2 + H_2O$$

$$R{-}ONO \longrightarrow R{=}O + HNO$$

$$2\,HNO \longrightarrow HON{=}NOH \longrightarrow N_2O + H_2O$$

$$HNO + \cdot NO_2 \longrightarrow HNO_2 + \cdot NO$$

$$2\cdot NO + O_2 \longrightarrow 2\cdot NO_2$$

Scheme 4.5: Proposed degradation pathway starting from the homolytic fission of the nitrate ester, derived from the schemes presented by Camera *et al.* [97] and Aellig[125].
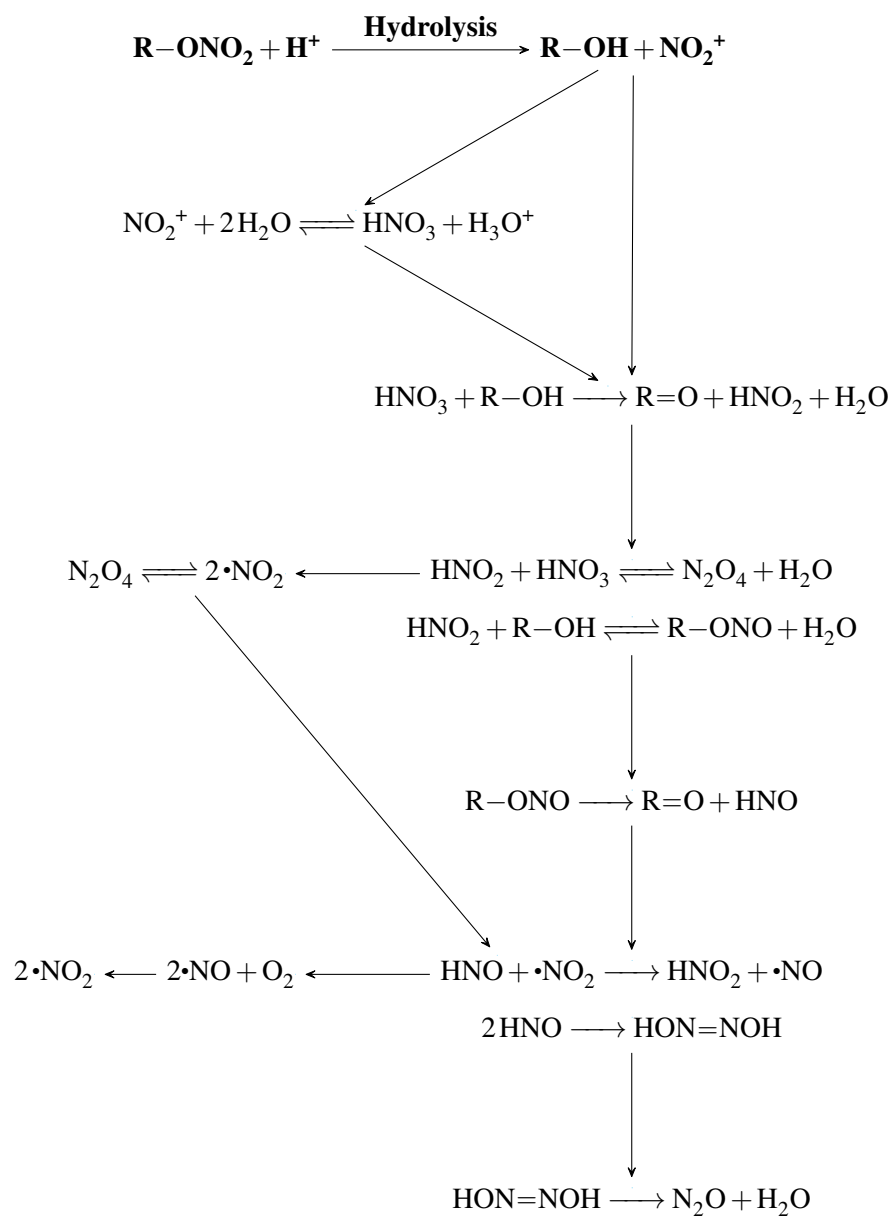
the homolytic pathway concluding in formation of N_2O, $\cdot NO_2$ and hydroxyl conversion to ketone. For all schemes, R=O and N_2O were terminating species. Whilst N_2O is released into the environment, R=O remains in the system may go on to participate in further decomposition reactions leading to ring opening. It is important to note that these schemes are not exhaustive, but rather a limited view of the possible steps that may take place during ageing based on the presence of nitrate and acid species expected to be in the closed system. Deeper degradation of the NC backbone has not been considered here and should the next step for future work.

$$R-ONO_2 \xrightarrow{\textbf{Elimination}} R=O + HNO_2$$

$$HNO_2 + R-OH \rightleftharpoons R-ONO + H_2O$$

$$R-ONO \longrightarrow R=O + HNO$$

$$2\,HNO \longrightarrow HON=NOH$$

$$HON=NOH \longrightarrow N_2O + H_2O$$

Scheme 4.6: Proposed degradation pathway starting from the elimination of HNO_2 from a nitrate ester, derived from the schemes presented by Camera *et al.* [97] and Aellig[125].

4.4 Summary

In this section, the energies (ΔG_r) for each of the reactions in the combined nitrate ester decomposition schemes proposed by Camera *et al.*, Chin *et al.* and Aellig *et al.* were evaluated using the ωB97X-D and B3LYP functionals [97, 58, 125]. Obtained energy values were compared to literature where available [131], confirming that individual molecular free energy and reaction energy values fell within the expected theoretical and experimental bounds. Decomposition reactions involving an alkyl nitrate were initially performed with

$$R-ONO_2 + H^+ \xrightarrow{\textbf{Hydrolysis}} R-OH + NO_2^+$$

$$NO_2^+ + 2H_2O \rightleftharpoons HNO_3 + H_3O^+$$

$$HNO_3 + R-OH \longrightarrow R{=}O + HNO_2 + H_2O$$

$$N_2O_4 \rightleftharpoons 2{\cdot}NO_2 \longleftarrow HNO_2 + HNO_3 \rightleftharpoons N_2O_4 + H_2O$$

$$HNO_2 + R-OH \rightleftharpoons R-ONO + H_2O$$

$$R-ONO \longrightarrow R{=}O + HNO$$

$$2{\cdot}NO_2 \longleftarrow 2{\cdot}NO + O_2 \longleftarrow HNO + {\cdot}NO_2 \longrightarrow HNO_2 + {\cdot}NO$$

$$2\,HNO \longrightarrow HON{=}NOH$$

$$HON{=}NOH \longrightarrow N_2O + H_2O$$

Scheme 4.7: Proposed degradation pathway starting from the acid hydrolysis of a nitrate ester, derived from the schemes presented by Camera *et al.* [97] and Aellig[125].

ethyl nitrate (EN) and then repeated for NC.

Starting from the three denitration mechanisms explored in chapter 3, using the reactions listed in the schemes above, three different degradation pathways were constructed. It can be seen that it is the HNO_2 species conversion of $R-OH \rightarrow R-ONO \rightarrow R=O$ that drives oxidation in all three schemes, playing a central role in the extended degradation scheme of NC. The regeneration of $\cdot NO_2$ indicated that this was the species most likely responsible for the autocatalytic rate of degradation observed experimentally [94, 134, 135].

Decomposition further than formation of the ketone species was not studied here. To understand the full ageing behaviour of NC and comprehensively attribute experimentally observed products to individual reactions, the relative rate of each of the mechanistic schemes above, in addition to ring fission and peeling-off reactions that disrupt the NC chain, must be probed. A limitation to this work is that the reaction energies were calculated from the molecules optimised in isolation. In practice, there are energy barriers associated with complexation of reactant compounds and solvation energies as newly liberated species depart from the NC backbone to freely move in the solvent. To account for these, a more detailed study to evaluate complexation and solvation energies is needed. The diffusion behaviour of individual reactant species through the NC bulk both in vacuum and solvent, and as the reaction mixtures evolves, should also be considered.

Chapter 5

Conclusion and future work

5.1 Conclusion

Since winning a medal at the World's Fair in London in 1862 as the first man-made plastic [136, 137], NC has become a central component in the manufacturing of everyday items across a whole spectrum of critical applications, from kitchenware to rocket fuel [138]. As has been demonstrated by this study and the extensive years of research since its first discovery, the degradation behaviour of NC is multi-staged and subject to high variation. The interplay of thermal triggers, hydrolytic initiation, as well as other factors not discussed here such as ultraviolet (UV) initiation [139, 140] and physical shock [141], are all subject to the unique composition of each sample; variation owed to its biological origins and preparation method. Adding to this, the ageing reactions that occur are at the mercy of the precise environmental conditions under which the NC is stored. The final result is that the true, exhaustive reaction scheme for full decomposition has remained elusive.

In this thesis, the degradation processes in NC were explored using computational methods to elucidate the dominant processes and key reactants involved in ambient ageing. In the first section, the polymeric structure of NC was introduced. Different sized truncations and capping group approximations for polymer chain endings were tested as models for the polysaccharide. This was achieved by inspection of the partial charges, ESP and critical interaction points for monomeric, dimeric and trimeric β-glucopyranose structures. The dimer was found to be the minimum structure required to reproduce the full properties of NC within a repeat unit.

Methoxy and hydroxyl capping groups were compared; the methoxy groups provided a more sterically and chemically similar proxy for the extended polymer, following examination of charges and geometry dependent interactions. Comparison of the charge densities

and intramolecular interactions around the monomer and dimer revealed that the former exhibited an acceptable level of deviation from the dimer behaviour, particularly with reference to further investigations concentrating only on localised reaction interactions. The bi-methoxy monomer was implemented as the model for NC in later studies.

Using the monomer model, the primary steps of decomposition were explored in Chapter 3. Thermolytic denitration reactions were investigated; homolytic fission of the nitrate $O-NO_2$ bond, and elimination of HNO_2 were tested for both the PETN test case, and the NC monomer model. Good agreement with literature values was found for the reaction energies and activation energies, in case of HNO_2 elimination in both PETN and NC. The loss of $\cdot NO_2$ *via* homolysis was confirmed. For the acid hydrolysis pathway , possible protonation sites in the monomer were analysed. It was found that the proton site most amenable to denitration was the bridging oxygen position of the nitrate. Further investigations considered denitration routes beginning from isomers protonated at both the terminal (upper) and bridging sites. The denitration step was then explored *via* a series of PES scans. The stability of different possible TS ring structures involving both pre-protonation and concerted protonation-denitration was examined, in addition to the nature of the NO_2 leaving group. No stable TS structures presenting the correct vibration for denitration were isolated, however scans confirmed that the NO_2 was released as NO_2^+, with possible formation of HNO_2 at greater separations.

Proposed decomposition routes originating from the primary denitration step were collated from nitrate ester reactions in literature. Using EN as an initial test case, the energies of each reaction were evaluated to determine whether it were a viable secondary reaction step following liberation of the $\cdot NO_2$, NO_2^+ or HNO_2 following first stage decomposition. Possible decomposition schemes were constructed, mapping from the point of NO_2 liberation to the oxidation of the alcohol group. The reaction energies were determined for the NC monomer. It was found that the energies were largely favourable from a thermodynamic equilibrium perspective. The fate of the released nitrogen species was in the accumulation of N_2O or regeneration of $\cdot NO_2$, suggesting $\cdot NO_2$ as the species responsible for autocatalytic processes in the system. Consumption of $\cdot NO_2$ in the formation of acids proved to be thermodynamically unfavourable.HNO_2 routes lead to the formation of N_2O without self-regeneration and HNO_3 routes lead primarily to formation of $\cdot NO_2$. This indicates that HNO_2 was unlikely to be a direct contributor to catalysis, and that HNO_3 was the pre-

cursor to the •NO$_2$ catalytic species, acknowledging experimental observations that HNO$_3$ appeared to facilitate autocatalysis [93].

Following the successful application of the monomer model in the investigation of denitration and protonation reactions of NC, further studies repeating the mechanisms explored here using the dimer (and trimer models, where feasible) would be extremely valuable. Possible synergistic effects of neighbouring nitrate groups on adjacent rings, in addition to increased steric factors, are likely to change the energetics and favourability of attack and protonation sites, thus altering the likelihood of denitration at each ring position. Interchain hydrogen bonding, largely dependent on unsubstituted hydroxyl groups, is also likely to alter the contribution to hydrolysis in particular. Porosity to solvents is influenced by local crystallinity and packing [142, 143], and is sensitive to the spatial arrangements of individual hydroxyl groups [144, 145, 63]. Molecular packing will determine the ease at which liberated degradation products can diffuse through and escape the NC matrix. It can be surmised that there exists certain decomposition pathways with corresponding reactions that are solely structure dependent.

Whilst this work has not exhaustively explored the myriad reactions that may occur in the complex ageing procedures of NC, it has established the key reactions of the early stages of degradation, with presentation of an effective truncation of the polymeric structure applicable for further study in the topic. Key competing reactions for the denitration step, the identity of nitrogen species released and their role in the longer-range decomposition process has been presented. The conclusion of this project sets the scope for subsequent investigations into the later-stage reaction processes that lead to deeper degradation of the NC backbone.

5.2   Further Work

In addition to expansion of the NC model to larger dimer and trimer units, the existing NC model may be refined by conducting a more rigorous examination of the subtle variations in geometry. Conformational scans, in particular for the C6 chain and for the orientation of the rings within the trimer, would benefit identification of other low energy structures likely to be present in the natural polymer. Here, only the denitration schemes for the singly nitrated NC monomer were documented. The differing stabilities of NC at varying levels of nitration will undoubtedly affect the reactivity at each site. Propagation of different nitration level and conformational structures through the denitration and secondary decomposition

schemes may reveal alternative reactions, or alter the balance of products obtained.

Classical molecular dynamics (MD) techniques would also provide further insight into the diffusion of the released products, and their interaction with the wider polymer. Studies involving the interaction of NC with plasticisers has effectively probed the diffusion rates of plasticiser migration, which is of key interest in the preservation of stable NC product formulations [146].

Another avenue of interest is in the exploration of other transition structures for the denitration stage, and for further degradation following formation of the ketone. The inclusion of additional explicit water molecules or water clusters is likely required to stabilise TS that were previously not viable (chapter 3 figure 3.10), highlighting the need for further understanding of NC-solvent interactions. A starting reference work would be the modelling of pentahydrate complexes around glucose by Momany *et al.* [23], with extension to a hybrid quantum mechanics/molecular mechanics (QM/MM) approach to treatment of solvation shells. Ab-initio molecular dynamics (AIMD) techniques may be effective for investigation into the interactions of both water and acids with NC, offering possible insight into the effect of increasing acid concentration on the protonation behaviour and water clustering around monomer, dimer and trimer structures at different DOS [147].

A natural extension to the study of the secondary reactions driving decomposition is the expansion to a wider range of possible reaction pathways. These may include the widely documented mechanisms studied for glucose, such as the conversion to hydroxymethyfurfural (HMF), whereby the 6-membered ring is converted to a 5-membered ring (figure 5.1) [148, 149, 150]; furan and other aromatic species have been observed in NC degradation residues [151]. This is in addition to further studies of possible ring opening mechanisms and chain scission reactions, in order to fully account for the broad spectrum of experimentally observed degradation products in infra-red spectroscopy (IR) and nuclear magnetic resonance spectroscopy (NMR) measurements [152, 153, 127, 154, 155].

Figure 5.1: The conversion of glucose to hydroxymethylfurfural (HMF) with a) showing the pro-
posed reaction scheme, and b) displaying a possible mechanistic pathway, from the *ab
initio* molecular dynamics (AIMD) study by Qian *et al.* [122].

(a) Conversion of glucose (I) to HMF (III) *via* a furan aldehyde intermediate (II).

β-D-glucose   furan aldehyde (intermediate)   HMF
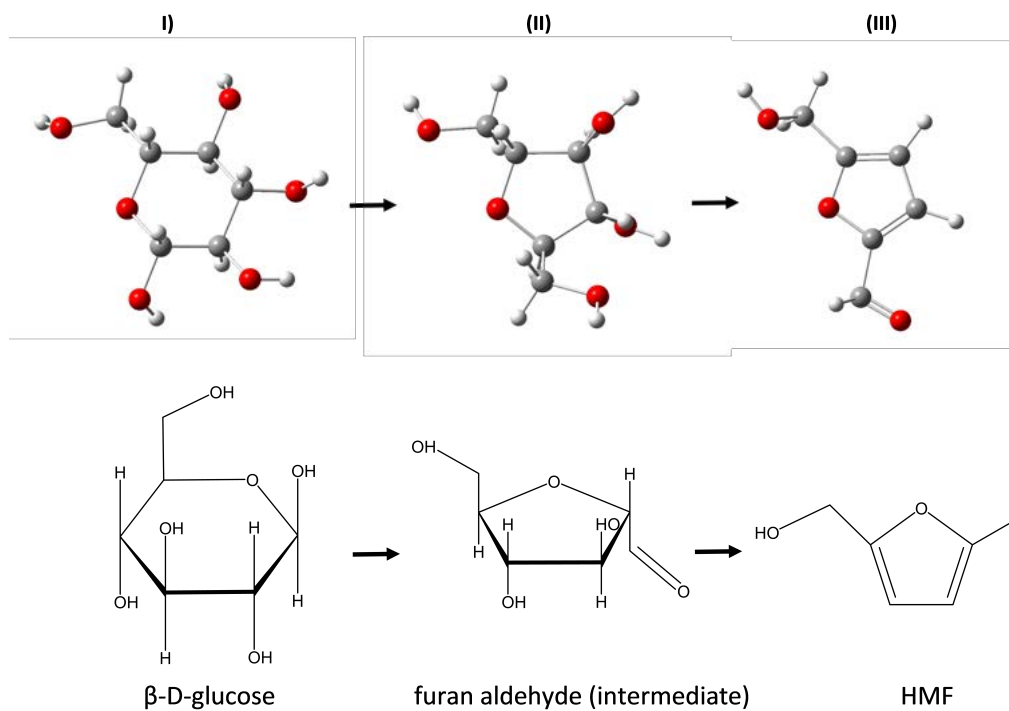
(b) (1): Protonation of C2−OH on β-D-glucose, (2): breakage of the C2−O2 Bond, (3): the formation of the
C2−O5 bond during glucose conversion to HMF.
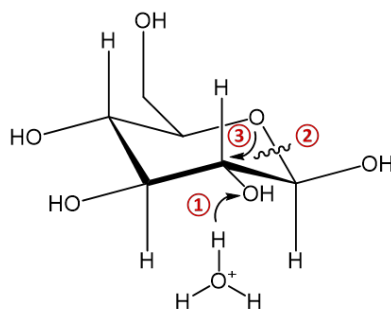
Bibliography

[1] E. Schrödinger. An undulatory theory of the mechanics of atoms and molecules. *Phys. Rev.*, 28:1049–1070, Dec 1926.

[2] Christopher J. Cramer. *Essentials of computational chemistry: Theories and models*, chapter 9, pages 338–340. Number 2. Wiley, 2004.

[3] J. C. Slater. The theory of complex spectra. *Phys. Rev.*, 34:1293–1322, Nov 1929.

[4] Frank Jensen. *Introduction to Computational Chemistry*, chapter 2, pages 22–35. Wiley, 2 edition, 2007.

[5] D. R. Hartree. The wave mechanics of an atom with a non-coulomb central field. part iii. term values and intensities in series in optical spectra. *Mathematical Proceedings of the Cambridge Philosophical Society*, 24(3):426–437, 1928.

[6] D. R. Hartree. The distribution of charge and current in an atom consisting of many electrons obeying dirac's equations. *Mathematical Proceedings of the Cambridge Philosophical Society*, 25(2):225–236, 1929.

[7] V. Fock. Näherungsmethode zur lösung des quantenmechanischen mehrkörperproblems. *Zeitschrift für Physik*, 61(1):126–148, 1930.

[8] Ambili S. Menon and Leo Radom. Consequences of spin contamination in unrestricted calculations on open-shell species: Effect of hartree-fock and møller-plesset contributions in hybrid and double-hybrid density functional theory approaches. *J. Phys. Chem. A*, 112(50):13225–13230, December 2008.

[9] P. Hohenberg and W. Kohn. Inhomogeneous electron gas. *Phys. Rev.*, 136:B864–B871, Nov 1964.

[10] W. Kohn and L. J. Sham. Self-consistent equations including exchange and correlation effects. *Phys. Rev.*, 140:A1133–A1138, Nov 1965.

[11] A. D. Becke. Density-functional exchange-energy approximation with correct asymptotic behavior. *Phys. Rev. A*, 38:3098–3100, Sep 1988.

[12] Chengteh Lee, Weitao Yang, and Robert G. Parr. Development of the colle-salvetti correlation-energy formula into a functional of the electron density. *Phys. Rev. B*, 37:785–789, Jan 1988.

[13] John P. Perdew, Kieron Burke, and Matthias Ernzerhof. Generalized gradient approximation made simple. *Phys. Rev. Lett.*, 77:3865–3868, Oct 1996.

[14] B. Hammer, L. B. Hansen, and J. K. Nørskov. Improved adsorption energetics within density-functional theory using revised perdew-burke-ernzerhof functionals. *Phys. Rev. B*, 59:7413–7421, Mar 1999.

[15] John P. Perdew, Adrienn Ruzsinszky, Gábor I. Csonka, Oleg A. Vydrov, Gustavo E. Scuseria, Lucian A. Constantin, Xiaolan Zhou, and Kieron Burke. Restoring the density-gradient expansion for exchange in solids and surfaces. *Phys. Rev. Lett.*, 100:136406, Apr 2008.

[16] Zhigang Wu and R. E. Cohen. More accurate generalized gradient approximation for solids. *Phys. Rev. B*, 73:235116, Jun 2006.

[17] Jürgen Gräfenstein and Dieter Cremer. The self-interaction error and the description of non-dynamic electron correlation in density functional theory. *Theoretical Chemistry Accounts*, 123(3):171–182, 2009.

[18] Junwei Bao, Laura Gagliardi, and Donald G. Truhlar. Self-interaction error in density functional theory: An appraisal. *J. Phys. Chem. Lett.*, 9(9):2353–2358, May 2018.

[19] Igor Ying Zhang, Jianming Wu, and Xin Xu. Extending the reliability and applicability of b3lyp. *Chem. Commun.*, 46(18):3057–3070, 2010.

[20] Axel D. Becke. Density-functional thermochemistry. iii. the role of exact exchange. *J. Chem. Phys.*, 98(7):5648–5652, April 1993.

[21] Axel D. Becke. A new mixing of hartree-fock and local density-functional theories. *J. Chem. Phys.*, 98(2):1372–1377, January 1993.

[22] Udo Schnupf, J. L. Willett, Wayne B. Bosma, and Frank A. Momany. Dft study of α- and β-d-allopyranose at the b3lyp/6-311++g** level of theory. *Carbohydrate Research*, 342(2):196–216, 2007.

[23] F. A. Momany, M. Appell, G. Strati, and J. L. Willett. B3lyp/6-311++g** study of monohydrates of α- and β-d-glucopyranose: hydrogen bonding, stress energies, and effect of hydration on internal coordinates. *Carbohydrate Research*, 339(3):553–567, 2004.

[24] Susan N. Pieniazek, Fernando R. Clemente, and Kendall N. Houk. Sources of error in dft computations of cc bond formation thermochemistries: *pi→sigma* transformations and error cancellation by dft methods. *Angewandte Chemie International Edition*, 47(40):7746–7749, September 2008.

[25] Peter R. Schreiner. Relative energy computations with approximate density functional theory–a caveat! *Angewandte Chemie International Edition*, 46(23):4217–4219, June 2007.

[26] Stefan Grimme. Accurate description of van der waals complexes by density functional theory including empirical corrections. *J. Comput. Chem.*, 25(12):1463–1473, September 2004.

[27] Stefan Grimme. Semiempirical gga-type density functional constructed with a long-range dispersion correction. *J. Comput. Chem.*, 27(15):1787–1799, November 2006.

[28] Jeng-Da Chai and Martin Head-Gordon. Systematic optimization of long-range corrected hybrid density functionals. *J. Chem. Phys.*, 128(8):084106, February 2008.

[29] Jeng-Da Chai and Martin Head-Gordon. Long-range corrected hybrid density functionals with damped atom-atom dispersion corrections. *Phys. Chem. Chem. Phys.*, 10(44):6615–6620, 2008.

[30] Axel D. Becke. Density-functional thermochemistry. v. systematic optimization of exchange-correlation functionals. *J. Chem. Phys.*, 107(20):8554–8560, November 1997.

[31] Qin Wu and Weitao Yang. Empirical correction to density functional theory for van der waals interactions. *J. Chem. Phys.*, 116(2):515–524, December 2001.

[32] R. Ditchfield, W. J. Hehre, and J. A. Pople. Self-consistent molecular-orbital methods. ix. an extended gaussian-type basis for molecular-orbital studies of organic molecules. *J. Chem. Phys.*, 54(2):724–728, January 1971.

[33] Frans B. van Duijneveldt, Jeanne G. C. M. van Duijneveldt-van de Rijdt, and Joop H. van Lenthe. State of the art in counterpoise theory. *Chem. Rev.*, 94(7):1873–1885, November 1994.

[34] Ł. M. Mentel and E. J. Baerends. Can the counterpoise correction for basis set superposition effect be justified? *J. Chem. Theory Comput.*, 10(1):252–267, January 2014.

[35] M. J. Frisch, G. W. Trucks, H. B. Schlegel, G. E. Scuseria, M. A. Robb, J. R. Cheeseman, G. Scalmani, V. Barone, B. Mennucci, G. A. Petersson, H. Nakatsuji, M. Caricato, X. Li, H. P. Hratchian, A. F. Izmaylov, J. Bloino, G. Zheng, J. L. Sonnenberg, M. Hada, M. Ehara, K. Toyota, R. Fukuda, J. Hasegawa, M. Ishida, T. Nakajima, Y. Honda, O. Kitao, H. Nakai, T. Vreven, J. A. Montgomery, Jr., J. E. Peralta, F. Ogliaro, M. Bearpark, J. J. Heyd, E. Brothers, K. N. Kudin, V. N. Staroverov, R. Kobayashi, J. Normand, K. Raghavachari, A. Rendell, J. C. Burant, S. S. Iyengar, J. Tomasi, M. Cossi, N. Rega, J. M. Millam, M. Klene, J. E. Knox, J. B. Cross, V. Bakken, C. Adamo, J. Jaramillo, R. Gomperts, R. E. Stratmann, O. Yazyev, A. J. Austin, R. Cammi, C. Pomelli, J. W. Ochterski, R. L. Martin, K. Morokuma, V. G. Zakrzewski, G. A. Voth, P. Salvador, J. J. Dannenberg, S. Dapprich, A. D. Daniels, Ö. Farkas, J. B. Foresman, J. V. Ortiz, J. Cioslowski, and D. J. Fox. Gaussian 09 revision e.01. Gaussian Inc. Wallingford CT 2009.

[36] J. B. Foresman and Æ Frisch. *Exploring Chemistry with Electronic Structure Methods*. Gaussian, Inc.: Wallingford, CT, 2 edition, 1996.

[37] A. K. Rappe, C. J. Casewit, K. S. Colwell, W. A. Goddard, and W. M. Skiff. Uff, a full periodic table force field for molecular mechanics and molecular dynamics simulations. *Journal of the American Chemical Society*, 114(25):10024–10035, 1992.

[38] Thomas A. Halgren. Merck molecular force field. i. basis, form, scope, parameterization, and performance of mmff94. *Journal of Computational Chemistry*, 17(5-6):490–519, 1996.

[39] Thomas A. Halgren. Merck molecular force field. ii. mmff94 van der waals and electrostatic parameters for intermolecular interactions. *Journal of Computational Chemistry*, 17(5-6):520–552, 1996.

[40] Thomas A. Halgren. Merck molecular force field. iii. molecular geometries and vibrational frequencies for mmff94. *Journal of Computational Chemistry*, 17(5-6):553–586, 1996.

[41] Thomas A. Halgren and Robert B. Nachbar. Merck molecular force field. iv. conformational energies and geometries for mmff94. *Journal of Computational Chemistry*, 17(5-6):587–615, 1996.

[42] Thomas A. Halgren. Merck molecular force field. v. extension of mmff94 using experimental data, additional computational data, and empirical rules. *Journal of Computational Chemistry*, 17(5-6):616–641, 1996.

[43] Faranak Bazooyar, Frank A. Momany, and Kim Bolton. Validating empirical force fields for molecular-level simulation of cellulose dissolution. *Computational and Theoretical Chemistry*, 984:119–127, 2012.

[44] Mckay W. Easton, John J. Nash, and Hilkka I. Kenttämaa. Dehydration pathways for glucose and cellobiose during fast pyrolysis. *J. Phys. Chem. A*, 122(41):8071–8085, October 2018.

[45] Anne Imberty and Serge Pérez. Structure, conformation, and dynamics of bioactive oligosaccharides: Theoretical approaches and experimental validations. *Chem. Rev.*, 100(12):4567–4588, December 2000.

[46] Niranjan Govind, Max Petersen, George Fitzgerald, Dominic King-Smith, and Jan Andzelm. A generalized synchronous transit method for transition state location. *Computational Materials Science*, 28(2):250–258, 2003.

[47] O. Tapia and O. Goscinski. Self-consistent reaction field theory of solvent effects. *null*, 29(6):1653–1661, June 1975.

[48] S. Miertuš, E. Scrocco, and J. Tomasi. Electrostatic interaction of a solute with a continuum. a direct utilizaion of ab initio molecular potentials for the prevision of solvent effects. *Chemical Physics*, 55(1):117–129, 1981.

[49] Jacopo Tomasi, Benedetta Mennucci, and Roberto Cammi. Quantum mechanical continuum solvation models. *Chem. Rev.*, 105(8):2999–3094, August 2005.

[50] Andrew R. Leach. *Molecular Modelling: Principles and Applications*. Prentice Hall, 2 edition, 2001.

[51] Heather B. Mayes and Linda J. Broadbelt. Unraveling the reactions that unravel cellulose. *J. Phys. Chem. A*, 116(26):7098–7106, July 2012.

[52] Zhenhuan Li, Kunmei Su, Jun Ren, Dongjiang Yang, Bowen Cheng, Chan Kyung Kim, and Xiangdong Yao. Direct catalytic conversion of glucose and cellulose. *Green Chem.*, 20(4):863–872, 2018.

[53] Richard F. W. Bader. A quantum theory of molecular structure and its applications. *Chem. Rev.*, 91(5):893–928, July 1991.

[54] Chérif F. Matta and Russell J. Boyd. *The Quantum Theory of Atoms in Molecules: From Solid State to DNA and Drug Design*, chapter 1, page 11. WILEY-VCH Verlag, 2007.

[55] P. Balanarayan and Shridhar R. Gadre. Topography of molecular scalar fields. i. algorithm and poincaré-hopf relation. *J. Chem. Phys.*, 119(10):5037–5043, August 2003.

[56] Miaomiao Jin, Nan Luo, Guoping Li, and Yunjun Luo. The thermal decomposition mechanism of nitrocellulose aerogel. *Journal of Thermal Analysis and Calorimetry*, 121(2):901–908, 2015.

[57] Aaron L. Bluhm. Chemical characterization of nitrocellulose degradation products. Technical report, United States Army Natick Research and Development Command Natick, United States Army Natick Research and Development Command Natick, 1977.

[58] Anton Chin, Daniel S. Ellison, Sara K. Poehlein, and Myong K. Ahn. Investigation of the decomposition mechanism and thermal stability of nitrocellulose/nitroglycerine

based propellants by electron spin resonance. *Propellants, Explosives, Pyrotechnics*, 32(2):117–126, April 2007.

[59] M. Edge, N. S. Allen, M. Hayes, P. N. K. Riley, C. V. Horie, and J. Luc-Gardette. Mechanisms of deterioration in cellulose nitrate base archival cinematograph film. *European Polymer Journal*, 26(6):623–630, 1990.

[60] Ministry of Defence. *Memorandum to the Committee from the Royal Ordnance Trade Unions, Ministry of Defence Comments, Annex A*. UK Parliament, February 2001.

[61] SBIR Solicitations,US Department of Defense. Plateau burning composite propellant with minimized temperature sensitivity. SBIR Solicitations, April 2013.

[62] Ahu Gümrah Dumanlı and Alan H. Windle. Carbon fibres from cellulosic precursors: a review. *Journal of Materials Science*, 47(10):4236–4250, 2012.

[63] Yoshiharu Nishiyama, Paul Langan, and Henri Chanzy. Crystal structure and hydrogen-bonding system in cellulose iβ from synchrotron x-ray and neutron fiber diffraction. *J. Am. Chem. Soc.*, 124(31):9074–9082, August 2002.

[64] Yoshiharu Nishiyama, Junji Sugiyama, Henri Chanzy, and Paul Langan. Crystal structure and hydrogen bonding system in cellulose iα from synchrotron x-ray and neutron fiber diffraction. *J. Am. Chem. Soc.*, 125(47):14300–14306, November 2003.

[65] Shishir P. S. Chundawat, Giovanni Bellesia, Nirmal Uppugundla, Leonardo da Costa Sousa, Dahai Gao, Albert M. Cheh, Umesh P. Agarwal, Christopher M. Bianchetti, George N. Phillips, Paul Langan, Venkatesh Balan, S. Gnanakaran, and Bruce E. Dale. Restructuring the crystalline cellulose hydrogen bond network enhances its depolymerization rate. *J. Am. Chem. Soc.*, 133(29):11163–11174, July 2011.

[66] Yulia A. Gismatulina, Vera V. Budaeva, and Gennady V. Sakovich. Nitrocellulose synthesis from miscanthus cellulose. *Prop., Explos., Pyrotech.*, 43(1):96–100, January 2018.

[67] Ahu Gumrah Dumanli. Nanocellulose and its composites for biomedical applications. *Current Medicinal Chemistry*, 24(5):512 – 528, 2017.

[68] Jan Řezáč, Kevin E. Riley, and Pavel Hobza. S66: A well-balanced database of benchmark interaction energies relevant to biomolecular structures. *J. Chem. Theory Comput.*, 7(8):2427–2438, August 2011.

[69] Srinivasan Parthiban, Glênisson de Oliveira, and Jan M. L. Martin. Benchmark ab initio energy profiles for the gas-phase sn2 reactions y- + ch3x → ch3y + x- (x,y = f,cl,br). validation of hybrid dft methods. *J. Phys. Chem. A*, 105(5):895–904, February 2001.

[70] A. Patrícia Bento, Miquel Solà, and F. Matthias Bickelhaupt. E2 and sn2 reactions of x- + ch3ch2x (x = f, cl); an ab initio and dft benchmark study. *J. Chem. Theory Comput.*, 4(6):929–940, June 2008.

[71] Manoj K. Shukla and Frances Hill. Computational elucidation of mechanisms of alkaline hydrolysis of nitrocellulose: Dimer and trimer models with comparison to the corresponding monomer. *J. Phys. Chem. A*, 116(29):7746–7755, July 2012.

[72] P. J. Linstrom; W. G. Mallard. *NIST Standard Reference Database Number 69.* National Institute of Standards and Technology, https://doi.org/10.18434/T4D303, 2020.

[73] A. Patrícia Bento, Miquel Solà, and F. Matthias Bickelhaupt. Ab initio and dft benchmark study for nucleophilic substitution at carbon (sn2@c) and silicon (sn2@si). *J. Comput. Chem.*, 26(14):1497–1504, November 2005.

[74] Julian Tirado-Rives and William L. Jorgensen. Performance of b3lyp density functional methods for a large set of organic molecules. *J. Chem. Theory Comput.*, 4(2):297–306, February 2008.

[75] Roy Dennington, Todd A. Keith, and John M. Millam. Gaussview Version 5.0.8, 2009. Semichem Inc. Shawnee Mission KS.

[76] G. Schaftenaar and J. H. Noordik. Molden: a pre- and post-processing program for molecular and electronic structures*. *Journal of Computer-Aided Molecular Design*, 14(2):123–134, 2000.

[77] Gijs Schaftenaar, Elias Vlieg, and Gert Vriend. Molden 2.0: quantum chemistry meets proteins. *Journal of Computer-Aided Molecular Design*, 31(9):789–800, 2017.

[78] Marcus D. Hanwell, Donald E. Curtis, David C. Lonie, Tim Vandermeersch, Eva Zurek, and Geoffrey R. Hutchison. Avogadro: an advanced semantic chemical editor, visualization, and analysis platform. *Journal of Cheminformatics*, 4(1):17, 2012.

[79] A. Cauchy. Methode generale pour la resolution des systemes d'equations simultanees. *C.R. Acad. Sci. Paris*, 25:536–538, 1847.

[80] Juan C. Meza. Steepest descent. *WIREs Comp Stat*, 2(6):719–722, November 2010.

[81] Tian Lu and Feiwu Chen. Multiwfn: A multifunctional wavefunction analyzer. *J. Comput. Chem.*, 33(5):580–592, February 2012.

[82] T. P. Yin and R. K. Brown. The reactivity of cellulose: Iii. the nitration of cotton linters alternatiely wetted with water at various temperatures and dried, and the probably distribution of the nitrate groups. *Can. J. Chem.*, 37(2):444–453, February 1959.

[83] Jimmie C. Oxley, Peter Politzer, and Jane S. Murray. Chapter 1 - a survey of the thermal stability of energetic materials. In *Theoretical and Computational Chemistry*, volume 12, pages 5–48. Elsevier, 2003.

[84] M. F. Foltz. Aging of pentaerythritol tetranitrate (petn). Technical report, Lawrence Livermore National Laboratory, United States, 2009.

[85] T. Shepodd, R. Behrens, D. Anex, D. Miller, and K. Anderson. Degradation chemistry of petn and its homologues. Technical report, Sandia National Laboratories, United States, 1997.

[86] M. F. Zaki, Ali Mostafa Ali, and Rafat M. Amin. Effect of gamma irradiation on optical and chemical properties of cellulose nitrate thin films. *Journal of Adhesion Science and Technology*, 31(12):1314–1327, June 2017.

[87] Roman V. Tsyshevsky, Onise Sharia, and Maija M. Kuklja. Thermal decomposition mechanisms of nitroesters: Ab initio modeling of pentaerythritol tetranitrate. *J. Phys. Chem. C*, 117(35):18144–18153, September 2013.

[88] Mohammed Moniruzzaman, John M. Bellerby, and Manfred A. Bohn. Activation energies for the decomposition of nitrate ester groups at the anhydroglucopyranose

ring positions c2, c3 and c6 of nitrocellulose using the nitration of a dye as probe. *Polymer Degradation and Stability*, 102:49–58, 2014.

[89] I. Rodger and J. D. Mcirvine. The decomposition of spent petn nitration acids. *Can. J. Chem. Eng.*, 41(2):87–90, April 1963.

[90] Torbjörn Lindblom. Reactions in stabilizer and between stabilizer and nitrocellulose in propellants. *Propellants, Explosives, Pyrotechnics*, 27(4):197–208, September 2002.

[91] Hermann N. Volltrauer and Arthur Fontijn. Low-temperature pyrolysis studies by chemiluminescence techniques real-time nitrocellulose and pbx 9404 decomposition. *Combustion and Flame*, 41:313–324, 1981.

[92] Mª Ángeles Fernández de la Ossa, María López-López, Mercedes Torre, and Carmen García-Ruiz. Analytical techniques in the study of highly-nitrated nitrocellulose. *TrAC Trends in Analytical Chemistry*, 30(11):1740–1755, 2011.

[93] John W. Baker and D. M. Easty. 217. hydrolytic decomposition of esters of nitric acid. part i. general experimental techniques. alkaline hydrolysis and neutral solvolysis of methyl, ethyl, isopropyl, and tert.-butyl nitrates in aqueous alcohol. *J. Chem. Soc.*, (0):1193–1207, 1952.

[94] N. Binke, L. Rong, Y. Zhengquan, W. Yuan, Y. Pu, Hu Rongzu, and Y. Qingsen. Studies on the kinetics of the first order autocatalytic decomposition reaction of highly nitrated nitrocellulose. *Journal of Thermal Analysis and Calorimetry*, 58(2):403–411, 1999.

[95] M. A. Zayed, Salah E. M. El-Begawy, and Hossam E. S. Hassan. Enhancement of stabilizing properties of double-base propellants using nano-scale inorganic compounds. *Journal of Hazardous Materials*, 227-228:274–279, 2012.

[96] Djalal Trache and Ahmed Fouzi Tarchoun. Stabilizers for nitrate ester-based energetic materials and their mechanism of action: a state-of-the-art review. *Journal of Materials Science*, 53(1):100–123, 2018.

[97] E. Camera, G. Modena, and B. Zotti. On the behaviour of nitrate esters in acid solution. ii. hydrolysis and oxidation of nitroglycol and nitroglycerin. *Propellants, Explosives, Pyrotechnics*, 7(3):66–69, June 1982.

[98] K. S. Hu, A. I. Darer, and M. J. Elrod. Thermodynamics and kinetics of the hydrolysis of atmospherically relevant organonitrates and organosulfates. *ACP*, 11(16):8307–8320, August 2011.

[99] E. K. Rideal and A. J. B. Robertson. The spontaneous ignition of nitrocellulose. *Symposium on Combustion and Flame, and Explosion Phenomena*, 3(1):536–544, 1948.

[100] Ruichao Wei, Yaping He, Jiahao Liu, Yu He, Wenzhong Mi, Richard Yuen, and Jian Wang. Experimental Study on the Fire Properties of Nitrocellulose with Different Structures. *Materials*, 10(3):316, mar 2017.

[101] V. G. Matveev and G. M. Nazin. Stepwise degradation of polyfunctional compounds. *Kinetics and Catalysis*, 44(6):735–739, 2003.

[102] A.G. Afanas'ev, B.A. Lur'e, and B.S. Svetlov. *Teoriya vzryvchatykh veshchestv (Theory of Explosive Substances)*, volume 53, page 63. Moscow: Mendeleev University of Chemical Technology, 1967.

[103] B.A. Lur'e and B.S. Svetlov. *Teoriya vzryvchatykh veshchestv (Theory of Explosive Substances)*, volume 53, page 51. Moscow: Mendeleev University of Chemical Technology, 1967.

[104] Manoj K. Kesharwani, Brina Brauer, and Jan M. L. Martin. Frequency and zero-point vibrational energy scale factors for double-hybrid density functionals (and other selected methods): Can anharmonic force fields be avoided? *J. Phys. Chem. A*, 119(9):1701–1714, March 2015.

[105] Pankaj Sinha, Scott E. Boesch, Changming Gu, Ralph A. Wheeler, and Angela K. Wilson. Harmonic vibrational frequencies: Scaling factors for hf, b3lyp, and mp2 methods in combination with correlation consistent basis sets. *J. Phys. Chem. A*, 108(42):9213–9217, October 2004.

[106] Wee Lam Ng, John E. Field, and Herman M. Hauser. Study of the thermal decomposition of pentaerythritol tetranitrate. *J. Chem. Soc., Perkin Trans. 2*, (6):637–639, 1976.

[107] Jimmie C. Oxley, James L. Smith, Joseph E. Brady IV, and Austin C. Brown. Characterization and analysis of tetranitrate esters. *Propellants, Explosives, Pyrotechnics*, 37(1):24–39, February 2012.

[108] D Chambers, C Brackett, and D O Sparkman. Perspectives on pentaerythritol tetranitrate (petn) decomposition. 7 2002.

[109] Yu Ran Luo. *Handbook of Bond Dissociation Energies in Organic Compounds*, chapter 3, page 76. CRC Press, 2002.

[110] Kimberly A. Jebber, Kui Zhang, Carolyn J. Cassady, and Alice Chung-Phillips. Ab initio and experimental studies on the protonation of glucose in the gas phase. *J. Am. Chem. Soc.*, 118(43):10515–10524, January 1996.

[111] Dajiang Liu, Mark R. Nimlos, David K. Johnson, Michael E. Himmel, and Xianghong Qian. Free energy landscape for glucose condensation reactions. *J. Phys. Chem. A*, 114(49):12936–12944, December 2010.

[112] Catherine E. Check and Thomas M. Gilbert. Progressive systematic underestimation of reaction energies by the b3lyp model as the number of c-c bonds increases: Why organic chemists should use multiple dft models for calculations involving polycarbon hydrocarbons. *J. Org. Chem.*, 70(24):9828–9834, November 2005.

[113] Steven M. Bachrach. Computational organic chemistry. *Annu. Rep. Prog. Chem., Sect. B: Org. Chem.*, 104(0):394–426, 2008.

[114] Stefan Grimme. n-alkane isodesmic reaction energy errors in density functional theory are due to electron correlation effects. *Org. Lett.*, 12(20):4670–4673, October 2010.

[115] Andrey A. Fokin, Lesya V. Chernish, Pavel A. Gunchenko, Evgeniya Yu. Tikhonchuk, Heike Hausmann, Michael Serafin, Jeremy E. P. Dahl, Robert M. K. Carlson, and Peter R. Schreiner. Stable alkanes containing very long carbon-carbon bonds. *J. Am. Chem. Soc.*, 134(33):13641–13650, August 2012.

[116] Steven M. Bachrach. Amine superbases stabilized by extended hydrogen bond networks. *J. Org. Chem.*, 78(21):10909–10916, November 2013.

[117] Josefredo R. Pliego, Jr. and José M. Riveros. The gas-phase reaction between hydroxide ion and methyl formate: A theoretical analysis of the energy surface and product distribution. *Chem. Eur. J.*, 7(1):169–175, January 2001.

[118] Josefredo R. Pliego, Jr. and José M. Riveros. A theoretical analysis of the free-energy profile of the different pathways in the alkaline hydrolysis of methyl formate in aqueous solution. *Chem. Eur. J.*, 8(8):1945–1953, April 2002.

[119] Jayaraman Chandrasekhar, Scott F. Smith, and William L. Jorgensen. Theoretical examination of the sn2 reaction involving chloride ion and methyl chloride in the gas phase and aqueous solution. *J. Am. Chem. Soc.*, 107(1):154–163, January 1985.

[120] Poliana Lima da Silva, Luciana Guimarães, and Josefredo R. Pliego. Revisiting the mechanism of neutral hydrolysis of esters: Water autoionization mechanisms with acid or base initiation pathways. *J. Phys. Chem. B*, 117(21):6487–6497, May 2013.

[121] Manoj K. Shukla and Frances Hill. Can an α-anomer of the trinitro form of d-glucopyranose be more easily hydrolyzed in alkaline environment than the β-anomer? a detailed theoretical analysis. *J. Phys. Chem. A*, 116(20):4909–4921, May 2012.

[122] Xianghong Qian. Mechanisms and energetics for acid catalyzed β-d-glucose conversion to 5-hydroxymethylfurfurl. *J. Phys. Chem. A*, 115(42):11740–11748, October 2011.

[123] M. Moniruzzaman and J. M. Bellerby. Use of uv-visible spectroscopy to monitor nitrocellulose degradation in thin films. *Polymer Degradation and Stability*, 93(6):1067–1072, 2008.

[124] Fotis Rigas, Ioannis Sebos, and Danae Doulia. Safety charts simulation of nitroglycerine/nitroglycol spent acids via chemical reaction kinetics. *Ind. Eng. Chem. Res.*, 36(12):5068–5073, December 1997.

[125] Christof Aellig, Ulrich Neuenschwander, and Ive Hermans. Acid-catalyzed decomposition of the benzyl nitrite intermediate in hno3-mediated aerobic oxidation of benzyl alcohol. *ChemCatChem*, 4(4):525–529, April 2012.

[126] S. J. Buelow, D. Allen, G. K. Anderson, F. L. Archuleta, J. H. Atencio, G. T. Baca, W. D. Breshears, T. J. Butenhoff, P. C. Dell'Orco, R. B. Dyer, B. R. Foy, K. A. Funk, D. M. Harradine, K. C. Knutsen, J. L. Lyman, D. A. Masten, T. G. McGuinness, R. E. McInroy, C. J. Monahan, R. C. Oldenborg, J. M. Robinson, M. A. Sedillo, D. A. Counce, C. K. Rofer, P. E. Trujillo, R. L. Brewer, G. A. Buntain, R. L. Flesner, J. A. Sanchez, T. Spontarelli, L. L. Sprouse, C. A. Vecere, G. R. Brewer, R. D. McFarland, W. J. Parkinson, R. P. Courier, S. M. Chitanvis, C. W. Pattersen, and L. R. Pratt. Destruction of energetic materials in supercritical water. Technical report, Air Force Research Laboratory, Los Alamos National Laboratory, New Mexico 87545, 2002.

[127] L. Dauerman and Y. A. Tajima. Thermal decomposition and combustion of nitrocellulose. *AIAA Journal*, 6(8):1468–1473, August 1968.

[128] E. Camera, G. Modena, and B. Zotti. On the behaviour of nitrate esters in acid solution. iii. oxidation of ethanol by nitric acid in sulphuric acid. *Propellants, Explosives, Pyrotechnics*, 8(3):70–73, June 1983.

[129] Juan F. Arenas, Francisco J. Avila, Juan C. Otero, Daniel Peláez, and Juan Soto. Approach to the atmospheric chemistry of methyl nitrate and methylperoxy nitrite. chemical mechanisms of their formation and decomposition reactions in the gas phase. *J. Phys. Chem. A*, 112(2):249–255, January 2008.

[130] Frank E. Wolf. Alkaline hydrolyis conversion of nitrocellulose fines. techreport, Badger Army Ammunition Plant, Olin Corporation, Badger Army Ammunition Plant, Baraboo, WI 53913, October 1997.

[131] NIST Computational Chemistry Comparison and Benchmark Database. Nist standard reference database number 101. http://cccbdb.nist.gov/, August 2020.

[132] Neha Awasthi, Thomas Ritschel, Reinhard Lipowsky, and Volker Knecht. Standard gibbs energies of formation and equilibrium constants from ab-initio calculations: Covalent dimerization of no2 and synthesis of nh3. *The Journal of Chemical Thermodynamics*, 62:211–221, 2013.

[133] G. K. Adams and C. E. H. Bawn. The homogeneous decomposition of ethyl nitrate. *Trans. Faraday Soc.*, 45(0):494–499, 1949.

[134] Kai Wang, Dabin Liu, Sen Xu, and Gaowen Cai. Research on the thermal history's influence on the thermal stability of ehn and nc. *Thermochimica Acta*, 610:23–28, 2015.

[135] Hua Chai, Qiangling Duan, Lin Jiang, Liang Gong, Haodong Chen, and Jinhua Sun. Theoretical and experimental study on the effect of nitrogen content on the thermal characteristics of nitrocellulose under low heating rates. *Cellulose*, 26(2):763–776, 2019.

[136] Deac Rossell. Exploding teeth, unbreakable sheets, and continuous casting : Nitrocellulose, from guncotton to early cinema. *This Film is Dangerous*, 2002.

[137] Alexander Parkes. Parkesine replica of bronze medal awarded to alexander parkes at the international exhibition in 1862. 1862. Replica medal. Object number: 2009-177.

[138] A. S. Greenberg and Simon Broder. The story of nitrocellulose. *Journal of the Patent Office Society*, 8(11):517–529, 1925.

[139] Sebastien Berthumeyrie, Steeve Collin, Pierre-Olivier Bussiere, and Sandrine Therias. Photooxidation of cellulose nitrate: New insights into degradation mechanisms. *Journal of Hazardous Materials*, 272:137–147, 2014.

[140] V. A. Khryachkov, E. A. Saratovskikh, R. N. Yarullin, and A. V. Kulikov. Effect of the d. desulfuricans bacterium and uv radiation on nitrocellulose oxidation. *Russian Journal of Physical Chemistry B*, 11(4):697–703, 2017.

[141] A. J. Taylor. Explosibility hazard of unpigmented industrial nitrocellulose. Technical Report 1, Royal Armament Research and Development Establishment, Ministry of Defence, UK, September 1971.

[142] David M. French. The density of cellulose nitrate. *J. Appl. Polym. Sci.*, 22(1):309–313, January 1978.

[143] D. T. Clark and P. J. Stephenson. A 13c n.m.r. and x-ray study of the relationship between the distribution of nitrate ester groups and interchain d(110) spacings in a series of cellulose nitrates. *Polymer*, 23(9):1295–1299, 1982.

[144] R. G. Zhbankov. Hydrogen bonds and structure of carbohydrates. *Journal of Molecular Structure*, 270:523–539, 1992.

[145] Margaretha Akerholm, Barbara Hinterstoisser, and Lennart Salmen. Characterization of the crystalline structure of cellulose using static and dynamic ft-ir spectroscopy. *Carbohydrate Research*, 339(3):569–578, 2004.

[146] Lisa A. Richards, Anthony Nash, Maximillian Joshua Sebastian Phipps, and Nora H. de Leeuw. A molecular dynamics study of plasticiser migration in nitrocellulose binders. *New J. Chem.*, 42(21):17420–17428, 2018.

[147] Diego Ardura and D. J. Donaldson. Where does acid hydrolysis take place? *Phys. Chem. Chem. Phys.*, 11(5):857–863, 2009.

[148] Xianghong Qian, Mark R. Nimlos, David K. Johnson, and Michael E. Himmel. Acidic sugar degradation pathways. In Brian H. Davison, Barbara R. Evans, Mark Finkelstein, and James D. McMillan, editors, *Twenty-Sixth Symposium on Biotechnology for Fuels and Chemicals*, pages 989–997. Humana Press, Totowa, NJ, 2005.

[149] Xianghong Qian, Mark R. Nimlos, Mark Davis, David K. Johnson, and Michael E. Himmel. Ab initio molecular dynamics simulations of β-d-glucose and β-d-xylose degradation mechanisms in acidic aqueous solution. *Carbohydrate Research*, 340(14):2319–2327, 2005.

[150] Xianghong Qian, David K. Johnson, Michael E. Himmel, and Mark R. Nimlos. The role of hydrogen-bonding interactions in acidic sugar reaction pathways. *Carbohydrate Research*, 345(13):1945–1951, 2010.

[151] Tomas L. Jensen, John F. Moxnes, Erik Unneberg, and Ove Dullum. Calculation of decomposition products from components of gunpowder by using reaxff reactive force field molecular dynamics and thermodynamic calculations of equilibrium composition. *Propellants, Explosives, Pyrotechnics*, 39(6):830–837, December 2014.

[152] Liu Huwei and Fu Ruonong. Studies on thermal decomposition of nitrocellulose by pyrolysis-gas chromatography. *Journal of Analytical and Applied Pyrolysis*, 14(2):163–169, 1988.

[153] D. T. Clark, P. J. Stephenson, and F. Heatley. Partial degrees of substitution in cellulose nitrates determined by means of 13c magnetic resonance studies. *Polymer*, 22(8):1112–1117, 1981.

[154] V. I. Kovalenko, R. M. Mukhamadeeva, L. N. Maklakova, and N. G. Gustova. Interpretation of the ir spectrum and structure of cellulose nitrate. *Journal of Structural Chemistry*, 34(4):540–547, 1994.

[155] Ting Kai Wu. Carbon-13 and proton nuclear magnetic resonance studies of cellulose nitrates. *Macromolecules*, 13(1):74–79, January 1980.